

Guided Wave Echolocation for Inspection Robots

Ross James McMillan

Department of Electronic and Electrical Engineering

University of Strathclyde

A thesis submitted for the degree of

Doctor of Philosophy

August 2024

Copyright

This thesis is the result of the author's original research. It has been composed by the author and has not been previously submitted for examination which has led to the award of a degree.

The copyright of this thesis belongs to the author under the terms of the United Kingdom Copyright Acts as qualified by University of Strathclyde Regulation 3.50. Due acknowledgement must always be made of the use of any material contained in, or derived from, this thesis.

Signed: 

Date: 26/09/2024

Acknowledgements

Foremost, I would like to thank my supervisors, Prof Gordon Dobie and Dr Morteza Tabatabaeipour, and my parents, Susan and David McMillan, for their support, encouragement and continued patience.

My thanks extend to all I have worked with throughout this study, in particular William, Adam, Rory, Kostas, Taiyi and Dayi.

I would like to thank the Centre for Ultrasonic Engineering for supporting this PhD via the Research Council for Non-Destructive Evaluation and the Engineering and Physical Sciences Research Council.

Abstract

Industrial assets such as storage tanks and pressure vessels require routine inspections to maintain safety standards. The precise localisation of inspection points is critical for tracking structural integrity over time and ensuring systematic analysis of inspection data. These assets are typically constructed from plate-like structures welded together, making welds very common across these structure. The welded sections can be utilised as landmarks to position and localise a mobile robotic inspection system by using ultrasonic guided waves, which have been shown to reflect from welded sections and edges. This study explored the efficacy of guided waves for echolocation-based localisation of mobile robotic inspection systems using wave reflections from welded sections.

A study on wave mode weld reflectivity was carried out to identify the best mode to reflect from welded sections in order to accurately range, as different modes interact with welds in different ways due to variations in wave characteristics such as energy density distribution and mode conversion effects. Through a systematic evaluation of five guided wave modes, the study identified SH1 at a frequency-thickness product of 2 MHz.mm as the most effective wave mode for robust weld reflections. SH1 consistently exhibited the highest reflection coefficient in simulation and experiment, averaging 0.45 across multiple weld geometries, with minimal mode conversion. A positional error of 2.65% was found in experiment using SH1.

To maximise the efficiency of guided wave generation and reception, a novel methodology for optimising Lorentz force PCB racetrack coil Periodic Permanent Magnet

(PPM) Electromagnetic Acoustic Transducers (EMATs) was developed. This optimisation methodology was found to double signal amplitude when compared to a non-optimised version of the same transducer. Following this the sensor optimisation methodology was applied to a sensor setup optimised for guided wave ranging from a mobile robot. The optimised sensor setup utilises a unidirectional side-shifted PPM array EMAT for transmission and reduced sized receiver for reception, reducing operational complexity, sensor size and magnetic holding force, and eliminating the need for an additional receiver. The experimental validation demonstrates that the optimised EMAT system significantly improves localisation accuracy while maintaining a compact and mobile-friendly form factor.

Contents

| | |
|---|------------|
| Contents | v |
| List of Figures | x |
| List of Tables | xix |
| Abbreviations | xx |
| 1. Introduction..... | 1 |
| 1.1. Project Motivation..... | 1 |
| 1.2. Robotically Deployed NDT Systems | 2 |
| 1.3. Positioning Mobile Inspection Robots | 3 |
| 1.4. Thesis Structure..... | 7 |
| 1.5. Aims & Objectives | 8 |
| 1.6. Contributions to Academia and Industry..... | 9 |
| 1.7. Lead Author Publications Arising from This Thesis..... | 10 |
| 1.8. Co-Author Publications Arising from this Thesis..... | 10 |
| 2. Literature Review | 13 |
| 2.1. Introduction | 13 |
| 2.2. Structures Under Inspection | 14 |
| 2.3. Non-Destructive Inspection Techniques | 16 |
| 2.3.1. Ultrasonic Inspection..... | 17 |

| | | |
|-----------|--|-----------|
| 2.3.2. | X-Ray | 24 |
| 2.3.3. | Pulsed Eddy Current..... | 25 |
| 2.3.4. | Visual Inspection Methods | 26 |
| 2.4. | Current State of the Art of NDT Robotic Crawlers..... | 27 |
| 2.5. | Mobile Robotic Positioning Systems | 33 |
| 2.5.2. | Sensing & Positioning in Commercial Robotics..... | 40 |
| 2.6. | Mobile Robotic Mapping and Exploration..... | 41 |
| 2.6.1. | Simultaneous Mapping and Localisation | 41 |
| 2.6.2. | Occupancy Grid Mapping | 45 |
| 2.6.3. | Mobile Robotic Inspection Crawlers Utilising Guided Waves for Mapping/Localisation Purposes | 46 |
| 2.7. | Conclusion..... | 49 |
| 3. | Electromagnetic Acoustic Transducers and Guided Waves..... | 52 |
| 3.1. | Introduction | 52 |
| 3.2. | Ultrasonic Guided Waves..... | 53 |
| 3.2.1. | Bulk Ultrasonic Waves..... | 53 |
| 3.2.2. | Guided Wave Modes and Dispersion..... | 56 |
| 3.2.3. | Guided Wave Energy Density Distribution..... | 67 |
| 3.3. | Electromagnetic Acoustic Transducers | 69 |
| 3.3.1. | Practicality of EMAT Wave Generation..... | 69 |
| 3.3.2. | Styles of EMATs..... | 71 |
| 3.4. | EMAT Mechanisms | 75 |

| | | |
|-----------|--|-----------|
| 3.4.1. | The Lorentz Force | 75 |
| 3.4.2. | EMAT Physics | 78 |
| 3.4.3. | Magnetostriction Mechanism | 82 |
| 3.4.4. | Detection Process | 83 |
| 3.5. | Chapter Conclusion | 84 |
| 4. | Characterisation of EMAT Guided Wave Reflectivity on Welded Structures for use in Ranging | 85 |
| 4.1. | Introduction | 85 |
| 4.2. | Existing Research Investigating Guided Wave Weld Reflectivity | 86 |
| 4.3. | Guided Wave Weld Reflectivity Investigation | 87 |
| 4.3.1. | Desired Wave Behaviours | 89 |
| 4.4. | Methodology | 90 |
| 4.5. | Simulation | 92 |
| 4.5.1. | Simulation Setup | 92 |
| 4.5.2. | Data Extraction..... | 97 |
| 4.5.3. | Wave Mode Simulation Results | 101 |
| 4.6. | Experiment | 102 |
| 4.6.1. | Weld Samples..... | 102 |
| 4.6.2. | Experimental Measurement Setup..... | 103 |
| 4.6.3. | Experimental Results and Comparison to Simulation..... | 105 |
| 4.7. | Ranging Evaluation | 107 |
| 4.8. | Investigation Conclusion..... | 111 |

| | |
|--|------------|
| 5. Design and Manufacture of an Optimised Side-Shifted PPM EMAT Array for Use in Mobile Robotic Localisation..... | 113 |
| 5.1. Introduction | 113 |
| 5.2. Optimising Sensor Setup for Positioning | 114 |
| 5.3. Optimisation and Methodology..... | 119 |
| 5.3.1. Transmitter Coil Optimisation..... | 120 |
| 5.3.2. Transmitter Magnet Array Optimisation..... | 125 |
| 5.4. Validation of Optimisation Model | 127 |
| 5.4.1. Magnetisation Validation via Experiment..... | 127 |
| 5.4.2. Industrial EMAT Comparison..... | 129 |
| 5.5. Mobile Robotic Transducer Design | 131 |
| 5.5.1. Transmitter/Receiver Setup..... | 131 |
| 5.5.2. Transmitter EMAT Design..... | 133 |
| 5.5.3. Reduced Size Receiver EMAT Design | 135 |
| 5.5.4. Simulation of Unidirectional Transmitter EMAT..... | 136 |
| 5.5.5. Experimental Test of Unidirectional EMAT..... | 138 |
| 5.5.6. Transducer Ranging | 141 |
| 5.6. Investigation Conclusion..... | 147 |
| 6. Conclusion | 150 |
| 6.1. Thesis Summary | 150 |
| 6.2. Thesis Findings..... | 152 |
| 6.2.1. Guided Wave Weld Reflectivity Investigation | 152 |

| | |
|---|------------|
| 6.2.2. Racetrack EMAT Optimisation Methodology and Sensor Setup | |
| Optimisation | 153 |
| 6.3. Future Work | 154 |
| References | 156 |

List of Figures

Fig. 1 Shows a comparison of the worker driven inspection (left) and the equipment required to do so, vs. the robotic crawler driven inspection (right). Both methods are carrying out an inspection on a very difficult to access underside area of an oil rig [13]. 3

Fig. 2 Image of a pressure vessel adapted from [15], where the welded sections are highlighted in blue, multiple long butt welds, can be seen to join the curved plates together to form the cylindrical pill structure, the underside support welds are highlighted in red.4

Fig. 3 Conceptual example of a robot utilising guided waves for locating itself on a steel pressure vessel.....6

Fig. 4 A) Typical above ground liquid storage tanks used in a variety of processing industries [25]. B) Typical industrial silos which are constructed by welding sheet metals together to form the larger structure [26]. C) Another example of an above storage tanker, the welds use to join the plates can be clearly seen here [27]. D) An example of a typical pressure vessel design, butt welds can be seen around the structures circumference and at the underside supports [28]. 15

Fig. 5 Exemplar diagrams of butt, lap, tee, corner, and edge joints. Adapted from [30].16

Fig. 6 A typical bulk ultrasonic inspection, the faster returning signal implies the presence of a flaw in the subjects bulk material, adapted from [20]..... 18

Fig. 7 Ultrasonic beam focussing can be achieved by delaying the wave launch times between each array element, adapted from [21]. 19

Fig. 8 A typical pancake coil EMAT is shown here, where the interactions between the permanent magnetic fields and the alternating image currents, create Lorentz forces that vibrate the subject. Adapted from [25].20

Fig. 9 An example of generation and reception of Lamb waves in a plate-like subject using air-coupled ultrasonic transmitters, discussed in [50].....22

Fig. 10 A) Thermoelastic laser ultrasound generation diagram, adapted from [52]. B) Ablative laser ultrasound diagram, adapted from [51].....23

Fig. 11 Example of the result of radiographic inspection of a pipeline, the green text measurements show the measured remaining wall thickness, with the dark spotted patches representing corrosion and pitting [57]. The thicker section of dark spotting is a welded section.25

Fig. 12 An example of typical Eddy Current inspection measuring plate thickness [60].26

Fig. 13 The Waygate Technologies BIKE, equipped with manipulating arm and a piezoelectric ultrasonic transducer. This robot is remote controlled and the operator utilises the camera in between the lights to inspect the subject. Adapted from [47].29

Fig. 14 A) The Scorpion 2 vertically traversing a ferromagnetic above ground tanker wall [79]. B) A close shot of the Scorpion 2 showing the dry coupled sensor head [80].....32

Fig. 15 The R-AUT horizontally traversing an above ground tanker, carrying out a raster scan to create a corrosion map. The ultrasonic probe is fed liquid couplant through umbilical cord, this cord also connects power and the user input to the robot [66].....33

Fig. 16 Diagram illustrating defect mapping error.34

Fig. 17 The yellow triangles depict the history of the robots true pose and the blue triangles represent the history of the robots estimated pose. The red shapes represent the true position of the observed landmarks and the green shapes represent the robots estimation of the observed landmarks. The arrows depict the robots observation of the landmarks.43

Fig. 18 Image of the simulated plate and transducer setup used for generating and detecting SH0 at different positions on the sample.48

Fig. 19 The robot pose is represented by the red diamond, as it is moving across the plate it is generating SH0 waves which reflect from the plate boundaries. The boundaries are shown by the cells filled in black, as there is high certainty that a boundary is being reflected from. The white filled cells represent areas of high certainty where there are no plate features.48

Fig. 20 Longitudinal propagation and shear wave propagation, image taken from [128].53

Fig. 21 Occurrences of Lamb waves are shown by solid lines, occurrences of Shear Horizontal waves are shown by the dashed lines. The blue and red indicates asymmetric and symmetric for Lamb waves and for Shear Horizontal waves. This plot was generated using Dispersion Calculator programme (German Aerospace Centre, DE).59

Fig. 22 An example of a 2DFFT plot to confirm that SH1 was generated in an experimental setup. SH1 was generated in 10mm steel and measured experimentally, the data was processed and plotted by wavenumber and frequency occurrences, with theoretical dispersion curves for the same sample overlaid.....61

Fig. 23 Symmetric/extensional (left) and anti-symmetric/flexural Lamb wave propagation, adapted from [137]......62

Fig. 24 Shear Horizontal guided wave mode propagation, adapted from [137].65

Fig. 25 The displacement patterns of three modes of the same wave type but different orders, in 10mm steel, SH0, SH1 and SH2. Generated using the programme Dispersion Calculator. Plate thickness axis is displayed in Fig. 24.67

Fig. 26 The coordinate system that is used to calculate the energy density through a plates thickness is shown here, where the direction of propagation can be seen, the plane on which the thickness lies and the cross section S.68

Fig. 27 An example of PPM EMAT with the housing removed where the magnet array and racetrack coil can be seen, this EMAT is designed to generate SH0 and SH1 with 25mm wavelengths.72

Fig. 28 Diagram of a unidirectional EMAT transmitter. Two coils, blue and orange, with wide centre gap spacing, are overlapped and offset by 90degrees of phase. The magnet array, red and blue squares, is also staggered to match the coil offset.73

Fig. 29 Diagrammatic representation of the Lorentz force mechanism in a racetrack coil PCB bidirectional EMAT, shown are the induced eddy currents in orange, magnetic flux, **B**, density surrounding the magnets perpendicular to the coil and the direction of propagation of the generated guided waves depicted by the blue arrow.76

Fig. 30 Theoretical dispersion curve for guided waves in 10mm thick steel. Lamb (solid lines) and Shear Horizontal (dashed lines) wave modes are shown. Asymmetric modes are blue and symmetric modes are red, this graph was generated using the Dispersion

Calculator Software (Centre for Lightweight Production Technology, DE). X's represent the frequencies of the wave modes used in this work.....88

Fig. 31 Experimental data. First received direct signal, left edge reflection signals and weld signals are highlighted. SH1 at 205kHz was used on Sample 3 for these measurements. The blue signal is where the receiver is 20cm from the weld and the orange signal is where the receiver is 60cm from the weld.....90

Fig. 32 Energy density (E_{Total}) distributions across 10mm plate for A0, S0, S1, SH0 and SH1 generated using Dispersion Calculator.92

Fig. 33 The weld sample model with the PPM EMAT block representations and monitoring point representations for SH wave inspection, which allow measurement at 64 different points with 1mm spacing.....93

Fig. 34 The various key propagation paths of the waves generated in this setup are shown here with the propagation paths of interest being path A and path C.94

Fig. 35 a) SH generation block array, the arrows indicate the application of force when pulsed. b) Lamb wave generation block array the arrows indicate the application of force when pulse. In this case the application of force is perpendicular away from and into the subjects surface.96

Fig. 36 a) Shows initial generation of SH0. b) Shows the first wave passing under the receiver points. c) Shows the wave encountering the weld. d) Shows the wave reflecting from and passing through the weld.97

Fig. 37 Wavenumber-Frequency Amplitude plots for (a) A0 (91kHz) (b) S1 (375kHz) (c) SH1 (128kHz). The centre frequencies are highlighted. The mode conversion of the

| | |
|---|-----|
| generated waves and the waves that returned after reflecting from the weld, are those with negative wavenumbers..... | 99 |
| Fig. 38 An example of the Wavenumber-Normalised Amplitude plot that is used to find the magnitude of the first transmitted wave and the weld reflected wave, this example is for SH1 taken from the plot Fig 16c. The limits of the integration performed on the spikes are highlighted by the red dashed lines. | 100 |
| Fig. 39 Simulated data. The reflection coefficient for each mode and each sample is shown, SH1 is significantly more reflective than the other modes tested, S1 is the most reflective lamb mode. Good stability is shown by A0, SH0 and SH1. | 102 |
| Fig. 40a) Shows the welding angle of the robotic arm. b) Shows the welding setup with sample 2 clamped in place. | 103 |
| Fig. 41 Experimental setup where the LabVIEW programme is used to command the Ritec generating the pulses to send through the EMAT's. The signal from the receiver EMAT is sent to the Ritec, digitized in the Picoscope and sent back to the LabVIEW programme where it can be viewed..... | 105 |
| Fig. 42 Plots of SH0 and SH1 experimental and simulation data plotted with a best fit line to find the trend value using the best fit line gradient..... | 107 |
| Fig. 43 Each red dot represents the positions for the receiver when propagating the modes at the weld for range and distance estimation, the transmitter and receiver EMAT's are kept 300mm apart and colinear for all measurements. | 107 |
| Fig. 44 Distance is the distance from receiver to the weld. Distance vs Estimated Distance of SH0, group velocity 3259m/s, orange, and SH1, group velocity 2000m/s, blue, in | |

experiment. The dashed line shows the exact position of the weld to the centre of the EMAT. 108

Fig. 45 A) Shows the STFT plot used for each frequency tested vs time with the magnitude of the amplitude. B) Shows the selected frequency plotted in isolation to identify the reflected signal. 109

Fig. 46 An example of a two receiver, bidirectional transmitter EMAT setup using miniaturised EMATs, fixed to a mobile robotic crawler. The transmitter is the circular yellow sensor labelled T, the two receivers are labelled R. 115

Fig. 47 (a) Shows the signals received from the two receivers, it can be seen that there is a small offset in phase between both red and black. (b) Shows the normalised envelopes of the signals shown in (a), where the edges reflections from the subject can be seen. The difference in phase between the two signals can be used to identify the direction of features relative to the transducer setup. 115

Fig. 48 Geometrical coil input parameters for the numerical model, shown diagrammatically. 121

Fig. 49 Diagram showing the magnet array spacing dimensions for PPM EMAT based on [197] and [198]. The red and blue rectangles represent the magnets and their polarization. 126

Fig. 50 Numerical model magnetization - no. of turns curve, blue, with the experimental data points for 5, 10, 15, 18 and 25 turns shown, orange. 128

Fig. 51 Experimental Setup, the Ritec pulses the EMATs and receives the resultant signals, the Picoscope is triggered to record this and feeds the information to the LabVIEW program so it can be analysed. 130

Fig. 52 The top graph shows the A-Scans of each transmitter when generating SH0 and the bottom graph shows the A-Scans for SH1. It can be seen clearly the increase in signal amplitude when using the optimized transmitter. 131

Fig. 53 Diagram showing the magnet and coil arrangement of the unidirectional, reduced receiver setup. 10 x 10 mm magnets were used for the transmitter and 20 x 10 mm magnets were used for the receiver. 133

Fig. 54 Unidirectional EMAT schematic showing how the coil and time of pulsing offset creates constructive and destructive interference, adapted from [20]. 134

Fig. 55 Multiple stages of single sided wave generation can be seen in the images of the simulation. Initial wave generation can be seen where an enhanced forward propagating wave moving towards the left can be seen. Two significantly dampened side lobe waves can be seen propagating to the right, their amplitudes are less than 0.1 mV which is in the range to be considered noise. 137

Fig. 56 Signals produced by the simulated unidirectional transmitter, the dampened wave is significantly reduced in size compared to the undampened wave. 138

Fig. 57 The forward propagating waves and the backward propagating waves are shown, the difference in amplitude shows unidirectional transmission has been achieved experimentally. The signal at 3.5 μ s in the backward propagating signal is a reflected signal from the forward propagating wave. 140

Fig. 58 Ranging test setup and plate, the number of 10 cm steps for each transducer setup is illustrated, the bidirectional transducer setup is 35 cm in length and unidirectional transducer setup is 15 cm. Transmitters are represented by the red squares and receivers by the blue squares. The arrows indicate the directions of wave generation. 143

Fig. 59 An example of a point on the plate where the direction of the signals could not be inferred due to the reflecting signals returning back to both receivers at the same time, as indicated by the red lines. 145

Fig. 60 Shows the entire seven scans taken to further highlight the point on the plate where the two-receiver setup cannot map; this is 65 cm from the plate edge. 145

List of Tables

Table 1 – State of the Art of Ultrasonic Robotic Inspection Systems30

Table 2 – Examples in literature of common positioning methods for mobile systems. .39

Table 3 – Calculated Cross Sectional Area of weld head samples.95

Table 4 – Sample Longitudinal and Shear Velocities 100

Table 5 - Experimental Reflection Coefficients for SH0 and SH1 105

Table 6 – List of positioning methods with SH0 and SH1 added..... 111

Table 7 – Pseudo Code of the Numerical Model 124

Table 8 – Unidirectional EMAT Coil Parameter Inputs 135

Abbreviations

2DFFT – Two Dimensional Fast-Fourier Transform

AC – Alternating Current

CFL – Courant Friedrichs Lewy

CSA – Cross Sectional Area

DOF – Degrees of Freedom

EMAT – Electromagnetic Acoustic Transducers

FPCB – Flexible Printed Circuit Board

GPS – Global Positioning System

HAZ – Heat Affected Zone

IMU – Inertial Measurement Unit

IPS – Indoor Positioning Systems

LIDAR – Light Detection and Ranging

MIG – Metal Inert Gas

NDE – Non-Destructive Evaluation

NDT – Non-Destructive Testing

OGM – Occupancy Grid Mapping

PCB – Printed Circuit Board

PPM – Periodic Permanent Magnet

RTK – Real-Time Kinematic

RVI – Remote Visual Inspection

SH – Shear Horizontal

SLAM – Simultaneous Mapping and Localisation

SNR – Signal to Noise Ratio

STFT – Short-time Fourier Transform

TIG – Tungsten Inert Gas

TOF – Time of Flight

TWR – Track Width Ratio

ULP – User Language Programme

Chapter 1

1. Introduction

1.1. Project Motivation

Non-destructive testing of industrial assets such as storage tanks and pressure vessels, has traditionally been carried out manually by an experienced operator [1]. In a traditional NDT inspection cycle the main cost contributing components are the asset downtime/time of inspection, worker safety/access measures and asset repair [1], [2]. The cost of downtime of a Nuclear Plant in the UK operating at 1200MW [3], can be an estimated £1.4M per day at an electricity spot price of £50/MWh (2020) [4]. The time of inspection is largely determined by the inspection surface, the coverage/speed of the inspection tool, and the setup of access to the site which includes worker safety measures. Assets used in the energy sector such as pressure vessels, can have surface areas of up to 20,000m² [5], to thoroughly inspect a subject of this size using handheld non-destructive evaluation techniques is lengthy. Additionally, setups such as scaffolding, are required by law to ensure operator safety and the larger the area of the inspection, the greater the cost of such setups.

1.2. Robotically Deployed NDT Systems

Manual NDT inspection is suitable when a very small portion of a subject requires evaluation and the subject is easily accessible [6]. However when inspecting large industrial plant, where large areas of the subject require inspection, and the environment can be dangerous, there are clear benefits to using robotically deployed inspection methods [1], [2], [7]. For an inspection, the increase in cost and time associated with manual deployment can be described as follows; due to the limit of the number of measurements a human operator can take within a given time period, the total time of inspection will be significantly longer compared to a robotically driven inspection [8], [9]; if there is safety equipment that has to be constructed and possibly moved in order to complete the inspection to the desired standard, the total inspection time will be increased further, as well as the cost; the knock on effect of increased inspection time increases the plant down time where the subject cannot be used as shut down is typically required for inspection safety; so through the increased inspection time, the cost of inspection can increase rapidly due to the costs of safety equipment, costs of inspection and inspector and prolonged plant downtime [10]. Additionally repeatability of inspection quality cannot be guaranteed with manually driven inspection, which may result in sections of the inspection having to be repeated, robotically deployed inspection methods solve the issues associated with manual NDT.

The use of robotically driven inspection methods are becoming more prevalent in industry [11], remote assessment by an operator via a mobile robotic system offers a reliable and cheaper alternative, which removes the majority of hazards of inspection for operators [1], [2], [12], [13]. In a good example, Lou et. al [14] presented a comparison of inspecting an offshore oil riser and its flowlines, using rope access operator inspection versus visual inspection using drone/crawler systems. The advantages for using robotically deployed inspection methods were shown clearly in this study; with ease of access to areas and pipelines of the structure significantly increased; weather hazards did not impede robotic deployment compared to that of operator rope access; a 15% reduction of overall inspection cost and a 16 day reduction of inspection time, a 33.3% reduction in time.



Fig. 1 Shows a comparison of the worker driven inspection and the equipment required to do so (left), vs. the robotic crawler driven inspection (right). Both methods are carrying out an inspection on a very difficult to access underside area of an oil rig [14].

1.3. Positioning Mobile Inspection Robots

Modern commercial bulk-wave ultrasonic robotic inspection systems such as the Eddyfi RMS 2 (Eddyfi, Quebec, CA) [15], are utilised to measure subject wall thicknesses, and

can build Ultrasonic C-Scans (thickness maps) of sections of large industrial plant, such as shown in Fig. 2.

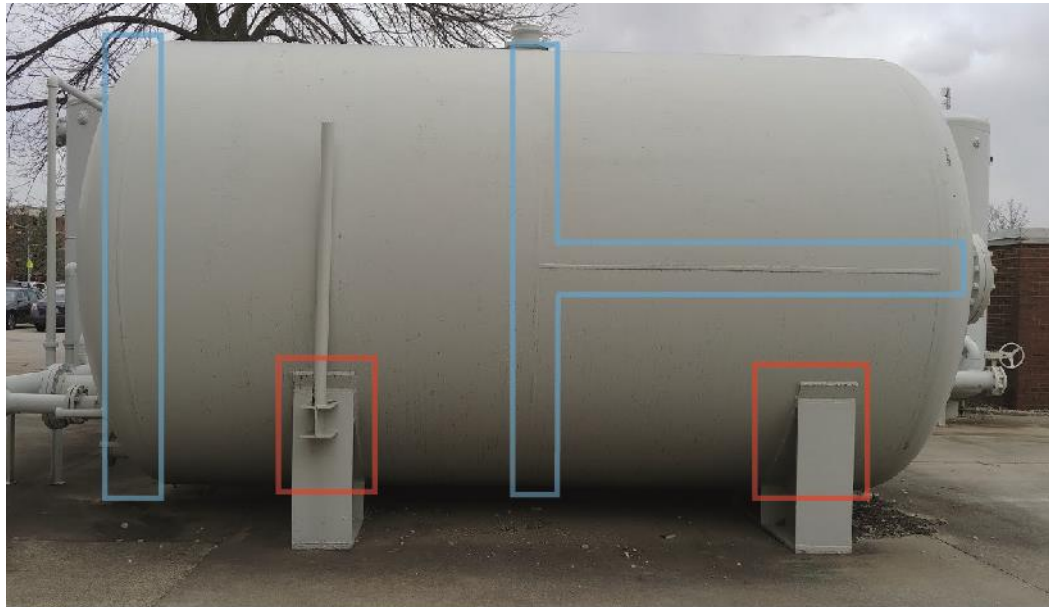


Fig. 2 Image of a pressure vessel adapted from [16], where the welded sections are highlighted in blue, multiple long butt welds, can be seen to join the curved plates together to form the cylindrical pill structure, the underside support welds are highlighted in red.

Due to the industrial environments that the inspection robots can operate in, conventional localisation systems can have limited operation capabilities. Onboard systems such as encoders and IMU positional estimates are subject to unavoidable integral error that accumulate over time [17]. This can be exacerbated by the subject's geometry which is likely to be curved and have welded sections which can be lumps on top of the scanning surface. Odd geometry increases the chance of wheel slippage which leads to positional errors. The radio signals from GPS systems are often blocked in industrial environments which is where many NDE applications are needed [18], [19]. Systems such as LIDAR degrade in accuracy with the shiny surfaces of the subjects under inspection [20].

Considering that the industrial plant under inspection are typically plate-like structures joined by welds, guided waves could be used to position a mobile robot with wave reflections from welded sections. Welds are extremely common features embedded in industrial plant, offering multiple reflectors across the entire structure. Guided waves can propagate up to 5 metres in plates, this was tested experimentally, which is considered suitable enough to be regularly in range of landmarks (welds) to position a robot. To range and position a mobile robot utilising welds and guided waves, a guided wave mode needs to be selected to do so. This mode would be best suited to reflecting from welds if it has strong reflections from welds, has no or little mode conversion and has little or no dispersion. An investigation into the guided wave mode which reflects best from welded sections is carried out and discussed in this thesis. SH1 was found to be the best suited mode as it had the highest reflection coefficients and had low dispersion so that ranging could be carried out.

Additionally industrial plant is typically made from ferromagnetic material and material which supports the use of Electromagnetic Acoustic Transducers (EMATs). EMATs are non-contact transducers which means they are more tolerant of positional errors and less surface prep is required compared to contact methods of transduction. This is beneficial in a mobile robotic setting as no complex methods are required to clean the surface and carefully place the sensor on the subject surface. EMATs are commonly used to generate guided waves and are the most practical method to generate Shear Horizontal guided wave modes.

As SH1 was found to be the mode best suited for ranging to position a mobile robot, an optimised sensor methodology was developed to improve the efficiency of Period Permanent Magnet (PPM) racetrack coil EMATs. Typical PPM EMATs are bidirectional which means two waves are generated in opposite directions along the longest axis of the EMATs geometry. Generating two waves makes positioning difficult when using one receiver, so two are required to understand the waves direction upon reception. This increases size of the sensor and the holding force of the sensors which can impede a mobile robots movement. To remove the second sensor a unidirectional transmitter design [21], [22] is optimised using the methodology developed and manufactured. The unidirectional design increases the amplitude of propagated wave and removes the need for a second receiver.



Fig. 3 Conceptual example of a robot utilising guided waves for locating itself on a steel pressure vessel.

1.4. Thesis Structure

The structure of the thesis is as follows.

Chapter 2 introduces typical industrial assets that require inspection and common inspection methods used to monitor the health of these structures. A current state of the art of mobile inspection robots is presented and the common positioning methods mobile inspection robots can use. Examples of mapping procedures used for automated robots are discussed as this contextualises where positioning information will be utilised.

Chapter 3 introduces the physics of ultrasonic bulk waves, this is built upon to derive the propagation physics of guided waves, both Lamb and Shear Horizontal waves. Electromagnetic acoustic transducers are then explored in detail to understand their operation mechanisms and the styles that can be produced.

Chapter 4 covers work carried out to identify the choice of optimal guided wave mode for echolocation, from a selection of five modes and different weld geometries. The guided wave modes were evaluated on their reflectivity from welded features, the mode with the highest reflectivity would be best suited for ranging and mapping.

Chapter 5 presents the development of a transduction setup optimised for mobile robotic ranging. An optimisation methodology was presented in order to greatly improve the efficacy of racetrack PCB EMATs, this methodology uses a numerical model to optimise the parameters of the racetrack coil and a guidance methodology for optimising and balancing the magnet array design, for increasing signal SNR (Signal to Noise Ratio) without increasing the input voltage. This optimisation methodology is applied to a

unidirectional transmitter and single reduced size receiver setup, which was found to be better for ranging in a mobile robotic situation compared to the previous setup.

The thesis ends with a conclusion and suggestions for future work.

1.5. Aims & Objectives

This research aims to advance the field of electromagnetic acoustic transducers for mobile robotic positioning by exploring guided wave technology and localisation techniques. By understanding the current state of the art and fundamental principles of EMATs, the study seeks to identify the most suitable guided wave mode for ranging from butt weld heads. Additionally, it focuses on developing an optimisation model for Lorentz force PCB coil PPM EMATs to enhance sensor efficiency. The ultimate goal is to design optimised EMATs capable of generating the selected wave mode for improved localisation and positioning in robotic applications.

- To understand the state of the art of localisation and EMAT technology.
- To understand the fundamentals of guided waves and EMATs.
- To determine which guided wave mode would be best suited to ranging from butt weld heads for mobile robotic positioning.
- To develop an optimisation model for Lorentz force PCB coil PPM EMATs to improve sensor efficiency which may be applied to bi-directional and unidirectional EMATs.
- To create optimised EMATs to generate the wave mode determined to be best suited for ranging from welds.

1.6. Contributions to Academia and Industry

This thesis presents a study on determining the guided wave mode best suited to guided wave echolocation relative to welds. It was found that from the modes tested SH1 had the highest reflection coefficient and it was found that this was due to the modes energy density distribution favouring the edge boundaries of the carrying plate. This work was published in IEEE Sensors [23].

Following this, an EMAT sensor was developed that was specifically optimised for guided wave echolocation. Firstly, a PPM racetrack EMAT optimisation model was developed to maximise the power of the guided waves produced, without increasing the strength of the background magnetic array used in the sensor as this would impede the movement of a mobile robot. A typical bidirectional PPM EMAT emits signals from both sides which increases the complexity of ranging therefore a unidirectional PPM EMAT setup was designed and the optimisation methodology was applied. Comparing this optimised EMAT to a standard industry sensor, a two times increase in signal amplitude was achieved compared to the industry sensor, additionally no ranging dead zones were found and due to the decrease in sensor setup size additional measurement steps were able to be taken. This work was published in MDPI Sensors [24].

I also supported my colleagues in several publications relating to automated inspection. A full list of papers arising from this thesis is detailed below.

1.7. Lead Author Publications Arising from This Thesis

McMillan, R., Hampson, R., Tabatabaeipour, M., Jackson, W., Zhang, D., Tzaferis, K., & Dobie, G. (2023). "Design and manufacture of an optimised side-shifted PPM 2 EMAT array for use in mobile robotic localisation." *Sensors*, 23(4), Article 2012. <https://doi.org/10.3390/s23042012>

McMillan, R., Tabatabaeipour, S. M., Tzaferis, K., Jackson, W., Edwards, R. S., Trushkevych, O., Macleod, C., Dobie, G., & Gachagan, A. (2022). "Crawler-based automated non-contact ultrasonic inspection of large structural assets." 49th Annual Review of Progress in Quantitative Nondestructive Evaluation (QNDE 2022), San Diego, United States.

McMillan, R., Tabatabaeipour, M., Hampson, R., Loukas, C., Zhao, T., Edwards, R. S., MacLeod, C. N., & Dobie, G. (2022). "Characterization of EMAT guided wave reflectivity on welded structures for use in ranging." *IEEE Sensors Journal*, 23(5), 4383-4391. <https://doi.org/10.1109/JSEN.2022.3179326>

1.8. Co-Author Publications Arising from this Thesis

Gilmour, A., Tabatabaeipour, M., McMillan, R., Tzaferis, K., Hampson, R., Jackson, W., Zhang, D., Lawley, A., Mohamed, A., MacLeod, C., Gachagan, A., Pierce, S. G., & Dobie, G. (2023). "Robotic ultrasonic inspection of large and complex structural assets." In S. Farhangdoust, A. Guemes, & F.-K. Chang (Eds.), *Structural Health Monitoring 2023: Proceedings of the 14th International Workshop on Structural Health Monitoring* (pp. 2143-2150).

Tzaferis, K., Tabatabaeipour, M., McMillan, R., Dobie, G., and Gachagan, A., “A shear horizontal phased array steering excitation technique for remnant wall thickness quantification,” *Ultrasonics*, vol. 136, no. August 2023, p. 107142, 2024, doi: 10.1016/j.ultras.2023.107142.

Tabatabaeipour, M., Tzaferis, K., McMillan, R., Jackson, W., Dobie, G., Edwards, R. S., Trushkevych, O., & Gachagan, A. (2022). “Ultrasonic guided wave estimation of minimum remaining wall thickness using Gaussian process regression.” *Materials & Design*, 221, Article 110990. <https://doi.org/10.1016/j.matdes.2022.110990>

Tabatabaeipour, M., McMillan, R., Tzaferis, K., Jackson, W., Edwards, R. S., Trushkevych, O., Dobie, G., MacLeod, C., & Gachagan, A. (2022). “Non-contact ultrasonic-based Bayesian mapping for robotic structural inspection.” Abstract from 59th Annual British Conference on Non-Destructive Testing 2022, Telford, United Kingdom. Advance online publication.

Jackson, W., Zhang, D., McMillan, R., Tabatabaeipour, M., Hampson, R., Gilmour, A., MacLeod, C. N., & Dobie, G. (2022). “Magnetic inspection platform for teleoperated remote inspections of complex geometry.” Paper presented at 49th Annual Review of Progress in Quantitative Nondestructive Evaluation (QNDE 2022), San Diego, United States.

Tabatabaeipour, M., Trushkevych, O., Dobie, G., Edwards, R. S., McMillan, R., MacLeod, C., O’Leary, R., Dixon, S., Gachagan, A., & Pierce, S. G. (2022). “Application of ultrasonic guided waves to robotic occupancy grid mapping.” *Mechanical Systems and Signal Processing*, 163, Article 108151. <https://doi.org/10.1016/j.ymsp.2021.108151>

Chapter 2

2. Literature Review

2.1. Introduction

There is a need to understand the common methods of inspection that can be used to carry out structural health monitoring of industrial assets. Firstly, detail on the characteristics of common industrial assets under inspection is given, this is to better understand the area that this research operates in. Following this the methods used to inspect the assets are explored at a high level and then the methods which are suitable for mobile robotic deployment are identified.

The current state of the art of mobile inspection crawler robots is presented, this is required to understand the current landscape of inspection robots and the methods typically used to track the position of current mobile inspection robots. Existing applications of ultrasonic guided waves and mobile robotic positioning are presented.

Common methods of mobile robotic positioning are presented to understand the applicability of guided wave ranging and the potential benefits and challenges. Following this common methods of robotic mapping are presented to give further context to the reader as ranging systems feed into mapping systems.

2.2. Structures Under Inspection

Typical industrial structures that require inspection include above ground storage tankers, industrial silos, pressure vessels and large pipelines. Large industrial plant service a variety of industries but are generally constructed in the same fashion, whereby smaller metal used sheets/plates are joined via various welding methods in order to form the structure. Tankers and pressure vessels etc., are considered plate-like structures joined with welds, although they can be large cylindrical, pipe like structures. Due to their mild curvature they can be considered plate-like. [25] shows that if the radius:thickness ratio is greater than 10:1 the effect of plate curvature on the dispersion curves is negligible.

Ferromagnetic materials such as carbon steel, grades SA516 and SA106, and stainless steel, grades 304, 316 and S275N, are frequently used for constructing industrial plant due to their low cost, mechanical strength and constructability. Alloy steels, aluminium and composite materials are also used but are application specific where lightweight construction is required or highly aggressive chemicals may be used. As these structures have large surface areas, manually carrying out a full structural health scan can be time consuming and manpower intensive.





Fig. 4 A) Typical above ground liquid storage tanks used in a variety of processing industries [26]. B) Typical industrial silos which are constructed by welding sheet metals together to form the larger structure [27]. C) Another example of an above storage tanker, the welds use to join the plates can be clearly seen here [28]. D) An example of a typical pressure vessel design, butt welds can be seen around the structures circumference and at the underside supports [29].

Welds are commonplace within these large structures, so are ideal for use as a consistent reflector that a mobile robot could use to localise itself. Common weld types, Fig. 5, that are used to join plate-like structures include butt joints, lap joints, tee joints, corner joints, and edge joints [30]. To create the joints to connect plate-like structures a number of welding methods can be used [30]. Metal Inert Gas (MIG) welding is an arc welding process that utilises a continuously fed wire electrode and a shielding gas to prevent contamination, which is typically argon or a mixture of argon and carbon dioxide. MIG welding is commonly used due to its high speed, ease of automation, and suitability for welding thick plates. Stick welding or shielded metal arc welding uses a consumable electrode coated in flux to create weldment. Tungsten Inert Gas (TIG) welding uses a non-consumable and a shielding gas, typically argon, to apply weld.

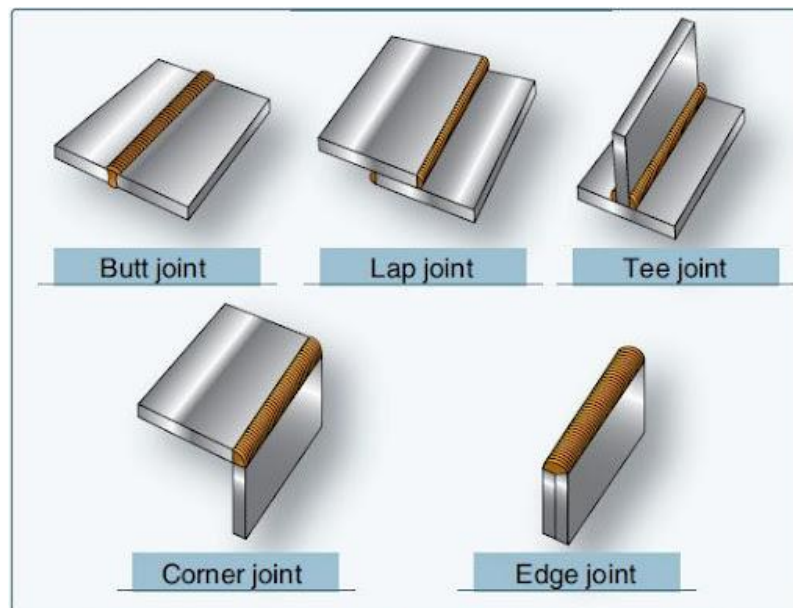


Fig. 5 Exemplar diagrams of butt, lap, tee, corner, and edge joints. Adapted from [31].

The majority of research on the interaction of bulk and guided ultrasonic waves with welded sections is typically focussed on the detection of defects within the weld, rather than utilising the returning reflections from the weld [32], [33], [34], [35], [36], [37], [38], [39], [40]. The focus of this investigation is to achieve consistent local ranging. Achieved by reflecting transmitted guided waves from welds in order to localise a given inspection system, so in this case the weld is used as a geometric reference.

2.3. Non-Destructive Inspection Techniques

There are many different inspection techniques available, each suited to the inspection of different geometries and scales. They also differ in the underlying physical phenomenon and rely on making the choice specific to the type of material under inspection and the type of expected defect. Inspection techniques can be categorised into two classes based on the areas they interrogate; volumetric and surface/near-surface. Volumetric techniques

allow for the interrogation of the interior geometry of the component include ultrasonic testing, and radiography [41]. Surface and near surface techniques include techniques such as visual inspection, eddy current testing, dye penetrant inspection [41].

2.3.1. Ultrasonic Inspection

Ultrasonic waves are the mechanical, elastic vibrations of particles within a subject at frequencies above 20 kHz and can be utilised for inspection purposes in a number of ways. There are three distinct types of ultrasonic waves which are generated through a number of means and can be used for various inspection methods; bulk ultrasonic waves; surface acoustic waves; ultrasonic guided waves. Ultrasound can be generated and measured using several approaches, including the piezoelectric effect, electromagnetic induction and thermo-acoustics. Ultrasonic inspection measurements use the time of flight of the path a wave is expected to travel compared to the measured time of flight to detect defects. If a bulk ultrasonic wave is received sooner than expected when measuring a subject of a given thickness, it indicates that there is a defect present within the waves propagation path [41], [42], [43]. Bulk ultrasonic waves are subject to attenuation, attenuation occurs largely because of the energy absorbed by the material and the scattering of the wave.

2.3.1.1. Piezoelectric Transducers

Piezoelectric transducers are the most common type of ultrasonic transduction method, Fig. 6. [44]. When a piezoelectric material is deformed by external pressure electric charges are generated on the surface, if the material is put under tension the charges are reversed. If a piezoelectric material is placed between two electrodes and an electric potential is applied, the material changes shape, this is the inverse piezoelectric effect. If an alternating voltage is applied across the piezoelectric material a mechanical oscillation which is directly proportional to the voltage is produced, this mechanical oscillation can be utilised to generate ultrasonic waves, likewise a voltage is produced if piezoelectric material is vibrated [41].

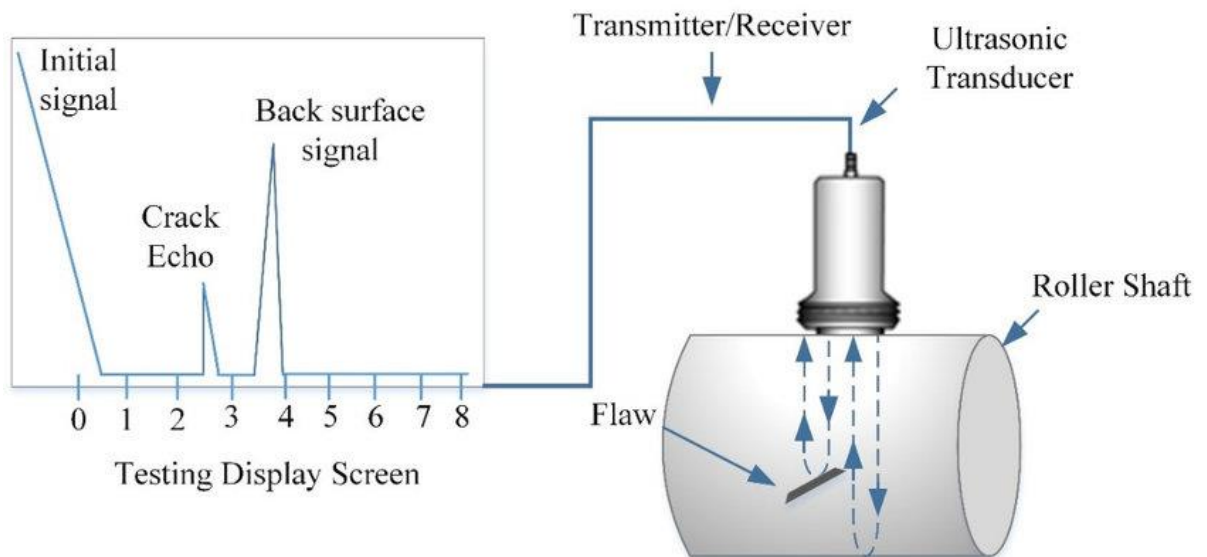


Fig. 6 A typical bulk ultrasonic inspection, the faster returning signal implies the presence of a flaw in the subjects bulk material, adapted from [20].

2.3.1.2. Phased Array Transducers

Ultrasonic phased array sensors can be used to generate a wavefront of ultrasonic waves using an array of piezoelectric transducers placed side by side in a row [41], as well the

individual elements can be pulsed at varying times. Controlling the time of transduction can be used to create delays in transmission and reception across the transducers which allows phenomena like beam steering/angling and beam focusing, Fig. 7. [45]. Beam manipulation using ultrasonic arrays allows multiple point inspection from a single probe or position, which is beneficial for detection and characterisation due to the increase in information per scan [42].

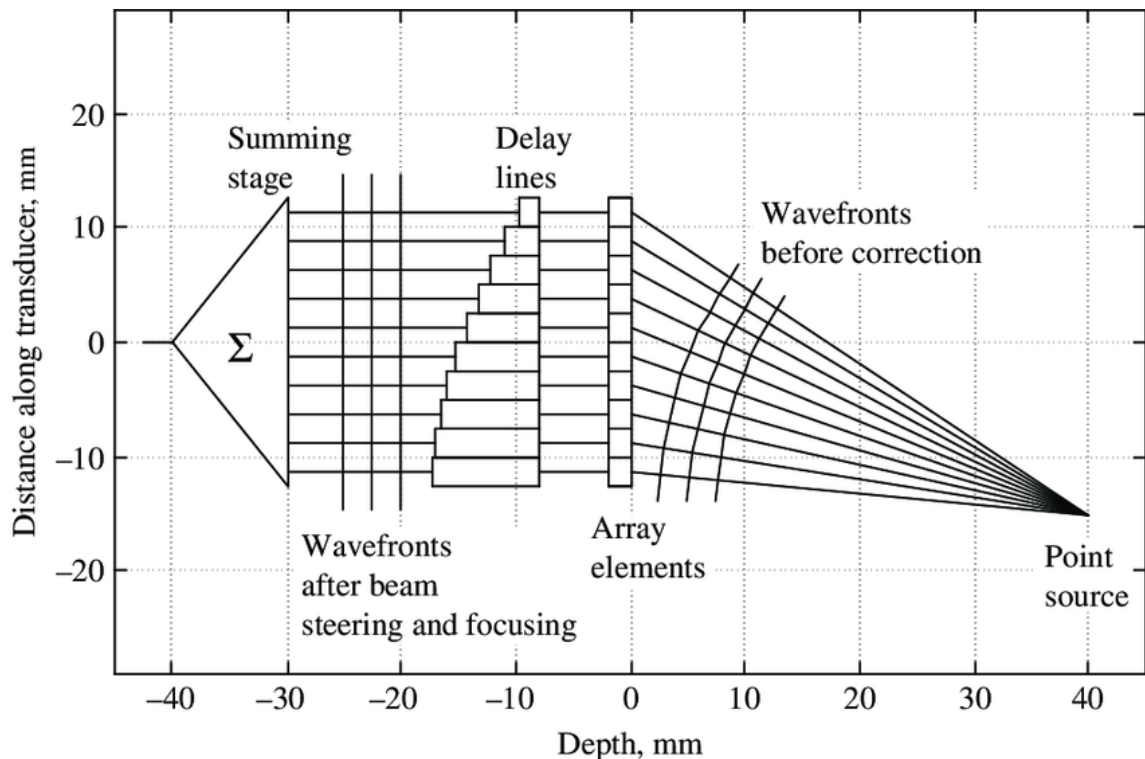


Fig. 7 Ultrasonic beam focussing can be achieved by delaying the wave launch times between each array element, adapted from [21].

2.3.1.3. Electromagnetic Acoustic Transducers

Electromagnetic acoustic transducers (EMATs) utilise electromagnetic phenomena to generate ultrasonic waves directly within an electrically conductive material. EMATs in their simplest form are an alternating current pulsed through a coiled wire, this creates an

alternating magnetic field [46]. When an alternating current is placed close to the surface of a conductive subject, a mirrored eddy current is induced within the subject. This eddy current interacts with the alternating magnetic field generating a Lorentz force. The electrons in the eddy current transfer their momentum, created by the Lorentz force, via elastic collision which creates a vibration that forms an ultrasonic waves [46], [47], [48]. In practice using only a coil generate waves is not practical as the strength of the wave created is very low due to the weak magnetic field from the coil. Real world use of EMATs typically requires a strong background magnetic field to increase the Lorentz force. This is typically created by an array of static magnets, Fig. 8 [49], this greatly improves the strength of signal generated [46], [47], [50].

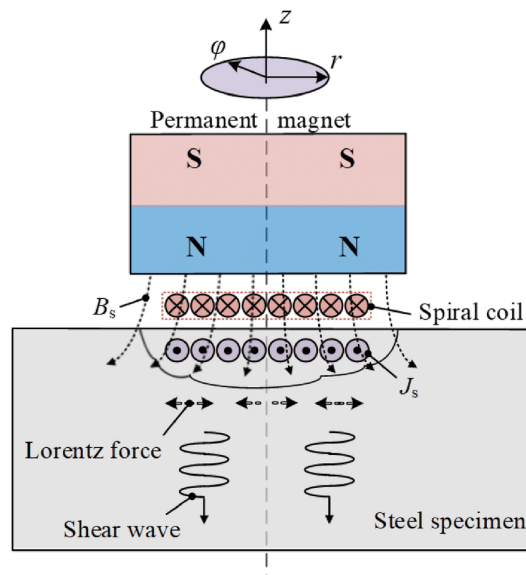


Fig. 8 A typical pancake coil EMAT is shown here, where the interactions between the permanent magnetic fields and the alternating image currents, create Lorentz forces that vibrate the subject. Adapted from [25].

EMATs are typically less efficient than other methods of ultrasonic generation as they have comparatively low transduction efficiency. Due to the nature of electromagnetics

they are non-contact which is highly beneficial for a number of applications where contact with the subject surface may not be possible, such as inspecting the subjects described in in the previous section, 2.2. Here, deployment is simplified by being tolerant to lift-off and angular misalignment, non-ideal alignment will still produce waves but signal quality will be effected compared ideal alignment. This is beneficial compared to piezoelectric crystal transducers that require perfect contact for transduction. Further benefitting from the minimal surface preparation and lack of couplant requirement. Additionally they are also the most practical way to generate shear horizontal guided wave modes [33]. This is beneficial to an application such as robotic crawlers as no couplant or surface prep is required prior to inspection

2.3.1.4. Air Coupled Transducers

Specific piezoelectric transducers can be constructed to generate ultrasonic waves within a subject via air coupling, this is non-contact method, [41], [51]. The operation principle is the same as normal piezoelectric ultrasound transduction except the impedance matching layer is made for transmission in air, Fig. 9 shows the typical transduction process.

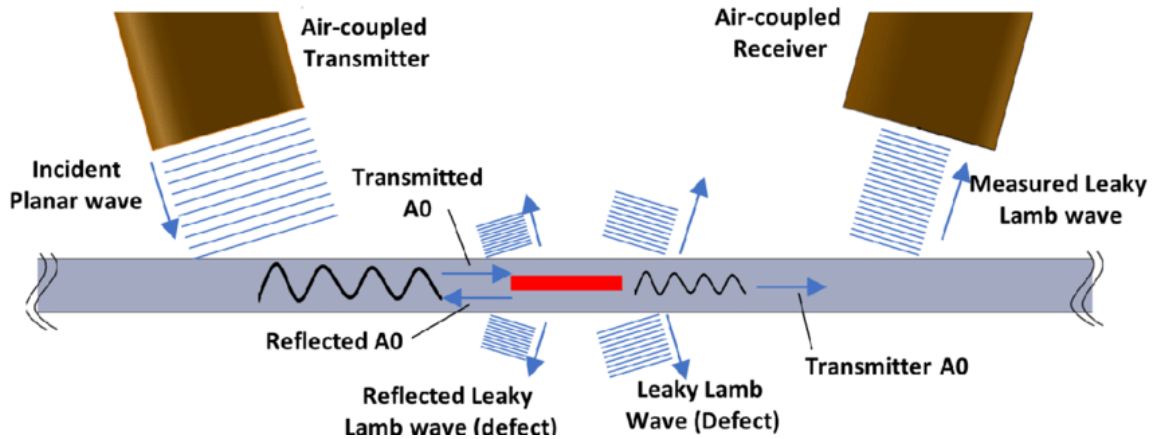


Fig. 9 An example of generation and reception of Lamb waves in a plate-like subject using air-coupled ultrasonic transmitters, discussed in [52].

The main benefits of this method are that surface contact with the subject and couplant are not required, which greatly eases the measurement process. Bulk ultrasonic, Rayleigh and Lamb waves can be generated using air coupled transducers. Air coupled transducers are typically used in industries that require composite materials as air coupled transduction of ultrasound is very effective for carrying out c-scan inspections.

Although air coupled transducers provide great benefits with non-contact transduction, high impedance mismatches due to air cause low SNR requiring more sophisticated transducers. The geometry that air coupled transducers can be used with is also limited as the energy loss from the transducer to the subject typically causes significant attenuation making it difficult to vibrate thick materials.

2.3.1.5. Laser Generated Ultrasound

Lasers can be used to generate ultrasonic waves, there are two operating principles used to generate waves via lasers depending on the laser energy and material properties, [53].

The first method utilises the thermoelastic effect. A laser pulse strikes a subjects surface

and rapidly heats a portion of the subject causing thermal expansion which generates stress within the material, this momentary stress generates an ultrasonic wave. The second method utilises the ablative effect where a high intensity laser hits a subjects surface, the energy is high enough to ablate a small portion of the materials surface. The ablation creates a high-pressure plasma that generates an ultrasonic wave. Fig. 10 A and Fig. 10 B depict both methods of laser ultrasound.

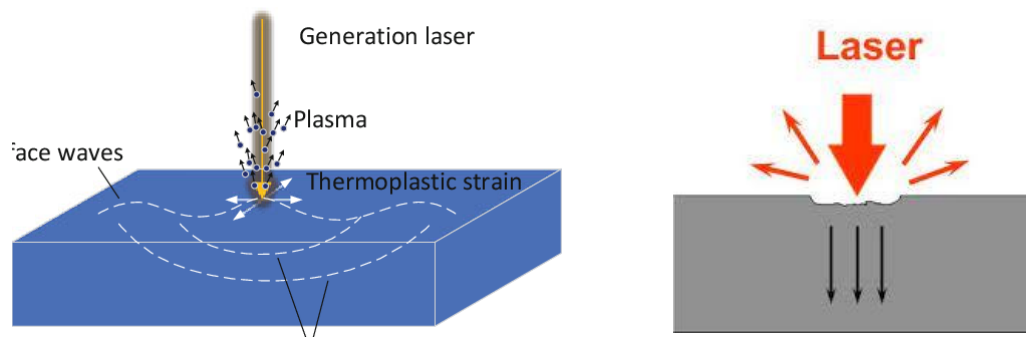


Fig. 10 A) Thermoelastic laser ultrasound generation diagram, adapted from [54]. B) Ablative laser ultrasound diagram, adapted from [53].

Laser generated ultrasound is advantageous as compared to other methods of ultrasound generation, significant separation between the generation source and the subject

2.3.1.6. Bulk Ultrasonic Inspection vs Guided Wave Inspection

Although both ultrasonic waves and can be generated with the same transducers, bulk ultrasonic waves and guided waves have different characteristics so can be used in different ways.

Typically bulk ultrasound inspections utilise time-of-flight principles to detect and characterise defects. Where returning/reflected signals are compared to transmitted signals and the change in time and signal can be measured. As well bulk ultrasound waves

can be transmitted through an area of interest from one transmitter to a receiver beyond the area of interest. The transmitted and received signal can be compared to detect/characterise defects. Guided waves can also be used for inspection through traditional time of flight (TOF) methods but are typically unable to be used to carry out detailed defect characterisation. Additionally due to the long propagation distances of guided waves, it is possible to inspect areas of a structure that cannot be evaluated with bulk ultrasonic methods in cases that the access is restricted or direct probe placement [55]. Guided waves are commonly used to detect defects in long pipelike structures from significant distances.

Multimodal generation can also be utilised whereby two or more modes are sent from a transmitter, to a receiver, through a corrosive patch for example, and due to the differences in wave characteristics such as wavelength, one mode might reach the receiver whereas the others might not. Comparing the modes which were able and unable to reach the receiver, the minimum thickness of the corrosive patch can be inferred [56].

2.3.2. X-Ray

X-rays are a form of electromagnetic radiation and can be utilised for inspection by exposing subjects to an γ -ray source and detecting the transmission on the other side of the subject. Rays used for inspection will spread uniformly from the source towards the subjects, variations in the subjects bulk makeup will cause attenuation, the attenuation will show on the detection source, creating an image that can be used for defect characterisation, Fig. 11 [41], [57]. Radiography is non-contact, can show any defect type in inspection (dependent on orientation), straightforward in operation principles and can

measure large areas quickly. However radiography expensive compared to other NDT methods, requires access to both sides of the subject which is not possible in a large amount of inspection sites and utilises hazardous radiation [58].

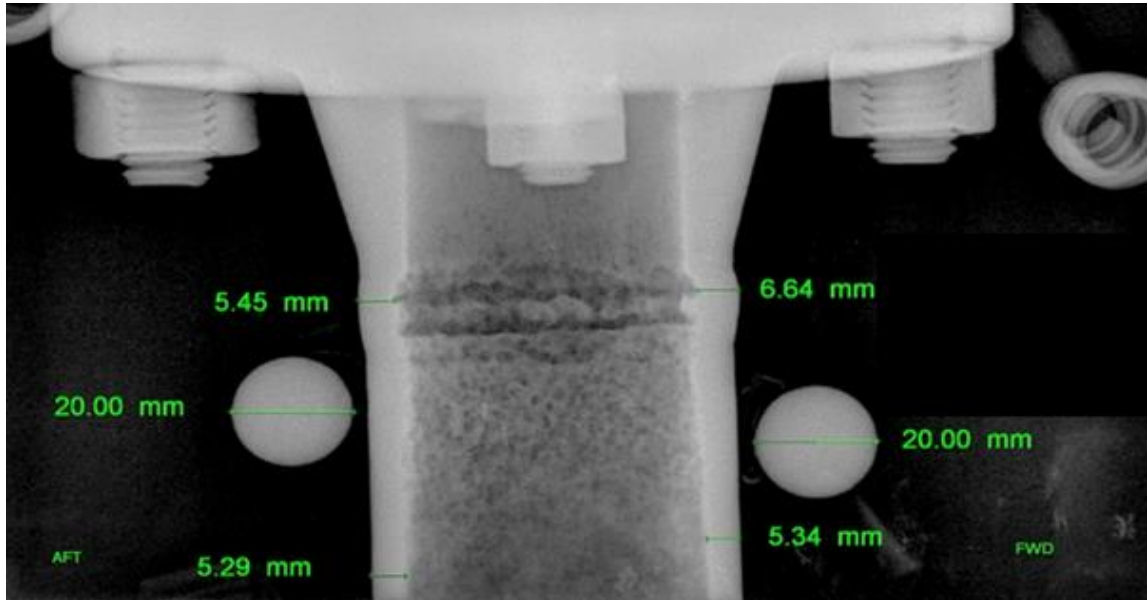


Fig. 11 Example of the result of radiographic inspection of a pipeline, the green text measurements show the measured remaining wall thickness, with the dark spotted patches representing corrosion and pitting [59]. The thicker section of dark spotting is a welded section.

2.3.3. Pulsed Eddy Current

Eddy currents can be generated by moving a wire solenoid coil close to a conductive material and running an alternating current through the coil. The resultant alternating magnetic field from the coil generates an eddy current within the material which is in opposition to the initial current, the eddy current creates its own alternating magnetic field, this magnetic field can be used to measure defects [41], [60], [61]. The eddy currents behaviour depends on the properties of the material and the geometry of the subjects

surface, flaws within the range of the eddy current alter the eddy currents path which change the magnetic field it creates, this change can be used to measure the defect [61].

Eddy currents can be utilised for surface defect depth measurement with careful calibration, Fig. 12, however this is very sensitive to sample parameters such as magnetic permeability and conductivity, which makes this difficult without prior sample characterisation [61]. Additionally they are a non-contact technique and as such can detect defects through surface coatings without removing the coating.



Fig. 12 An example of typical Eddy Current inspection measuring plate thickness [62].

2.3.4. Visual Inspection Methods

Visual inspection utilises the human eye or cameras to observe the external surface of a subject to detect visible flaws, deformations, or discontinuities. Traditionally, human inspectors perform this method, relying on experience and visual acuity to characterise defects. However, the integration of automated detection systems using digital cameras

has enhanced the reliability and efficiency of this technique. Automated systems employ advanced image processing algorithms to identify and quantify defects in real-time, offering increased repeatability and objectivity compared to manual inspection [63], [64], [65], [66]. This approach is especially useful in high-speed production environments or hazardous areas where human inspection may be limited, as it allows for consistent monitoring over extensive areas without the variability introduced by human factors.

Dye penetrant inspection (DPI) is widely adopted for identifying surface-breaking flaws, especially in metal, ceramic and plastic components as it increases small defects visibility in visual inspection. In this method, a liquid penetrant is applied to the surface under inspection, allowed to dwell, and then removed to reveal defects where the penetrant remains trapped [41]. DPI is simple in principle, cost-effective and highly sensitive to small cracks or porosity. However, it requires thorough pre-inspection cleaning to prevent contaminant interference and necessitates proper post-inspection cleaning to remove chemical residues. Moreover, dye penetrant inspection is limited to open-surface flaws and may prove impractical for large-scale operations if repeated applications or extensive surface preparation are required.

2.4. Current State of the Art of NDT Robotic Crawlers

Robots are able to be safely sent into dangerous areas, such as pipelines at the bottom of oil rigs [2] or pipelines in a nuclear plant [14][67]. In scenarios like this the robot is typically remotely controlled by the inspector whilst they remain outside the hazard area. The majority of commercial crawlers are remote controlled where scanning paths and the

scanning area is managed by an experienced operator using a remote control with a screen fed by a camera system to give clear view of what surrounds the robot. Robotic crawler systems can be equipped with adhesion systems such as magnetic wheels [68] or vacuum setups [69] which allow the crawler to traverse vertical walls and ceilings, which greatly increases the areas of access for remote inspection without having to increase safety measures.

Typically a crawler inspection robot will be equipped with cameras for visual inspection and an ultrasonic or eddy current sensor which the operator will use to take thickness measurements of a subject, Fig. 13. Remote Visual Inspection (RVI) robots can be used to access extremely difficult to reach areas, such as down pipelines or tanker ceilings, this allows the operator to closely inspect the surface of a given area without requiring access.



Fig. 13 The Waygate Technologies BIKE, equipped with manipulating arm and a piezoelectric ultrasonic transducer. This robot is remote controlled and the operator utilises the camera in between the lights to inspect the subject. Adapted from [47].

A single sensor robot can also be used to carry out automated line scanning or single point scans. Robotic crawlers have been developed to carry out semi-automated raster scans, see the Gecko Robotics R-AUT [70], this allows an operator to create a high quality thickness map of a small perimeter of a subject. Robotic systems which piece together different scans to form a larger map are required to accurately track position at each measurement through accurate sensor positioning, otherwise the information will be inaccurate and unusable.

Although robotically driven inspection systems are a great improvement upon manual inspection methods, a crucial factor which makes an inspection robot successful is the

system's ability to accurately capture the position of each measurement in the scan. Inaccuracies in positioning will lead to a measurement or a group of measurements incorrectly representing an area of a subject, resulting in incorrect thickness estimations. Positional tracking can be carried out in a number of ways which is covered in a later section.

Table 1 below, lists a current state of the art industrial robotic inspection crawlers.

Table 1 – State of the Art of Ultrasonic Robotic Inspection Systems

| Robot, Manufacturer | Positioning Sensors | Control | Locomotion | Inspection Method |
|---|---|---|--|---|
| Scorpion 2 [68], Eddyfi | Twin encoders separate from magnetic wheels | Inspector via remote control w/o visual | 4x Magnetic wheels | 1x Probe, dry coupled ultrasound |
| Magg 310 R-Scan [71], Eddyfi | Track mounted encoders | Inspector via remote control w/ visual | 2x Inuktun tracks and belly magnets | 1x Probe, dry coupled ultrasound 1x camera, for RVI |
| VR Inspection Robot [72], University of Strathclyde, CUE, Mobile Robotic Inspection Team | Track mounted encoders | Inspector via remote control w/ visual | 2x Inuktun tracks and belly magnets | 6x Wide angle lens cameras for Virtual Reality headset for visual inspection |
| Saddle weld inspection robot [72], University of Strathclyde, CUE, Mobile Robotic Inspection Team | Motor and idle wheel encoders | Inspector via remote control w/o visual | 4x Magnetic wheel articulated base, Jireh Navic 2 [73] | 1x Phased array probe deployed via 6 DOF robotic arm |
| RMS 2 Corrosion Mapper [15], Eddyfi | X/Y Encoders in scanning head manipulator and built in wheel encoders in drive system | Inspector via remote control w/o visual | 4x Magnetic Wheels | 1x Ultrasonic immersion Probe, on a 100mm track for raster scans |
| Stingray - API 635 Tank Floor Cleaning and Inspection [74], Diakont (CA, US) | Fibre optic gyroscopes | Inspector via remote control w/o visual, utilises Sonar for localisation in tanks | 4x Wheels, with water jet and power scrubbing capabilities | 64x Magnetic flux leakage sensors, 96x ultrasonic sensors |
| RUG (Rapid Ultrasonic Gridding) [75], Gecko Robotics (PA, US) | <i>Unlisted</i> | Inspector via remote control w/o visual | Gecko TOKA magnetic wheel platform | 24x Ultrasonic probes |

| | | | | |
|---|--|---|---|--|
| R-AUT (Rapid Automated UT) [70], Gecko Robotics | Built in motor and idle wheel Encoders | Inspector via remote control w/o visual | 4x Magnetic wheel articulated base, Jireh Navic 2 [73] | 64 Element dual linear phased array probe, on a moving track for raster scanning |
| Tripod [76], Jireh (AB, CA) | Built in magnetic wheel encoders | Inspector via remote control w/o visual | 3x Magnetic wheel articulated base | 1x Ultrasonic probe deployed via 6 DOF robotic arm |
| Terax [77], Jireh | Built in track motor encoders | Inspector via remote control w/ visual | 2x Tank tracks | Visual inspection via camera |
| SAW Bug Weld Scanner [78], Pheonix | Built in magnetic wheel encoders | Inspector via remote control w/o visual | 4x Fixed magnetic wheels, for traversing pipe circumferences in one plane | Up to 6x ultrasonic transducers for weld inspection |
| Accutrak [79], AUT (TX, US) | Y Encoder in scanning head manipulator and built in wheel encoders in drive system | Inspector via remote control w/o visual | 4x Magnetic wheel split platform | 1x Configurable ultrasonic probe on moving track for raster scans |
| BIKE [80], Waygate Technologies (PA, US) | Built in magnetic wheel encoders | Inspector via remote control w/ visual | 4x Magnetic wheel highly articulated base | 1x Ultrasonic probe, 1x camera with lighting |
| ALTISCAN [81], Roboplanet (FR) | Built in magnetic wheel encoders | Inspector via remote control w/o visual | 4x Magnetic wheel base | 1x Ultrasonic sensor |
| SteerROVER [82], Olympus (JP) | Built in Motor and Idle Wheel Encoders | Inspector via remote control w/o visual | 4x Magnetic wheel articulated base, Jireh Navic 2 [73] | 1x Configurable ultrasonic probe on moving track for raster scans |

The Eddyfi Scorpion 2 [68] is an example of a typical commercial magnetic wheeled remote controlled inspection robot, Fig. 14. The inspection method of the Scorpion 2 is a dry coupled ultrasonic wheel probe which can carry out automated continuous point and line scans. This system was designed to carry out thickness measurements on subjects such as large ferromagnetic tank vessels, the magnetic wheels allow the crawler to traverse the walls and easily access the roof of large ferromagnetic industrial structures. The individual point scans can be combined to form a b-scan of the line which has been

scanned. Twin external roller encoders are used to track the position of the robot as it traverses a subject, they can be seen in Fig. 14A between the front and back magnetic wheels.



Fig. 14 A) The Scorpion 2 vertically traversing a ferromagnetic above ground tanker wall [83]. B) A close shot of the Scorpion 2 showing the dry coupled sensor head [84].

The Rapid Automated Ultrasonic Testing (R-AUT) crawler produced by Gecko Robotics [70], Fig. 15, is a magnetic wheel crawler that is able to traverse large ferromagnetic structures and carry out raster scans across a subjects surface. The R-AUT utilises a dual linear array phased array sensor to carry out its thickness measurements, this probe is mounted to a motorised rail mechanism which sweeps the probe across an axis in incremental steps, the probe is continually fed couplant fluid during the scan. As the probe is automatically moved, measurements are taken, after each sweep of the probe, the robot shifts forward to begin the next sweep. Gecko Robotics carried out a case study [85] which showed using this system achieved a 70% reduction in man hours when thickness mapping a specific pipeline compared to the manually driven inspection processes previously used. Positioning of the robot is measured using a motor encoder in two of the four wheels and

an idle encoder in the two other wheels, this is a common design choice to balance positioning accuracy, cost and positional reliability. Sensor positioning is measured using the motorised rail which manipulates it. This system is an effective solution with a clear benefit over single point probe solutions, however large coverage scans will be time consuming. Operator control and intervention is still required, surface preparation is required in order to carry out the inspection and the robot's large size could limit access for inspection.

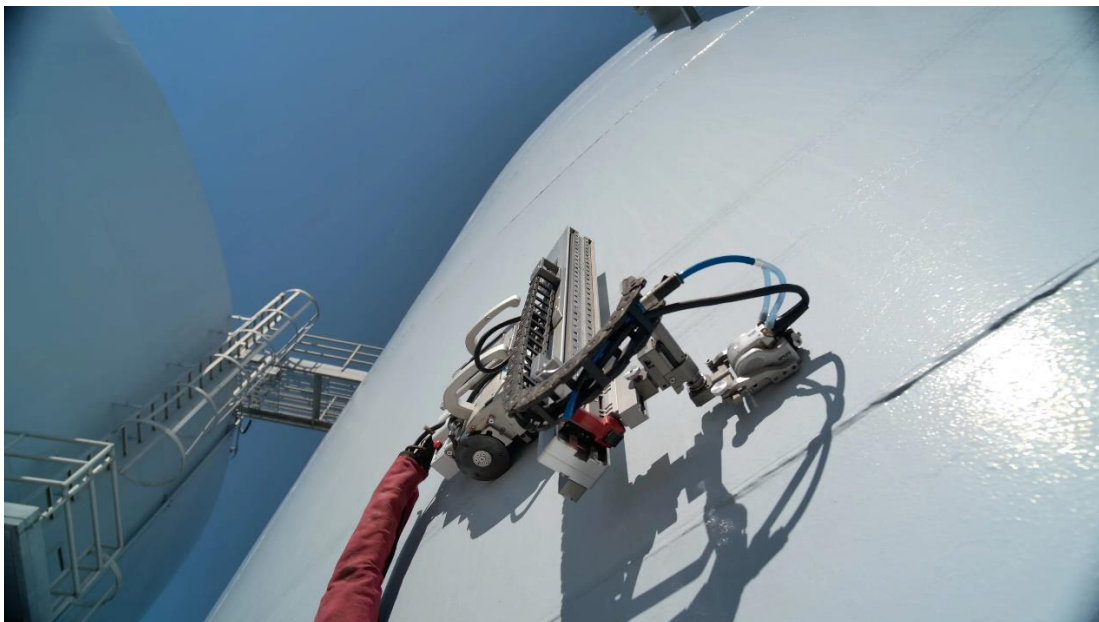


Fig. 15 The R-AUT horizontally traversing an above ground tanker, carrying out a raster scan to create a corrosion map. The ultrasonic probe is fed liquid couplant through umbilical cord, this cord also connects power and the user input to the robot [70].

2.5. Mobile Robotic Positioning Systems

When an inspection robot carries out a measurement, the position of the measurement has to be accurately recorded to complete an inspection. Repair of damaged areas can be impeded if the position has been wrongly recorded during inspection or damaged areas

could be misinterpreted as healthy which could lead to structure failure. Fig. 16 diagrammatically depicts the positional inaccuracies that can occur during inspection.

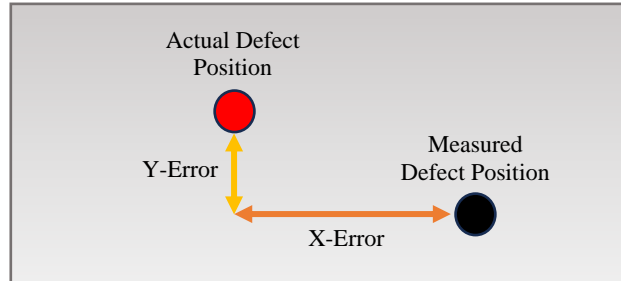


Fig. 16 Diagram illustrating defect mapping error.

There are two types of positional measurement that can be taken, absolute measurements and relative measurements. Absolute measurements do not rely on previous measurements for the current estimate, so each measurement is independent of previous measurements, this prevents measurement error build up [86]. Relative measurements build upon previous measurements to estimate the current position, this is typically accurate over short periods but builds accumulating errors overtime [86], [87].

There are two main types of positioning sensors, external sensors and internal sensors. External sensors are not attached to the robot and end to produce absolute measurements, which is the measure of a given position in a fixed global reference frame. Outdoor Global Position Systems (GPS) and photogrammetry systems are examples of external sensors, however they are not practical when used in inspection robotic systems due to the relative cost of the systems compared to the cost of the robot. The industrial locations where the robots are typically used can disrupt and interfere with the operation of positioning system, the location may also be unsafe to setup an external positioning system. Additionally

outdoor systems can have an error within the metre range, this range is unsuitable for positioning in mobile robotic inspection where the scale is significantly smaller.

Internal sensing systems are attached directly to the robot, such as wheel encoders and accelerometers, internal sensing systems are easily integrated into mobile robotic designs. They typically produce relative measurements so are subject to time dependent integral error which increases over time, they are very accurate over short periods of time and don't require external systems to be setup in order to take measurements.

Accurate positional estimation and localisation is a historic problem within mobile robotics, probabilistic estimation of a robots position through fusion of multiple sensors outputs are typically used in modern robotic systems to achieve accurate positioning so that robot navigation and mapping is accurate [88], [89]. Combinations of onboard sensors and external sensors can be used, the datasets can be combined using methods like Kalman Filters to improve positional estimation. This data can be fed, real time, into a framework like Simultaneous Localisation and Mapping (SLAM) which will then control the robots navigation and trajectory. As accurate external sensing methods such as GPS are not practical in mobile robotic inspection applications, Indoor Positioning Systems (IPS) can be used. Four common types of IPS methods are Odometry, Trilateration, Optical, Inertial.

2.5.1.1. Odometry

Odometry methods are able to estimate a robots positional changes using onboard and integrated sensors, such as wheel encoders, and are able to determine the past trajectory of the robots. Positional changes in odometry methods are summated using integration

methods, the robots position its estimated relative to its starting position, as a result of this are sensitive to unbounded integral error over time [90]. The most commonly used form of odometry used in mobile robotics are encoders, encoders can be magnetic, mechanical or optical, a review of different types of encoders is given in Chapter 7 of [90]. In mobile robotics encoders, are typically used to estimate the distance travelled by a wheel or track, where the distance moved in each time step is calculated. Odometry methods provide good short-term accuracy, are relatively inexpensive and allows for high sample rates [91].

Although odometry methods naturally build up error over time due to their relative measurement method of operation, however a lot of errors can be attributed to systematic errors, such as unequal wheel diameters, and non-systematic errors, such as wheel slippage. Systematic errors can be accounted for using the University of Michigan Benchmark method [92].

2.5.1.2. Optical Methods

Utilising landmarks as localisation points for optical positioning systems is a commonly used method for indoor mobile robotic localisation [90], [91], [93]. There are two types of landmarks, natural and manmade, natural landmarks are distinct features within an environment that can automatically recognised by a system, this is beneficial as they don't have to be manually inserted into the environment prior to robotic mapping but automated determination of a natural landmark can be difficult and tend to work better in very structured environments [94]. Man made landmarks, like Quick Release (QR) codes, can be placed within an environment and used to gain an absolute measurement of a robots position [95] and are highly detectable [96].

In industrial situations such as warehouses, manmade landmarks are very effective methods of robotic localisation [97], [98]. In industrial inspection settings, utilisation of manmade landmarks is not feasible as the landmarks have to be placed in the environment and typically mobile robotics are used due to access issues and dangerous hazards.

Visual odometry is where a camera can be used to determine the distance moved by a mobile robot by tracking or matching features between frames to estimate the distance travelled [99]. Similar to locomotive odometry methods, visual odometry methods are subject to integral error [100], but are less susceptible to non-systematic errors and have been shown to be more reliable and accurate over longer periods of travel compared to wheel odometry [101].

2.5.1.3. Trilateration Methods

Trilateration localisation methods measure the position of a mobile vehicle using relative distance measurements to three or more transmitter beacons, the beacons have to be placed at known locations within the environment of the inspection area with a receiver onboard mounted to the mobile robot [91]. Time-of-flight information is used to calculate the relative distance from the robot to the beacons which can then be used to locate the robot within the environment providing an absolute measurement of the robots position. Indoor Global Positioning Systems (iGPS) such as the Marvel Mind [102] can be used, but in the case of inspection zones in dangerous environments the beacons would need to be able to placed in the environment by a worker which goes against the idea of utilisation of robotic methods of NDT to keep workers safe. Manufacture of future industrial assets which will

be expected to require inspection could potentially include beacons within their design which would make them ready for use with trilateration positioned mobile robotic systems.

2.5.1.4. Inertial Measurement Units

Inertial Measurement Units (IMU) are small onboard sensors, they can be used to estimate the orientation, velocity and position of a robot [103], [104], [105]. An IMU is a proprioceptor where it senses changes within the mobile robot system instead of movements or changes within the environment the robot is in. Compared to exteroceptive sensors, ultrasonic and laser range finders, IMUs have reduced inaccuracies associated with the environment. IMUs are able to estimate the orientation of an object and this is typically achieved by utilising an IMU with 9 Degrees of Freedom (DOF), which has a 3-axis accelerometer, a 3-axis gyroscope and a 3-axis magnetometer.

IMUs are not best suited for robot navigation, determining displacement is carried out by double integration of accelerometer readings which creates integral errors [90], [106], [107]. In industrial environments where ferrous objects are common, the magnetic field vector estimated by an IMU is subject to interference from local magnetic fields, in addition to this there are typically magnetic materials present on mobile robotic crawlers

[108]. As the angular acceleration is integrated to find the angular change, gyroscopes are also subject to integral error.

2.5.1.5. Examples of Robotic Positioning Systems in Literature

Table 2 below presents some examples of common positioning methods found in academia.

Table 2 – Examples in literature of common positioning methods for mobile systems.

| Positioning Method | Onboard/External | Positioning Error |
|---|---|----------------------------|
| Laser Positioning (Pose Tracking) [109] | Onboard | +/- 5.3cm (Minimal Error) |
| Radio Waves (Extended Kalman Filter) [110] | Onboard | +/- 23cm (Minimal Error) |
| Odometry (IMU and Encoder) [111] | Onboard | +/- 50cm (Maximal Error) |
| Camera/Laser Data Fusion (Extended Kalman Filter) [112] | Onboard | +/- 10.3cm (Minimal Error) |
| 3D Vision System and Natural Landmarks (Extended Kalman Filter) [113] | Onboard | +/- 1.8cm (Minimal Error) |
| Vision Assisted GPS [114] | External assisted by onboard/local system | +/- 5cm (Minimal Error) |
| LiDAR (Multi-Sensor Setup) [115] | Onboard | +/- 11.1cm (RMSE) |
| Wireless Sensor Network and IMU (H Filtering) [116] | Onboard | +/- 13.1cm (RMSE) |

2.5.2. Sensing & Positioning in Commercial Robotics

Products driven by automated exploration have grown in popularity in recent years, automated robotic hoovers and lawnmowers are key examples of this. A typical robotic vacuum cleaner will feature a number of sensors which help guide the robot around a room following a predetermined navigation style, the sensors will let the vacuum know when it has or is going to collide with an object in the room, this is a relatively simple navigational setup [117]. High end robotic vacuum cleaners such as the iRoomba 976 [118] are fitted with more sophisticated mapping and navigating procedures. The iRoomba 976 utilises wheel encoders and cameras which take images of the users home and stitches the images together to form a map which it uses to path plan. This allows the robot to more efficiently clean a room, compared to cheaper or older models which use a brute force approach.

Modern agriculture makes use of positioning and sensing systems in a variety of ways. Modern tractors are now semi or fully autonomous and make use of GPS positioning and other sensing methods in order to accurately plant seeds and manipulate soil as efficiently as possible. Semi-autonomous systems such as precision planters utilize a combination of sensors, including ultrasonic sensors and optical cameras, to detect the soil's texture and moisture levels. This data allows the system to adjust planting depth and seed spacing dynamically. High-end models also incorporate real-time kinematic (RTK) GPS technology, which provides centimetre-level accuracy, ensuring that each pass of the tractor is perfectly aligned with the previous one. These advanced systems enable farmers to maximize crop yields while minimizing input costs and environmental impact, making modern agriculture more sustainable and efficient [119].

A typical autonomous warehouse robot is equipped with a variety of sensors that enable efficient navigation within a warehouse environment. These sensors help the robot detect and avoid obstacles, ensuring smooth and uninterrupted operation. Basic models often follow simple navigational setups, such as adhering to predetermined floor markings. In contrast, high-end autonomous warehouse robots, like those utilized by Amazon Robotics, incorporate advanced technologies including LIDAR, computer vision, and RTK positioning. Amazon's first fully autonomous warehouse robot, Proteus, uses advanced safety, perception, and navigation technologies to move around facilities independently while carrying packages. This robot combines LIDAR for spatial awareness and computer vision for real-time object recognition, creating detailed maps of its surroundings to navigate efficiently without external landmarks [120]. Similarly, other robots like Amazon's Cardinal use AI and computer vision to sort packages by reading labels and placing them in the appropriate carts, enhancing accuracy and reducing manual labour [121]. This advanced mapping and navigation technology allows the robots to optimize their routes, enhance task efficiency, and adapt to new layouts or obstacles, significantly outperforming older or simpler models that rely on less precise navigation methods.

2.6. Mobile Robotic Mapping and Exploration

2.6.1. Simultaneous Mapping and Localisation

Positioning systems can provide information that is fed into automated mapping systems such as Simultaneous Mapping and Localisation algorithms. The Simultaneous Mapping and Localisation (SLAM) problem, a thoroughly researched area [82], [122], [123], [119],

allows mobile robots to map an unknown environment whilst exploring it. Currently, SLAM methodologies or similar mapping procedures, are not integrated into the control of NDT mobile robotics as a standard feature.

Typically the mobile robots utilising SLAM will be equipped with sensors measuring the robots movement and sensors which perceive the robots environment. Onboard sensors include odometry systems and trilateration methods, perception sensors can come in the form of visual camera systems, laser and LIDAR range finding systems. Mapping in SLAM is the process of taking information about the surrounding environment collected by the sensors and collating it into a useable map, mapping methods that are used in SLAM systems include Occupancy Grid Maps, Feature Maps and Pose Graphs [124]. Localisation in SLAM is the process of using the information from the onboard sensors to identify the robots pose within the environment as it is moving, localisation is a well-researched area and can be split into local and global localisation problems. When there is no prior information on the robots position this is global localisation, when there is prior information available on the robots pose this is known as local localisation which is the localisation problem occurring in SLAM.

Mapping and localisation are thoroughly explored areas but combining the two areas in real time is the true complexity of the SLAM problem. Combining the two areas can be defined by the following equations [88], [122], [125] and [124]. Where \mathbf{x}_k is the state vector describing the location and orientation of the vehicle, \mathbf{y}_k is the control vector, applied at time $k - 1$ to drive the vehicle to a state \mathbf{x}_k at time k , \mathbf{m}_i is the vector describing the location of the i th landmark whose true location is assumed time invariant,

\mathbf{z}_{ik} is the observation taken from the vehicle of the location of the i th landmark at time k . When there are multiple landmark observations at any one time or when a specific landmark is not relevant to the discussion, the observation will be written as \mathbf{z}_k .

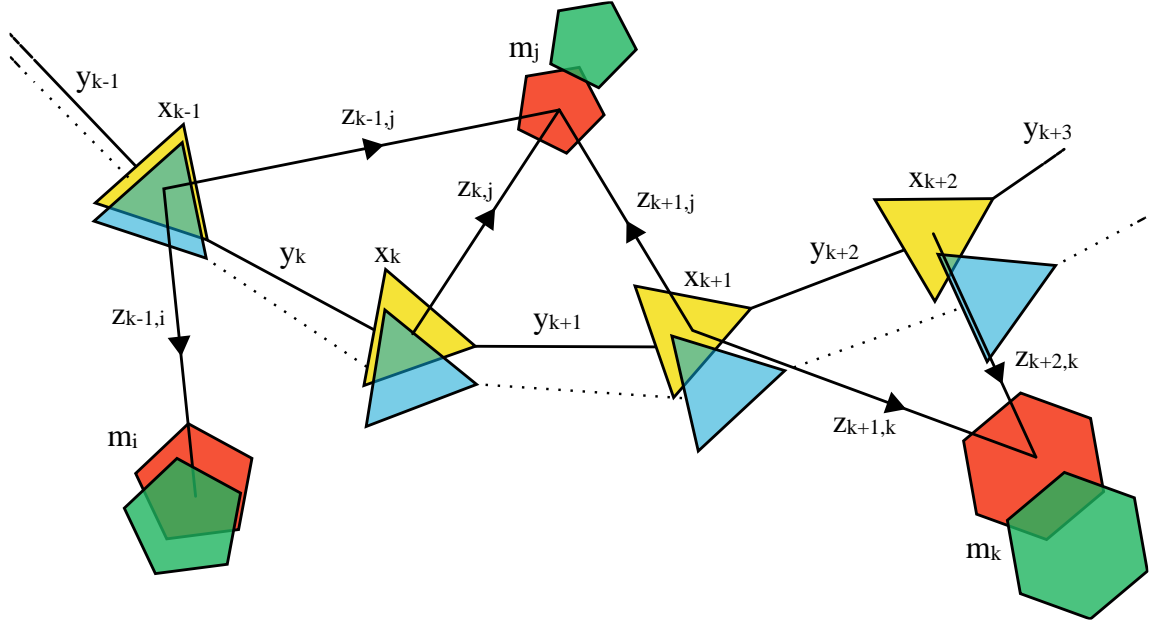


Fig. 17 The yellow triangles depict the history of the robots true pose and the blue triangles represent the history of the robots estimated pose. The red shapes represent the true position of the observed landmarks and the green shapes represent the robots estimation of the observed landmarks. The arrows depict the robots observation of the landmarks.

The following sets are also required:

Where $\mathbf{X}_{0:k} = \{\mathbf{x}_0, \mathbf{x}_1, \dots, \mathbf{x}_k\} = \{\mathbf{X}_{0:k-1}, \mathbf{x}_k\}$ gives the history of the vehicle locations.

Where $\mathbf{Y}_{0:k} = \{\mathbf{y}_1, \mathbf{y}_2, \dots, \mathbf{y}_k\} = \{\mathbf{Y}_{0:k-1}, \mathbf{y}_k\}$ gives the history of control inputs.

Where $\mathbf{m} = \{\mathbf{m}_1, \mathbf{m}_2, \dots, \mathbf{m}_n\}$ gives the set of all landmarks.

Where $\mathbf{Z}_{0:k} = \{\mathbf{z}_1, \mathbf{z}_2, \dots, \mathbf{z}_k\} = \{\mathbf{Z}_{0:k-1}, \mathbf{z}_k\}$ gives the set of all landmark observations.

The probability distribution that is computed for k at all times which describes the joint posterior density of the landmark locations and vehicle state is given in (2.1).

$$P(\mathbf{x}_k, \mathbf{m} | \mathbf{Z}_{0:k}, \mathbf{Y}_{0:k}, \mathbf{x}_0) \quad (2.1)$$

The observation model for the probability of making an observation \mathbf{z}_k when the vehicle location and landmark locations are known is described by (2.2).

$$P(\mathbf{z}_k | \mathbf{x}_k, \mathbf{m}) \quad (2.2)$$

An assumption can be made that once vehicle location and map are defined, observations are conditionally independent given the map and current vehicle state. The motion model for the vehicle can be described by (2.3) in terms of probability distribution on state transitions.

$$P(\mathbf{x}_k | \mathbf{x}_{k-1}, \mathbf{y}_k) \quad (2.3)$$

The algorithm is then split into a standard two-step recursive prediction correction form, with (2.4) giving the time update and (2.5) giving the measurement update.

$$P(\mathbf{x}_k, \mathbf{m} | \mathbf{Z}_{0:k-1}, \mathbf{Y}_{0:k}, \mathbf{x}_0) = \int P(\mathbf{x}_k | \mathbf{x}_{k-1}, \mathbf{y}_k) \times P(\mathbf{x}_{k-1}, \mathbf{m} | \mathbf{Z}_{0:k-1}, \mathbf{Y}_{0:k-1}, \mathbf{x}_0) d\mathbf{x}_{k-1} \quad (2.4)$$

$$P(\mathbf{x}_k, \mathbf{m} | \mathbf{Z}_{0:k}, \mathbf{Y}_{0:k}, \mathbf{x}_0) = \frac{P(\mathbf{z}_k | \mathbf{x}_k, \mathbf{m}) P(\mathbf{x}_k, \mathbf{m} | \mathbf{Z}_{0:k-1}, \mathbf{Y}_{0:k}, \mathbf{x}_0)}{P(\mathbf{z}_k | \mathbf{Z}_{0:k-1}, \mathbf{Y}_{0:k})} \quad (2.5)$$

This model of SLAM described above relies on the use of observational landmarks, \mathbf{m} , whereby prominent features in the environment are utilized as beacons for the robot to continuously localize itself against as it moves through each time step.

Grid-Based FastSLAM [126] is a method which looks to integrate the control of robots motion through active localization and using a strategy whereby a robot makes multiple visits to the same location in order to reduce map error. This methodology utilises active-loop closing, where the vehicle returns to known portions of the map in order to reduce uncertainty and improve map accuracy. The model creates a 2D grid map of an environment, where free space and boundaries are represented by white and black dots respectively, and unexplored space is shown as grey area. This is highly applicable for usage in mapping using guided waves, where thickness feature maps can be easily expressed in a 2D grid map. Further to this returning to the same location is beneficial for defect detection and characterization as this presents an opportunity to scan a defect again from a different angle [123].

2.6.2. Occupancy Grid Mapping

Occupancy Grid Mapping (OGM) is a probabilistic mapping algorithm for generating a 2D grid map from noisy, uncertain sensor data, with the assumption that the robot pose is known [122].

In practice the OGM model simply partitions a 2D environment into cells with each being the probability of three states including free, occupied, and unknown, the sensory input for the OGM in this work is guided wave ranging measurements. Cells can be described as one of three states; white cells represent free space, which the robot has likely moved through; black cells represent occupied space, likely boundaries or defects; grey cells represent unknown space which has not been measured yet. In the map each cell which has been detected by the sensory input is given an initial value of 0.5, a grey cell, which

updates overtime so can range from 0 to 1, 0 for a white cell, 1 for a black cell, as the vehicle senses the cell and uncertainty decreases about its state.

An example of an occupancy grid map where guided waves are utilised as the sensory input is shown by [127]. In this work a robot atop a steel plate utilises guided waves to map the boundaries of the plate. The grid map was generated using the wave reflections. When generating guided waves which reflect from the plate boundaries, the cell probability values which represent the position of the plate boundaries are initially 0.5. As the robot drives closer and stronger reflections return from the plate boundaries, the uncertainty of the wall cells being occupied starts to increase, as such their cell states move from 0.5 towards 1. The closer the robot moves to a given boundary the more the uncertainty increases and as a result the cells value move towards 1. A cell value close to 1 means that there is a high probability that cells represent a boundary or plate defect in the real world. The same process occurs for free space where the cell value moves towards 0. It can be said that the further a cells value moves from its initial value, the less uncertainty surrounding its state.

2.6.3. Mobile Robotic Inspection Crawlers Utilising Guided Waves for Mapping/Localisation Purposes

Robotically deployed guided wave inspection and localisation systems is a new area of robotics beginning to be explored. To the best of the authors knowledge this is the current literature available on this subject.

Work carried out which the author of this thesis has collaborated on, [127], is an early example of fusing guided wave inspection into the path planning of a robotic crawler for efficient thickness mapping. In this work SH0 was used, as it is non-dispersive, as the sensory input for a transmitter model that operated within an OGM, where occupied cells would represent plate reflectors such as walls/boundaries or defects, white cells would represent featureless bulk material of the plate and grey cells or unknown or unscanned areas of the plate.

The OGM system was then simulated with a bidirectional EMAT transmitter and two EMAT receivers, a sensor model was created for this EMAT setup to represent it in the OGM algorithm. Two receivers were used in order to identify the direction of propagation, as a bidirectional transmitter produces waves propagating forwards and backwards. After incorporating the sensor model into the OGM, the model was simulated. In this simulation however the robots path was predefined, as at this point in the work a proof of concept was needed to show that guided waves could be used to map and range before moving to a fully automated path planning and mapping system. Automated path planning will be carried out in future work so that robot performs SLAM when in operation.

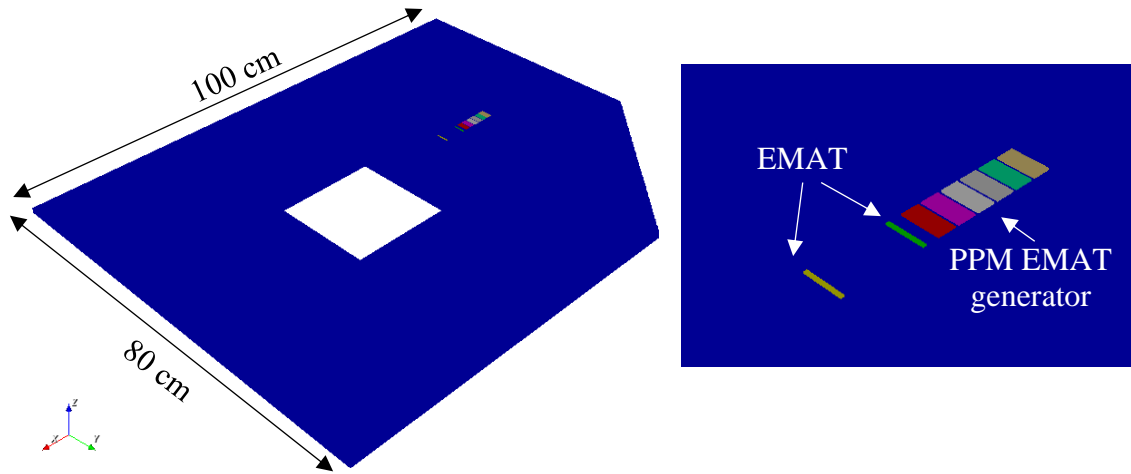


Fig. 18 Image of the simulated plate and transducer setup used for generating and detecting SH0 at different positions on the sample.

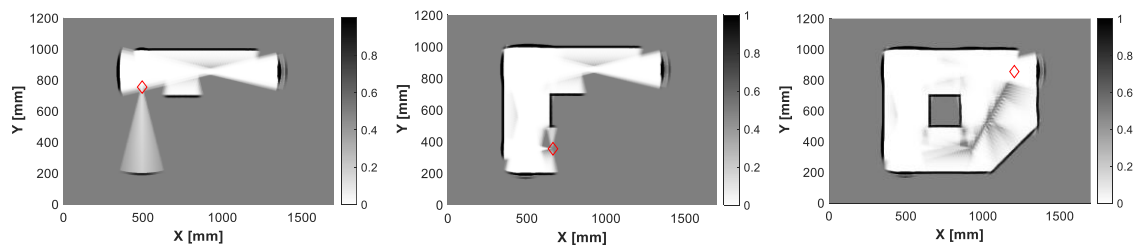


Fig. 19 The robot pose is represented by the red diamond, as it is moving across the plate it is generating SH0 waves which reflect from the plate boundaries. The boundaries are shown by the cells filled in black, as there is high certainty that a boundary is being reflected from. The white filled cells represent areas of high certainty where there are no plate features.

Fig. 18 shows the simulation setup and the sample used for test, Fig. 19 shows the simulation results. The red diamond represents the robot crawler and the position of the transducer setup, this diamond moves across the surface of the sample generating guided waves in the plate. As the robot moves and guided waves are received cells turn from grey, unknown, to white or black which is free or occupied respectively. As the robot continues to move the edges of the plates become clear and the full shape can be seen. This

simulation proved that guided waves could be used as the sensory input for ranging and mapping, the ultimate goal for this system is to develop a robotic crawler that can autonomously build a structural map of a ferromagnetic subject.

A system that was inspired by [127] was developed by Ouabi et al. [128] whereby an omnidirectional piezoelectric transducer is used to generate Lamb waves for mapping and sensory input for a magnetic robotic crawler mapping system whilst simultaneously inspecting the subject, this system uses a Bayesian occupancy grid framework similar to that in [127]. This system was shown to work experimentally where a magnetic crawler driven by an operator mapped the boundaries of a large steel plate demonstrating the efficacy of the mapping and inspection setup.

2.7. Conclusion

In this chapter the assets under inspection and their common characteristics were presented. Following this, traditional/manual methods of inspecting industrial structures was presented as well as robotically deployed inspection techniques/platforms. A review of popular robotic positioning methods was presented with their advantages and disadvantages, a brief discussion of well known mapping methods are presented to show how positioning information can be utilised.

Industrial structures were reviewed for their suitability for guided wave propagation and reflection from their geometry. They were found to be typically ferromagnetic with a plate-like geometry joined via welds. This offers a common fixed localisation points and a medium suitable for guided wave generation with EMATs.

Current state of the art robotic inspection systems are equipped with a variety of positioning sensors which were reviewed and their characteristics were summarised in Table 2. It can be seen that utilising guided waves for positioning of an inspection robot in the environments described in section 2.2 that guided waves would be a good fit due to; ferromagnetic structure allows EMATs to be used for non-contact generation which requires minimal surface prep and no couplant medium; guided waves are thought to have suitable distance coverage to be practically useful for mapping and can propagate to inaccessible areas; utilising guided waves generated onboard the robot would provide a means to determine an absolute location within the structure where other methods can have issues.

As EMAT generated guided waves are going to be investigated for their applicability for ranging to position a mobile robot, a review of guided wave behaviours and EMAT operating principles are presented in the following chapter. As well a review of relevant EMAT designs and technologies are discussed.

The current state of the art of mobile inspection crawler robots is presented, this is required to understand the current landscape of inspection robots and the methods typically used to track the position of current mobile inspection robots. Existing applications of ultrasonic guided waves and mobile robotic positioning are presented.

Common methods of mobile robotic positioning are presented to understand the applicability of guided wave ranging and the potential benefits and challenges. Following this common methods of robotic mapping are presented to give further context to the reader as ranging systems feed into mapping systems.

Chapter 3

3. Electromagnetic Acoustic Transducers and Guided Waves

3.1. Introduction

This chapter delves into the physics of ultrasonic guided wave propagation. A deeper understanding of guided waves was required to understand the reflection and propagation characteristics of different wave modes within welded structures.

As EMATs are intended to be used for generating guided waves for ranging, the underlying physics of Lorentz force generation in EMATs and the process of wave reception needs to be understood. This fundamental understanding of EMATs was required to be able to create the optimisation methodology detailed in Chapter 5. Prior works detailing EMAT builds which are related to the design and construction of PPM bi-directional and uni-directional racetrack coil EMATs are presented.

3.2. Ultrasonic Guided Waves

3.2.1. Bulk Ultrasonic Waves

To understand how guided waves propagate and behave, we must first understand the propagation of bulk ultrasonic waves. Bulk wave propagation in infinite isotropic media is well documented [43], [129], [130], [131], [132], the key equations of interest for motion in an isotropic medium are described here. Bulk ultrasonic waves exist in two wave forms, shear/transverse waves and longitudinal/compressional waves, Fig. 20 shows the propagation of both.

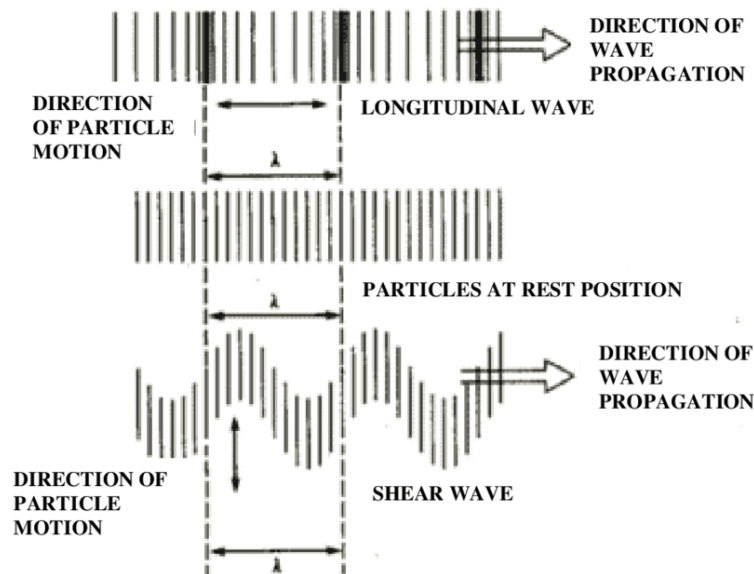


Fig. 20 Longitudinal propagation and shear wave propagation, image taken from [133].

Applying Newton's second law and the conservation of the mass within an arbitrary volume in an elastic solid, Euler's equation of motion can be derived. Euler's equation can be written as (3.1), when the materials density, ρ , is constant and is linearly elastic. The body forces can be neglected. Where \mathbf{u} is the total displacement vector.

$$\rho \cdot \left(\frac{\partial^2 \mathbf{u}}{\partial t^2} \right) = \nabla \cdot \vec{\sigma} \quad (3.1)$$

Where the stress tensor, $\vec{\sigma}$, is directly proportional to the strain tensor, $\vec{\varepsilon}$, shown by a generalized form of Hooke's law (3.2), where C is a rank fourth order stiffness tensor.

$$\vec{\sigma} = C \cdot \vec{\varepsilon} \quad (3.2)$$

For isotropic, homogenous, linearly elastic material, it can shown that it is possible to reduce the potential 21 components of the C tensor to two material components, λ and μ , which are known as the materials Lamé constants [130]. Expressing the strain tensor in terms of displacement, Hooke's law can be written as:

$$\vec{\sigma} = \lambda \nabla \cdot \mathbf{u} + \mu (\nabla \mathbf{u} + \mathbf{u} \nabla^T) \quad (3.3)$$

Where \mathbf{I} is the identity matrix for second -order stress tensor. Combining equations (3.1) and (3.3) results in Navier's differential equation of motion for isotropic elastic medium:

$$(\lambda + \mu) \nabla \nabla \cdot \mathbf{u} + \mu \nabla^2 \mathbf{u} = \rho \left(\frac{\partial^2 \mathbf{u}}{\partial t^2} \right) \quad (3.4)$$

(3.4) can be rearranged to better show the components of wave propagation in an elastic solid using Helmholtz Decomposition/wave equation decomposition. The first section of the left hand side shows the compressional motion of a wave and the second section of the left hand side shows the rotational of a wave.

$$[(\lambda + 2\mu) \nabla (\nabla \cdot \mathbf{u})] + [(\mu \nabla) \times (\nabla \times \mathbf{u})] = \rho \left(\frac{\partial^2 \mathbf{u}}{\partial t^2} \right) \quad (3.5)$$

Compressional + Rotational

Typically for NDT applications a material damping model which describes constant loss of displacement per wavelength travelled is used [134], [135], [136]. Damping of the material means that the Lamé constants can be substituted with (3.6) and (3.7), where μ' and λ' are the viscoelastic constants and ω is the angular frequency.

$$\lambda = \lambda + \frac{\lambda'}{\omega} \quad (3.6)$$

$$\mu = \mu + \frac{\mu'}{\omega} \frac{\partial}{\partial t} \quad (3.7)$$

If the above constants are zero, then the material is purely elastic so there is no damping, which is described by (3.5). When the constraints are non-zero the material exhibits viscoelastic behaviour, introducing damping. (3.5) can then be rewritten as (3.8), where frequency-dependent terms are included.

$$(\lambda + \mu)\nabla(\nabla \cdot \mathbf{u}) + \mu\nabla^2 \mathbf{u} + \left(\frac{\lambda' + \mu'}{\omega}\right)\nabla\left(\nabla \cdot \frac{\partial \mathbf{u}}{\partial t}\right) + \left(\frac{\mu'}{\omega}\right)\nabla^2 \frac{\partial \mathbf{u}}{\partial t} = \rho\left(\frac{\partial^2 \mathbf{u}}{\partial t^2}\right) \quad (3.8)$$

(3.8) can be solved through a Helmholtz [137] decomposition by splitting the displacement field, \mathbf{u} , into a rotational component, $\nabla \times \boldsymbol{\psi}$, and an irrotational component, $\nabla\phi$, where $\boldsymbol{\psi}$ is an equivoluminal vector potential and ϕ is a compressional scalar potential. This results in equation (3.9).

$$\nabla\left[(\lambda + 2\mu)\nabla^2 \phi - \rho\left(\frac{\partial^2 \phi}{\partial t^2}\right)\right] + \nabla \times \left[\mu\nabla^2 \boldsymbol{\psi} - \rho\left(\frac{\partial^2 \boldsymbol{\psi}}{\partial t^2}\right)\right] = 0 \quad (3.9)$$

If (3.9) is satisfied, the two equations, (3.10) and (3.11), can be obtained, where c_L and c_T are the phase velocities of the longitudinal and shear waves respectively.

$$c_L \nabla^2 \phi = \frac{\partial^2 \phi}{\partial t^2} \quad (3.10)$$

$$c_t \nabla^2 \psi = \frac{\partial^2 \psi}{\partial t^2} \quad (3.11)$$

If the material is purely elastic, (3.10) and (3.11) becomes:

$$c_L = \left(\frac{\lambda + 2\mu}{\rho} \right)^{\frac{1}{2}} \quad (3.12)$$

$$c_T = \left(\frac{\mu}{\rho} \right)^{\frac{1}{2}} \quad (3.13)$$

If the material is purely elastic and the constants c_L and c_T are real values they will equal the longitudinal and shear bulk wave velocities respectively. If the material contains damping and is viscoelastic, then the speeds are complex.

3.2.2. Guided Wave Modes and Dispersion

There are different types of guided waves with different oscillation patterns. Lamb waves are guided waves that have particle displacements perpendicular to the direction of propagation that are also within the same plane as the direction of propagation. Lamb waves can be subdivided further into asymmetric (flexural) or symmetric (extensional) modes. Shear Horizontal waves are guided waves which oscillate perpendicular to the direction of propagation and in the plane perpendicular to propagation [138], [139]. Each guided wave type has different mode orders, where at different frequencies and plate thicknesses, different mode orders can occur, mode orders are commonly referred to as “modes” [140].

Guided waves are a packet of waves of different frequencies surrounding a centre frequency propagating as one, instead of a singular wave at a given frequency [41], [139]. The speeds of each individual frequency in a wave packet, the phase velocity, are typically

different from the speed of the centre frequency that the whole wave packet travels at initially at generation, this is called the group velocity. A mode is dispersive when the group velocity of the wave packet is different from the individual phase velocities of the different frequencies in the wave packet, as a wave propagates away from the point of generation, the wave packet begins to separate as the individual frequencies travel at their own speeds. This phenomena is called Dispersion [138], apart from the fundamental shear horizontal mode (SH0) where the group velocity is the same as the phase velocity, all guided waves mode are dispersive at varying intensities.

The theoretical occurrence of a mode in a plate of a given thickness can be calculated for a number of individual frequencies and then plotted as a curve to create a dispersion curve plot, [138], [139], where the occurrence of a mode at a given frequency-thickness product and wavenumber can be easily seen. Programmes such as Dispersion Calculator (German Aerospace Centre, DE) can be used to easily calculate all the theoretical occurrences of a guided waves for a given set of plate parameters, Fig. 21.

The frequency-thickness product is a key parameter in guided wave analysis, as it normalizes frequency values to account for plate thickness, making it easier to generalize dispersion behaviour across different materials and structures. Since guided wave modes depend on both the material properties and the geometric constraints imposed by plate thickness, the occurrence of certain wave modes is strongly linked to the frequency-thickness product. Lower-order modes, such as the fundamental symmetric (S0) and anti-symmetric (A0) Lamb wave modes, and the fundamental shear horizontal mode (SH0),

are generally present at all thicknesses, whereas higher-order modes emerge only when the frequency-thickness product reaches specific threshold values.

In dispersion curve plots, the phase velocity of each mode varies with frequency, and the shape of these curves provides insight into the dispersive nature of the waves at a given frequency. The slope of the dispersion curve, defined as the derivative of phase velocity with respect to frequency ($\partial v_p / \partial f$), shows how strongly dispersive a mode is. When the slope of the curve is nearly flat, the mode has little dispersion, meaning that different frequency components of a wave packet travel at similar speeds, and thus the wave packet maintains its shape over long propagation distances. When the slope of the dispersion curve is steep, the mode is highly dispersive, causing significant spreading of the wave packet as different frequency components travel at varying speeds. This phenomenon results in reduced signal clarity and complicates interpretation in ultrasonic testing applications.

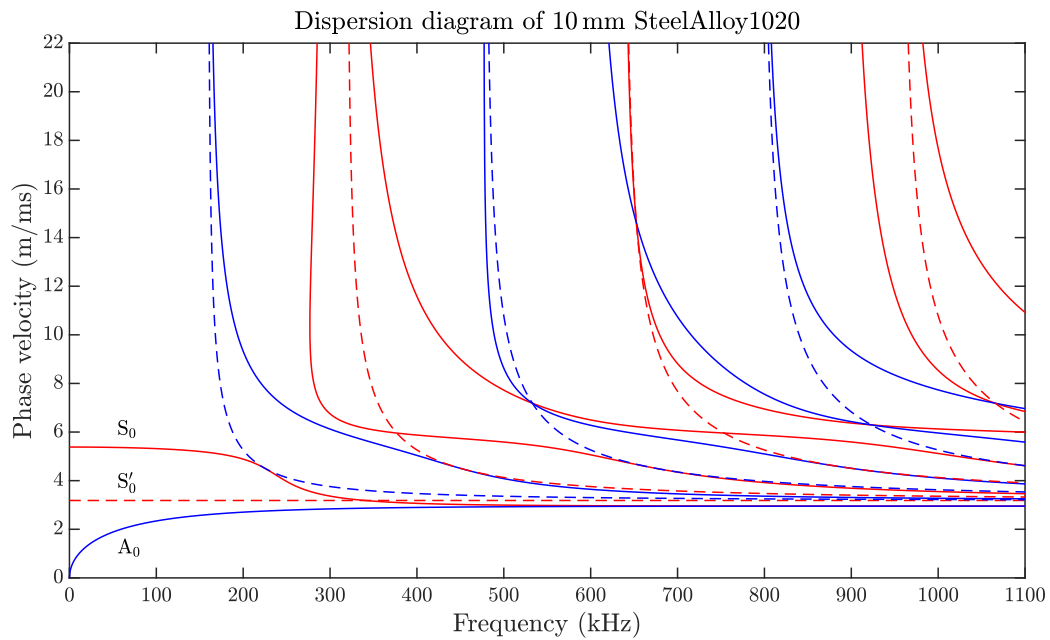


Fig. 21 Occurrences of Lamb waves are shown by solid lines, occurrences of Shear Horizontal waves are shown by the dashed lines. The blue and red indicates asymmetric and symmetric for Lamb waves and for Shear Horizontal waves. This plot was generated using Dispersion Calculator programme (German Aerospace Centre, DE).

For non-dispersive modes, such as the fundamental shear horizontal (SH0) mode, the phase velocity remains constant regardless of frequency, meaning that the group velocity is equal to the phase velocity. This makes the SH0 mode highly desirable for long-range inspections, as the wave maintains coherence over long distances without significant distortion. In contrast, higher-order wave modes typically exhibit strong dispersion, especially in thin plates, making their use more challenging in practical applications due to signal degradation.

When dispersion curves overlap or occur at the same frequency, multimodal generation can occur, meaning multiple guided wave modes are excited simultaneously. The extent to which this affects signal analysis depends on the phase velocity differences between

the modes at the shared frequency. If two modes exist at the same frequency but have significantly different phase velocities, multimodal generation is less problematic, in terms of signal analysis, because the wave packets will quickly separate in space as they propagate at different speeds. This natural separation reduces interference and simplifies signal interpretation. When multiple modes exist at the same frequency and have similar phase velocities, multimodal generation becomes a significant challenge for signal analysis. In this case, the wave modes travel at nearly the same speed, making it difficult to distinguish them in the received signal. Additionally, as the wave modes propagate at similar speeds they begin to interact, and can undergo mode conversion. Mode conversion can cause energy from one mode to be transferred into another due to reflections, scattering, or changes in boundary conditions. Mode conversion is particularly prevalent when guided waves encounter structural discontinuities, such as thickness variations, defects, or interfaces between different materials. This phenomenon can complicate defect detection and characterization, as converted modes introduce additional wave components that may obscure or mimic defect signals.

The dispersion curve also reveals cutoff frequencies, below which specific modes cannot exist. These cutoff frequencies are dependent on the plate thickness and material properties, dictating which modes can propagate for a given structure. In practical applications, dispersion curves can be used to select appropriate wave modes and frequencies to optimize signal propagation, minimize interference from unwanted modes, and enhance defect detection in structural health monitoring.

Experimentally the occurrence of a mode can be validated by carrying out a two dimensional Fast-Fourier Transform (2DFFT) [141] by generating a wave and measuring the wave over a number of distance steps. An example plot of SH1 is shown in Fig. 22. For example by measuring 64 steps at 1 mm iterations, at a position that is suitable to prevent electrical saturation, the received signals can then be processed and plotted as a heatmap of a wavenumber frequency-thickness plot with the theoretical occurrences overlaid, if the correct modes have been generated the wavenumbers/frequencies with high amplitude occurrences will align with the theoretical dispersion curves.

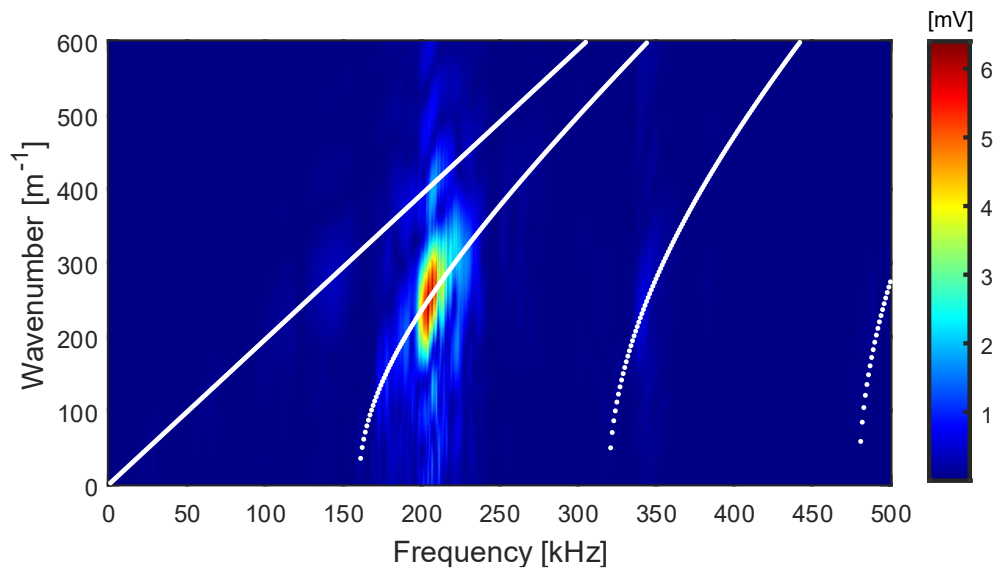


Fig. 22 An example of a 2DFFT plot to confirm that SH1 was generated in an experimental setup. SH1 was generated in 10mm steel and measured experimentally, the data was processed and plotted by wavenumber and frequency occurrences, with theoretical dispersion curves for the same sample overlaid.

3.2.2.1. Lamb Wave Propagation

Using the approach defined by Rose [138] for an infinite isotropic solid, the equations which govern Lamb wave propagation and their dispersive properties can be derived from

(3.10) and (3.11). Lamb waves comprise of both shear and longitudinal motion creating elliptical particle motion, Lamb wave propagation, symmetric and anti-symmetric, can be seen in Fig. 23.

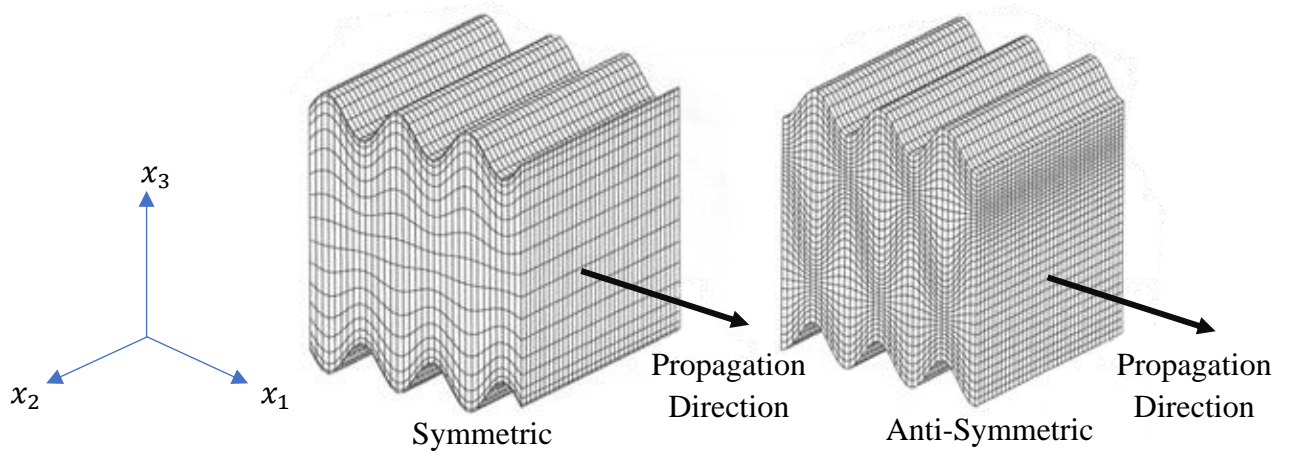


Fig. 23 Symmetric/extensional (left) and anti-symmetric/flexural Lamb wave propagation, adapted from [142].

For purely isotropic media, (3.14) and (3.15) can be written:

$$\nabla^2 \phi - \frac{1}{c_L^2} \frac{d^2 \phi}{dt^2} = 0 \quad (3.14)$$

$$\nabla^2 \psi - \frac{1}{c_T^2} \frac{d^2 \psi}{dt^2} = 0 \quad (3.15)$$

Due to the elliptical motion of Lamb waves, the equations can be simplified by disregarding the motion in the direction of x_2 axis, this results in:

$$\frac{\partial^2 \phi}{\partial x_1^2} + \frac{\partial^2 \phi}{\partial x_3^2} = \frac{1}{c_L^2} \frac{d^2 \phi}{dt^2} \quad (3.16)$$

$$\frac{\partial^2 \psi}{\partial x_1^2} + \frac{\partial^2 \psi}{\partial x_3^2} = \frac{1}{c_T^2} \frac{d^2 \psi}{dt^2} \quad (3.17)$$

The elliptical motion allows for plane strain to be assumed, where deformation only occurs in the x_1 - x_3 plane. General plane wave solutions can be defined for travelling waves in the x_1 direction and standing waves in the x_3 direction, where k is the wavenumber.

$$\phi = \Phi(x_3)e^{i(kx_1-\omega t)} \quad (3.18)$$

$$\psi = \Psi(x_3)e^{i(kx_1-\omega t)} \quad (3.19)$$

(3.20) and (3.21) can be assumed the expressions in the thickness direction, where A_1, A_2, B_1 and B_2 are arbitrary amplitude constants, g and p are wavenumbers in the x_3 direction.

$$\Phi(x_3) = A_1 \sin(px_3) + A_2 \cos(px_3) \quad (3.20)$$

$$\Psi(x_3) = B_1 \sin(gx_3) + B_2 \cos(gx_3) \quad (3.21)$$

Displacement terms can be established by splitting functions into odd and even functions which results in symmetric and antisymmetric solutions. Symmetric motion about the mid plane of a plate can be described by cosine terms in the u_1 displacement and sine terms in the u_3 . Antisymmetric motion about the mid plane of a plate can be described by sine terms in u_1 and cosine terms in the u_3 .

Symmetric Waves

$$u_1 = ikA_2 \cos(px_3) + qB_1 \cos(gx_3) \quad (3.22)$$

$$u_3 = -pA_2 \sin(px_3) - ikB_1 \sin(gx_3) \quad (3.23)$$

Antisymmetric Waves

$$u_1 = ikA_1 \sin(px_3) - qB_2 \sin(gx_3) \quad (3.24)$$

$$u_3 = pA_1 \cos(px_3) - ikB_2 \cos(gx_3) \quad (3.25)$$

The boundary conditions for Lamb waves state that the normal and shear stresses must be equal to zero at the top and bottom plate surfaces, represented by $\pm h$, creating the condition $x_3 = \pm h$. Applying this condition gives a pair of equations with two unknown constants for both symmetric modes, A_2 & B_1 , and antisymmetric modes, A_1 & B_2 . The systems of equations for each mode can be solved via matrix format and taking the determinant. For symmetric waves this can be simplified to give (3.26) and for antisymmetric waves (3.27). The time dependent of the plane wave solution is omitted for simplicity.

$$\frac{\tan(gh)}{\tan(ph)} = -\frac{4k^2pg}{(g^2 - k^2)^2} \quad (3.26)$$

$$\frac{\tan(gh)}{\tan(ph)} = -\frac{(g^2 - k^2)^2}{4k^2pg} \quad (3.27)$$

If the wavenumber is real, imaginary or complex, various real-world applications can be inferred. If the wavenumber value is complex, the time harmonic element of the dispersion relationship, $e^{i(kx_1 - \omega t)}$, which was omitted from the above derivation is shown by (3.28). From this, three distinct forms of k_{im} can be seen which describe the different types of Lamb waves. In the case of $k_{im} > 0$, an evanescent Lamb wave that exponentially decays with distance is described. In the case of $k_{im} < 0$ a Lamb wave that grows exponentially with distance is described. Lamb waves described by $k_{im} = 0$ are those which are utilised by NDE techniques.

$$e^{i(kx_1 - \omega t)} = e^{i(k_r x_1 - \omega t)} e^{-k_{im} x_1} \quad (3.28)$$

3.2.2.2. Shear Horizontal Guided Wave Propagation

Similarly to Lamb waves, the equations which describe bulk and shear motion in an infinite isotropic solid can be used to derive the equations which govern the propagation of Shear Horizontal guided waves in finite media. For SH waves there is no displacement in the x_1 and x_3 directions and there is no compressional scalar potential as their particle motion is entirely in the transverse direction. Fig. 24 shows the propagation of an SH mode. This means that Equation (3.11) can be rewritten as (3.29) for motion in the x_2 direction.

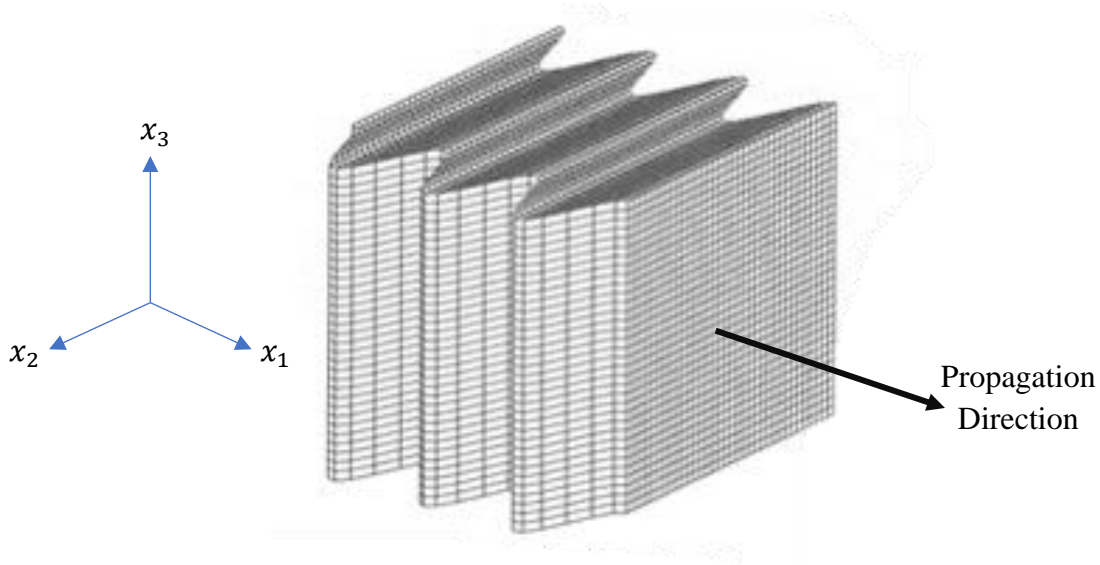


Fig. 24 Shear Horizontal guided wave mode propagation, adapted from [142].

$$\frac{\partial^2 \psi}{\partial t^2} = c_T^2 \left(\frac{\partial^2 \psi}{\partial x_3^2} \right) \quad (3.29)$$

A general plane solution can be taken, where k_{x_1} is the wavenumber in the propagation direction:

$$\psi = \Psi(x_3)e^{i(k_{x_1}x_1 - \omega t)} \quad (3.30)$$

The component in the thickness direction, x_3 , can be written as:

$$\Psi(x_3) = A \sin(k_{x_3}x_3) + B \cos(k_{x_3}x_3) \quad (3.31)$$

A and B are arbitrary constants and k_{x_3} is the through thickness wavenumber. For SH waves, the boundary conditions require that the shear stress σ_{32} vanishes at the free surfaces:

$$\frac{\partial \psi}{\partial x_3} = 0 \text{ at } x_3 = 0, x_3 = T$$

Applying these boundary conditions and solving for k_{x_3} results in (3.32).

$$\cos(k_{x_3}T/2) \sin(k_{x_3}T/2) = 0 \quad (3.32)$$

(3.32) can be solved when k_{x_3} is equal to:

$$k_{x_3} = \frac{\pi n}{T} \quad (n = 0, 1, 2, 3, \dots) \quad (3.33)$$

The wavenumber can be related to the shear bulk wavenumber, shown in (3.34).

$$k_{x_3}^2 = k_T^2 + k_{x_1}^2 \quad (3.34)$$

The shear wave wavenumber can be described as (ω/c_T) which results in:

$$k_{x_1}^2 = \left(\frac{\pi n}{T}\right)^2 - \left(\frac{\omega}{c_T}\right)^2 \quad (3.35)$$

As $k_{x_1} = \omega/c_p$, the dependent phase velocity of shear horizontal waves can be found for a given frequency, f , and plate thickness, T , this is shown by (3.36).

$$c_p(fT) = \pm 2c_T \left(\frac{fT}{\sqrt{4(fT_0)^2 - n^2c_T^2}} \right) \quad (3.36)$$

(3.36) can be derived further to find the group velocity for a given frequency and plate thickness:

$$c_g = c_T \sqrt{1 - \frac{\left(\frac{n}{2}\right)^2}{(fT_0c_T)^2}} \quad (3.37)$$

3.2.3. Guided Wave Energy Density Distribution

Guided wave modes have different wave shapes, this applies to waves of the same mode (shear horizontal) but of different order (SH0/S_H1), an example can be shown in Fig. 25, where the particle displacement in oscillation follows a different pattern for each mode order but oscillation occurs in the same plane for a given mode type [138].

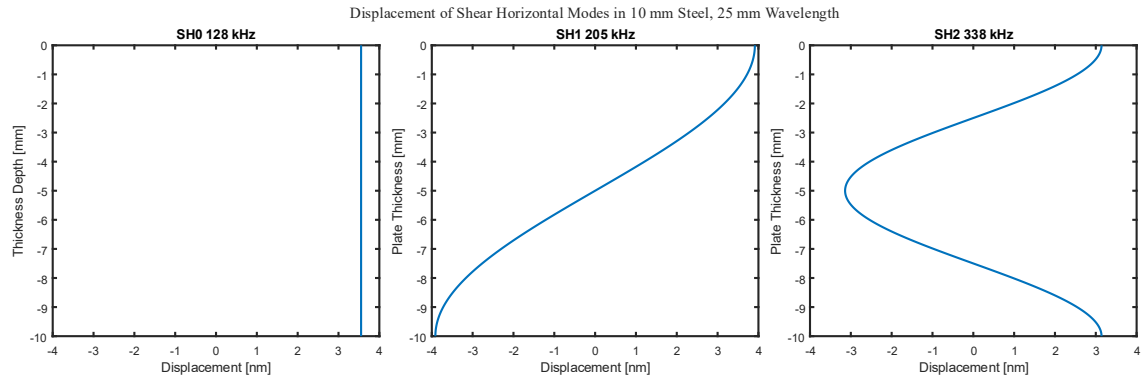


Fig. 25 The displacement patterns of three modes of the same wave type but different orders, in 10mm steel, SH0, SH1 and SH2. Generated using the programme Dispersion Calculator. Plate thickness axis is displayed in Fig. 26.

As well orders of the same mode have varying energy density distributions, the energy density distribution of a given mode can be used to identify the percentage of a modes energy at a given point in a plates thickness. The energy density distribution, E_{total} , can

be calculated for a given point in the plates thickness using (3.38). These equations operate in a domain, $x_i = (x_1, x_2, x_3)$, see Fig. 26, where the plate thickness lies on the x_2 axis.

$$E_{total} = E_{strain} + E_{kinetic} \quad (3.38)$$

$$E_{strain} = \frac{1}{2} \int_S \sigma_{ij} \varepsilon_{ij} dS \quad i, j = 1, 2, 3 \quad (3.39)$$

$$E_{kinetic} = \frac{1}{2} \rho \int_S v_i^2 dS \quad (3.40)$$

Where σ_{ij} is the stress tensor, ε_{ij} is the strain tensor, ρ is the plate density, v_i is the particle velocity. Integration of the two energy densities is performed over the cross section of the plate, S [40].

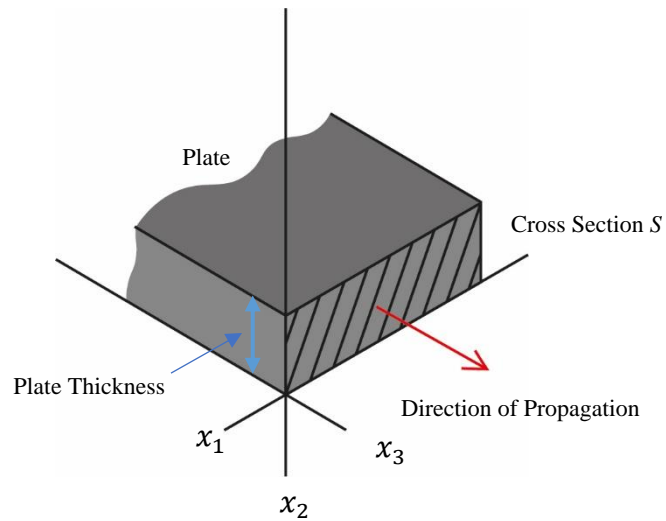


Fig. 26 The coordinate system that is used to calculate the energy density through a plates thickness is shown here, where the direction of propagation can be seen, the plane on which the thickness lies and the cross section S .

3.3. Electromagnetic Acoustic Transducers

3.3.1. Practicality of EMAT Wave Generation

Lorentz forces are the main driving mechanism in the majority of EMAT setups, as Lorentz forces can be generated in any metallic subject such as aluminium [46], [143]. In ferromagnetic subjects two other mechanisms arise, magnetization and magnetostriction, the material of the subject and the EMAT setup influences the dominance of each mechanism in a given case.

There are multiple advantages to using an EMAT to produce ultrasonic waves, the two key advantages are the non-contact transduction and ability to easily generate certain guided wave modes. As electromagnetic induction is used to excite waves within a material, couplant and subject contact is not needed, unlike piezoelectric wave generation methods. However transduction efficiency degrades exponentially as the lift off from the subject increases slightly, in practice this separation is only a few millimetres before transduction is too weak to produce a wave suitable for inspection purposes [46], [144]. The non-contact gap however is enough that it makes EMATs suitable for inspection where movement is involved, where either the sample is moving or the transducer is moving and the other is stationary. EMATs have been used and developed for use on mobile robots where the subject is stationary and the transducer is moving [50], [127].

There are applications for EMATs in a factory setting to inspect ferromagnetic subjects on a production line. As the parts are moved under an EMAT and contact is not required [145], [146], simple rapid inspection can be carried out on parts during production in a

continuous fashion. Furthermore EMATs can be built to be robust and withstand high temperatures which makes them extremely useful in situations where the subject under investigation is at a high temperature [46].

Compared to common piezoelectric generation methods, EMATs are simpler in terms of setup for generating waves. As EMATs only need to be within close proximity to a conductive subject to generate a wave and typically don't require surface prep. Methods such as phased array require complete contact with a subjects surface, a coupling medium, and usually require surface prep and cleaning prior to inspection.

There are disadvantages to using EMATs, the first being that EMATs can only be used to generate waves within subjects that are good electrical conductors which significantly reduces the usage applications for EMATS. Signal-to-noise ratios can be poor if the correct transduction design is not used, even in cases where the setup is optimized, the SNR will typically be less than other methods of ultrasonic detection [41], [46], [50]. Different materials have different electromagnetic properties and as a result the strength and quality of signals from the same EMAT can vary depending . Furthermore in mobile robotic applications, due to EMATs typically requiring high strength background magnetic fields, the magnet arrays that make up EMATs can typically impede mobile robotic movement when operating on a ferromagnetic subject [50].

3.3.2. Styles of EMATs

EMATs can be used to generate a variety of bulk waves and guided waves. There are a wide variety of coil styles and magnet arrays that could be combined to create an EMAT, in this section the most common styles are covered.

A spiral/pancake coil EMAT can be used to generate radially polarized shear bulk waves, the coil is beneath single magnet where the poles are directed normal to the subject surface. An elongated spiral/racetrack EMAT can be used to generate linearly polarized shear waves. Linearly polarized longitudinal waves can be generated using a spiral coil configuration which loops around a horseshoe magnet [46], [147].

Meander coil EMATs are a design that can be used to generate Lamb and Rayleigh Waves, the coil follows a back and forth zig-zag pattern that resembles the free space between the combs of an interdigitated transducer, in a conventional meander EMAT a single magnet is placed above the coil with the poles directed normal to the subject surface [148]. The horizontal spacing between coil lengths determines the wavelength of the waves generated.

Periodic Permanent Magnet EMATs, Fig. 27, are the easiest way to practically generate Shear Horizontal guided waves. Typical PPM EMATs utilize a racetrack coil underneath a magnet array with two rows, where a given magnet faces a magnet of opposite polarization in all directions, when the coil is pulsed a typical PPM EMAT transmitter will produce waves in both directions, bi-directionally [46]. Bi-directional generation is where the transducer will produce waves, both forwards and backwards, in the same axis that the coil is when it is underneath the magnet array, this is highlighted in Fig. 27. The

number of magnets in row determines the bandwidth of generation, an increased number of magnets in a row creates narrowband generation and a decreased number of magnets in a row creates wideband generation. The wavelength of the generated modes is determined by the centre-to-centre spacing between two magnets of the same polarization in a given row. A variety of PPM EMAT designs exist [149], [150], [151], [152].

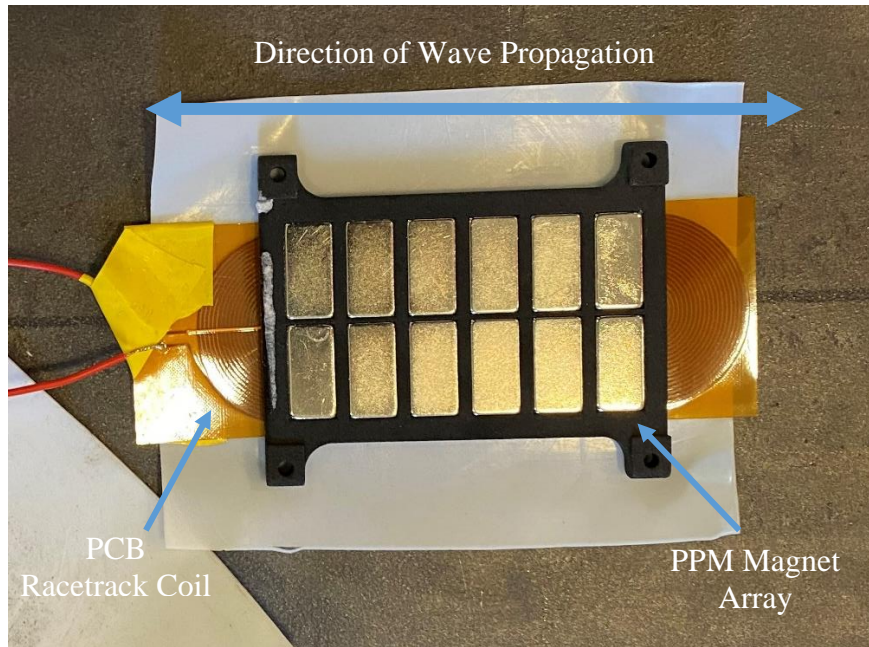


Fig. 27 An example of PPM EMAT with the housing removed where the magnet array and racetrack coil can be seen, this EMAT is designed to generate SH0 and SH1 with 25mm wavelengths.

Omnidirectional EMATs are EMATs which can generate waves in a full 360 degrees around the centre of the transducers in a single transmission. A circular pancake coil combined with a circular magnet can be used to generate waves in all directions. Guo et al. [153] presented an annular magnet PPM array omnidirectional EMAT design which enhances the strength of A0 signals generated by the transducer. Seung et al. [154]

presented a Lorentz force based omnidirectional EMAT for generating shear horizontal wave modes.

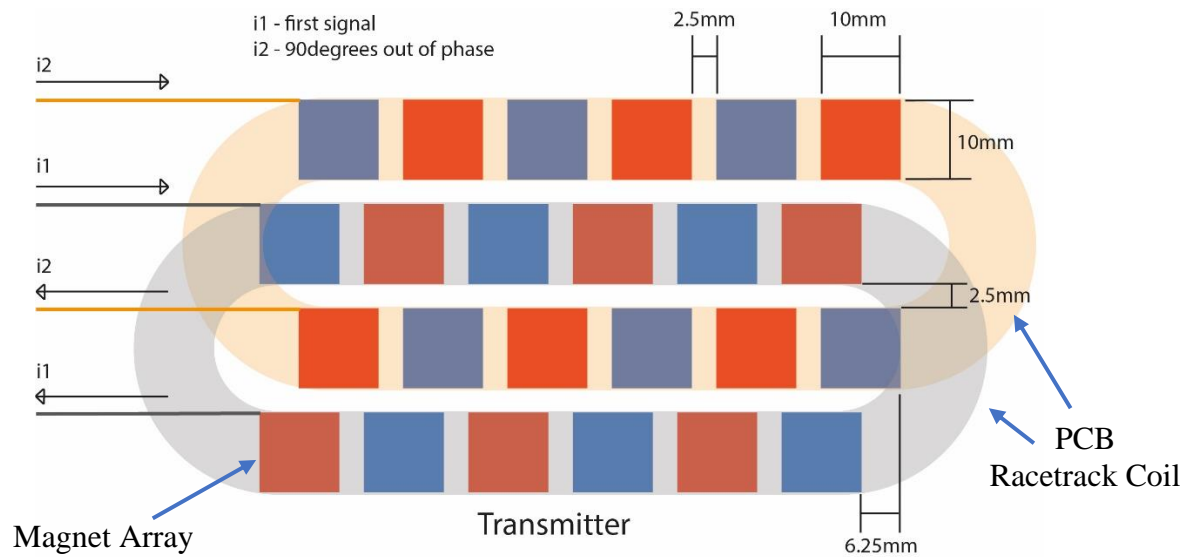


Fig. 28 Diagram of a unidirectional EMAT transmitter. Two coils, blue and orange, with wide centre gap spacing, are overlapped and offset by 90degrees of phase. The magnet array, red and blue squares, is also staggered to match the coil offset.

Unidirectional EMATs are EMATs which are typically modified versions of a traditional EMAT design where typically two transducers are overlapped and combined in order to create constructive and destructive interference at opposing ends of the EMAT, Fig. 28 shows a diagram of a unidirectional SH EMAT. An early example was presented in 1978 by Toda and Shinoda [155] where an interdigitated style unidirectional Lamb wave transducer was created, the two combs were pulsed separately with 90° phase shift between the two signals. Shujuan Wang et al. [156] developed a unidirectional focusing meander coil EMAT for generation of Rayleigh waves, this system overlapped two meander coils which were pulsed 90° out of phase underneath a single magnet. Rieger et al. [157] developed a unique coil only Lamb wave unidirectional EMAT, where two

racetrack coils are placed side by side, spaced $\frac{1}{4}$ wavelength apart, and pulsed independently. Kubrusly et al. [21] demonstrates a side shifted magnet array which equates to two PPM EMATs merged and offset, the two coils in this EMAT are pulsed 90° apart, resulting in single sided generation with small backward side-lobes. [22] demonstrates a dual-linear coil array rather than the traditional racetrack design, whereby multiple magnet arrays are individually wrapped in wire from one of two coils, which are pulsed with 90° separation creating single sided generation. The resultant wavelength is however doubled making it more suited to low frequencies. [158] revised the side shifted design of [21] to improve the radial pattern by altering the racetrack coil shape to loop under increased magnet arrays. Thon et al. [152] presents work on optimising the magnet array of a PPM EMAT for generating plate SH guided plates waves in curved surfaces such as a pipe. Different magnet array configurations were investigated where the array that produced the best signals was constructed using magnets that were altered to conform to the curvature of the pipe, reducing the distance between the background magnetic field and the sample. Coil optimisation was not investigated in this work. S. L. Huang et al. [159] investigated a unique point focussed unidirectional EMAT which uses a semi-circle shaped magnet array with side shifted magnets to achieve unidirectional focussing.

3.4. EMAT Mechanisms

3.4.1. The Lorentz Force

Electromagnetic acoustic transducers are transducers that can generate bulk and guided ultrasonic waves within metallic materials [46]. EMATs in their simplest form are a coil that is pulsed with an Alternating Current (AC), the alternating current induces an eddy current density, \mathbf{J}_e , in the material when placed close to the surface. A magnet or magnet array creates a static background bias magnetic flux density, \mathbf{B} , also known as the magnetic field vector, is placed behind the coil. The eddy currents interact with and are enhanced by the magnetic flux density which produces a net body force in the subject, this force is called the Lorentz force, Fig. 29, and is given by Equation 3.41. The Lorentz force is body force as it is a distributed force that acts across a volume of material instead of being concentrated at a single point, generating mechanical motion. As the AC current is changing direction, this causes the Lorentz force to change direction which generates an ultrasonic wave [46], [143], [160]. The Lorentz force is the dominant mechanism for the generation of waves in the majority of steels [46], [147], [143], [160].

**Directions of
Lorentz Force**

$$\mathbf{f} = \mathbf{J}_e \times \mathbf{B} \quad (3.41)$$

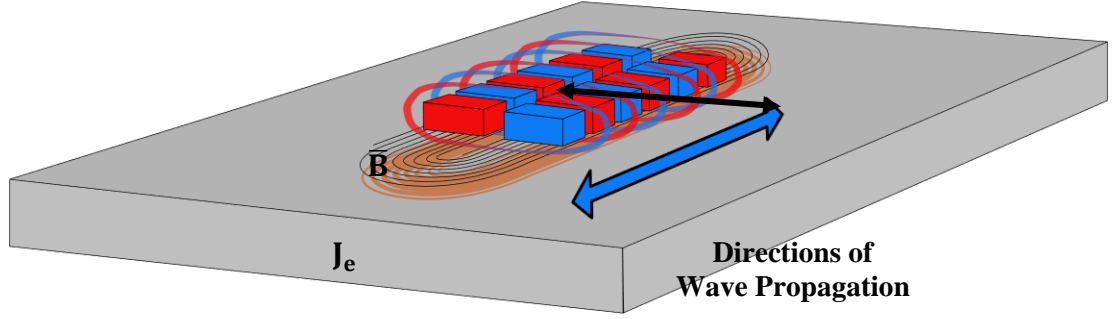


Fig. 29 Diagrammatic representation of the Lorentz force mechanism in a racetrack coil PCB bidirectional EMAT, shown are the induced eddy currents in orange, magnetic flux, \mathbf{B} , density surrounding the magnets perpendicular to the coil and the direction of propagation of the generated guided waves depicted by the blue arrow.

Microscopically, the electric field, \mathbf{E} , induces a current by applying a Coulomb force, $e\mathbf{E}$, where e is the charge on the particle, on the subjects electrons, accelerating them to a mean velocity given by $-e\mathbf{E}\tau/m_e$, where m_e is the mass of an electron, τ is the time between electron-ion collisions. If a bias magnetic field vector is present the electrons are subject to the Lorentz force, the eddy current density can be written as $e\mathbf{v}_e$, where \mathbf{v}_e is the electrons mean velocity. Due to harmonic oscillations being considerably slower than the mean frequency of the of electron-ion collision, the inertial forces of the electrons can be neglected, thus (3.41) becomes (3.42), where n_e is the electron density.

$$\frac{n_e(m_e\mathbf{v}_e)}{\tau} = -n_e e(\mathbf{E} + \mathbf{v}_e \times \mathbf{B}) \quad (3.42)$$

The electrons that are driven by the Lorentz and Coulomb force collide with the ions of the subject and exchange their momentum, the force experienced by a materials ions is described by (3.43). Where N_i is the ion density, Z_i is the ion charge and \mathbf{v}_i is the ion velocity.

$$\mathbf{f} = N_i Z_i (\mathbf{E} + \mathbf{v}_i \times \mathbf{B}) + \frac{n_e (m_e \mathbf{v}_e)}{\tau} \quad (3.43)$$

(3.42) and (3.43) can be utilised to show that the collision force from the electrons is the dominant force acting on the lattice ions rather than the Lorentz force they experience from the magnetic field, as the electrons are transferring the Lorentz energy to the ions via collision. The dominant force acting on the ions is shown in (3.44), where $\mathbf{J}_e = -n_e e \mathbf{v}_e$ and is the eddy current induced in the subject.

$$\mathbf{f} = -n_e e \mathbf{v}_e \times \mathbf{B} = \mathbf{J}_e \times \mathbf{B} \quad (3.44)$$

For EMATs, the magnetic flux density, \mathbf{B} , is typically the dominating component of (3.44), and the dominating factor of \mathbf{B} , is the static background magnetic field vector, $\bar{\mathbf{B}}$. However, the presence of an alternating eddy current density means that the total force applied to the ions oscillates, leading to periodic displacements of the lattice structure.

These oscillating forces in the material act as a localised periodic excitation source, generating an elastic wave that propagates through the solid. The direction of wave propagation depends on the relative orientation of the applied magnetic field, the induced eddy currents, and the material's elastic properties.

- For Shear Horizontal (SH) Waves: If the eddy current distribution and Lorentz force primarily induce displacements parallel to the surface, a horizontally polarized shear wave (SH wave) is generated. This occurs when the bias magnetic field is perpendicular to the plane of the eddy currents, leading to a force that oscillates parallel to the material surface.

- For Rayleigh or Lamb Waves: If the Lorentz force generates oscillations both normal to and along the material surface, surface-guided waves such as Rayleigh waves or Lamb waves can be excited, propagating at the interface or within the plate.
- For Bulk Waves (Longitudinal or Shear Vertical Waves): Depending on the force distribution and transducer design, bulk longitudinal waves (if the force has a strong normal component) or shear vertical waves (if the force is directed out of the plane) can also be excited, propagating deeper into the material.

Thus, by carefully selecting the orientation of the magnetic field, the configuration of the eddy currents, and the material properties, EMATs can be designed to generate specific wave modes.

3.4.2. EMAT Physics

The mechanisms described in this section cover the typical operation of the EMATs used in this work where the Lorentz force is the dominating operating mechanism, magnetization is also covered. Magnetostriction is discussed in the next section separately as Lorentz and magnetization forces are body tractions applied to an elastic subject whereas magnetostriction is the elastic strain created in a subject by an external magnetic field.

Electromagnetism is the mechanism that EMATs utilize to operate, electromagnetism can be described by Maxwells fundamental equations which combine Faradays and Amperes

Law [46], [48], [143], [161]. The first Equation (3.45) states that the electric flux density, \mathbf{D} , leaving a closed surface is proportional to charge density within the surface, ρ .

$$\nabla \cdot \mathbf{D} = \rho \quad (3.45)$$

The second of Maxwells equations, (3.46), states that the net magnetic flux density through a closed surface is zero.

$$\nabla \cdot \mathbf{B} = 0 \quad (3.46)$$

The third equation (3.47) is that any time-varying electric field, will generate a time varying magnetic field, the same is true for the reverse where any time varying magnetic field generates a time-varying electric field.

$$\nabla \times \mathbf{E} = -\frac{\delta \mathbf{B}}{\delta t} \quad (3.47)$$

The fourth equation (3.48) states that a moving electric charge will induce a magnetic field, \mathbf{H} , in a closed loop around it. The curl of this magnetic field is proportional to the electric current density within the loop, \mathbf{J} , and the variation in the electric flux density. In this work the operation frequencies are below 100MHz so the term $\delta \mathbf{D}/\delta t$ is dropped [162].

$$\nabla \times \mathbf{H} = \mathbf{J} + \frac{\delta \mathbf{D}}{\delta t} \quad (3.48)$$

The constitutive relation between the magnetic flux density and the magnetic field is given by Equation (3.49). Where \mathbf{M} is the magnetization, which describes how a material reacts to an applied magnetic field and μ_0 is the permeability of free space.

$$\mathbf{B} = \mu_0(\mathbf{H} + \mathbf{M}) \quad (3.49)$$

Equation (3.50) is the microscopic version of Ohms law.

$$\mathbf{J} = \sigma \mathbf{E} \quad (3.50)$$

Using the fundamental equations above, the following equations (3.51), (3.52) & (3.53) can be derived to calculate the dynamic forces applied to a subject by an EMAT. Where \mathbf{f}_L is the Lorentz force and \mathbf{f}_M is the magnetization force.

$$\mathbf{f}_L = \mathbf{J}_e \times \mathbf{B} \quad (3.51)$$

$$\mathbf{f}_M = \nabla \mathbf{H} \cdot \mu_0 \mathbf{M} \quad (3.52)$$

$$\mathbf{f}_{\text{body}} = \mathbf{f}_L + \mathbf{f}_M \quad (3.53)$$

In (3.52), $\nabla \mathbf{H}$ is a 3×3 second order tensor whose (i,j) element in cartesian coordinate is $\delta H_j / \delta x_i$, the magnetization force components can be described by $f_k = \mu_0 M_i (\delta H_i / \delta x_k)$, where summation convention is assumed. The acoustic field for a continuous elastic isotropic subject, when the described body forces are applied, is described by (3.54), where ρ_s is the subjects mass volume density, \mathbf{S} is the displacement vector, μ_c and λ_c are Lamé constants.

$$\mathbf{f}_{\text{body}} = \mu_c \nabla \times \nabla \times \mathbf{S} - (\lambda_c + 2\mu_c) \nabla \nabla \cdot \mathbf{S} + \rho_s \frac{\partial^2 \mathbf{S}}{\partial t^2} \quad (3.54)$$

When the EMAT coil is pulsed with an AC current the dynamic current density induces a mirror eddy current in the samples skin-depth which opposes the original current, eddy currents can only be induced near the surface of the material close to the coil. The skin-depth, δ , can be calculated using (3.55), where f is the frequency of the sinusoidal AC current the coil is pulsed with, σ is the subject conductivity and μ_r is the relative permeability.

$$\delta = (\pi f \sigma \mu_0 \mu_r)^{-1/2} \quad (3.55)$$

The body forces applied to a subject by an EMAT through Lorentz forces are summarized by (3.56). The magnetic flux density applied to a subject by an EMAT is a combination of the dynamic magnetic vector field, $\tilde{\mathbf{B}}$, and the static magnetic vector field, $\bar{\mathbf{B}}$, created by the magnet or magnet array behind the coil. This means that the Lorentz force can be split into dynamic and static operations, shown by (3.57), where $\bar{\mathbf{f}}_L$ is the static force, $\tilde{\mathbf{f}}_L$ dynamic is the dynamic force, the frequency f can also be described as the angular frequency $\omega = 2\pi f$.

$$\mathbf{f}_L = \tilde{\mathbf{f}}_L + \bar{\mathbf{f}}_L = \mathbf{J}_e \times (\tilde{\mathbf{B}} + \bar{\mathbf{B}}) \quad (3.56)$$

$$\mathbf{f}_L = \begin{cases} \mathbf{J}_e, \tilde{\mathbf{B}} \propto \sin \omega t \\ \bar{\mathbf{B}} = \text{const.} \end{cases} \quad (3.57)$$

Magnetisation forces, (3.52), have been shown theoretically and experimentally [46], [163], [164] to have a similar amplitude be out of phase with the Lorentz forces resulting in cancelling of the magnetisation. This means that Magnetisation cannot be used to generate compressional waves and their contribution to shear wave generation is negligible.

The magnetization force is proportional to the gradient of the magnetic field and generally acts along the direction of magnetization variations within the material, which is typically parallel to the magnetization vector but can develop components in both the in-plane and out-of-plane directions. In contrast, the Lorentz force acts perpendicular to both the induced current density and the total magnetic field, $(\tilde{\mathbf{B}} + \bar{\mathbf{B}})$. The magnetization force develops components along the field gradient, meaning it typically has an axial (longitudinal) or out-of-plane component relative to the Lorentz force. In PPM EMATs,

where alternating magnetization patterns are present, this results in a force that is not only phase-shifted relative to the Lorentz force but also oriented in a direction that does not effectively contribute to the generation of shear horizontal (SH) waves, further reducing its influence.

For materials with significant magnetic susceptibility, the magnetization force often develops a component opposing the Lorentz force. This opposition arises due to the internal alignment of atomic dipoles with the applied field, creating a restoring effect that counteracts the Lorentz-driven motion. Furthermore, the magnetization force is out of phase with the Lorentz force, meaning that if the Lorentz force varies sinusoidally with time (e.g., $\sin \omega t$ dependence), the magnetization force often follows a $\cos \omega t$ or $-\sin \omega t$ dependence, depending on the material's response. This phase shift leads to partial cancellation of the net force experienced by the material.

3.4.3. Magnetostriction Mechanism

EMATs exploit field induced magnetostriction, where the presence of a magnetic field causes elastic stresses in a ferromagnetic subject. The application of a magnetic field to a ferromagnetic structure results in a net strain in the direction of the field, microscopically the crystal domains of a subject that are closest to the alignment of the magnetic field expand and try to fully align themselves with the applied field. This results in a given domain applying force to their neighbouring domains through shifting caused by alignment. When a dynamic oscillating magnetic field is applied, dynamic oscillating stresses occur which creates vibrations due to the expansion and contraction of the

domains, this creates vibrations and as such this effect can be utilized to generate ultrasonic waves.

Ribichini et al. [165] have shown that in the cases of steel, which this work primarily focusses on, Lorentz forces is the main generation mechanisms for EMATs. Nickel has been shown to be a suitable coupling material when it is bonded to a steel subject, however practically, especially in the case of mobile robotics, bonding nickel plating to another subject increases the difficulty of inspection and is better suited to a long term structural health monitoring scenario where repeated measurements are taken from the same point [166].

3.4.4. Detection Process

Ultrasonic waves propagate in a subject through the vibrations of the crystal lattice of ions [138], which dominate wave transmission due to their significantly greater mass compared to the free electrons oscillated by the Coulomb force [167]. There are no net electromagnetic fields created by a propagating wave, although if the moving charged particles encounter an external applied magnetic field, such as the static background field created by an EMAT magnet array, the charged particles will create an electric field when their motion is affected by the external field. This is shown by (3.58) where \mathbf{E}_D is the dynamic electric field, $\bar{\mathbf{B}}$ is the background static magnetic field created by the receiver EMAT magnet array and \mathbf{u} is the particle displacement [46], [48].

$$\mathbf{E}_D \propto \frac{\partial \mathbf{u}}{\partial t} \times \bar{\mathbf{B}} \quad (3.58)$$

The field created by the charged particles produces a current loop in the subject, the dynamic magnetic field is registered by the receiver EMAT coil. A voltage output signal is created which is proportional to the vibration of subject.

3.5. Chapter Conclusion

This chapter presented the physics of ultrasonic guided wave propagation and their different characteristics. From this it was found that the energy density distribution of a wave mode, and that the wave modes likeliness to mode convert are the determining factors of their reflectivity from a welded section. This was further explored in Chapter 4 through simulated and experimental investigation.

Relevant EMAT design work were reviewed however it was clear that there was a gap in literature for a method to optimise EMATs for mobile robotic applications. The style of EMAT to be optimised for mobile robotics was a PPM EMAT this was covered in Chapter 5. A PPM style EMAT was optimised as a result of the conclusion of investigation in Chapter 4.

Chapter 4

4. Characterisation of EMAT Guided Wave Reflectivity on Welded Structures for use in Ranging

4.1. Introduction

Utilising guided waves reflecting from welded sections has been proposed as a potential ranging system for mobile robotic positioning, this chapter covers the investigation into this. The criteria for a wave modes ranging suitability and the process for measuring wave mode reflectivity is presented, simulation and experimental setup of this process and the results are shown. SH1 was found to be the wave mode best suited to ranging due to its high reflectivity from welded sections in simulation and experiment. The positional error of SH1 due to dispersion was evaluated, it was found to be acceptable at 2.65%.

4.2. Existing Research Investigating Guided Wave Weld Reflectivity

There is existing research investigating guided wave propagation however the research is not in-depth enough to determine which guided wave mode reflects best from a welded section. As well existing research does not describe why one wave mode would reflect more than another. Both were investigated in this work, existing research is presented in the following paragraph.

Yang et. al [168] has looked at the propagation of SH0, 128kHz, waves at a Butt Weld, T-Joint, and Lap Joint. SH0 was shown to reflect off each weld type in experimental setup and 2D simulation, however the reflection coefficients were found through non-welded area comparisons. Khalili and Cawley [55] used simulation to carry out an investigation into the response of SH0, SH1, S0 and A1 modes when encountering features in 10mm steel. It was found that S0, SH0 and SH1 were reflected from a T-joint, with SH1 having the highest reflection coefficient. The T-Joint was simulated by adding additional steel to the surface of the plate without simulating any weld head or weld pass geometry. In this work 2DFFT was used to identify the modes generated and received. Sargent [169] used an omnidirectional multi-element transducer to detect corrosion within butt welds and did not explicitly measure wave mode reflectivity. It is stated that at positions normal to the weld the reflectivity of the S1 wave mode was too great to identify the artificial corrosion. Both [170] and [171], investigated Rayleigh wave interaction with welds and rib type

features (geometry comparable to butt welds). Both works showed instances of Rayleigh wave reflections at very short distances from the welds with low reflectivity.

4.3. Guided Wave Weld Reflectivity Investigation

To assess whether a guided wave mode is capable for use in ranging using welds, its reflectivity from welds must first be investigated, if the mode does not reflect well from welds it is not suitable for ranging. The following wave modes were investigated: SH0 (128 kHz), SH1 (205 kHz), S0 (106 kHz), S1 (375 kHz) and A0 (91 kHz). The modes listed are marked on a dispersion curve for 10mm Mild Steel, Fig. 30.

SH frequencies were chosen based on the EMAT's available for experimental generation. Lamb wave frequencies were chosen where dispersion would be reduced and single mode generation was encouraged. Looking at the dispersion curve plot below this would be frequencies where the gradient is near horizontal and/or is not close in phase velocity with another mode at the same frequency of occurrence.

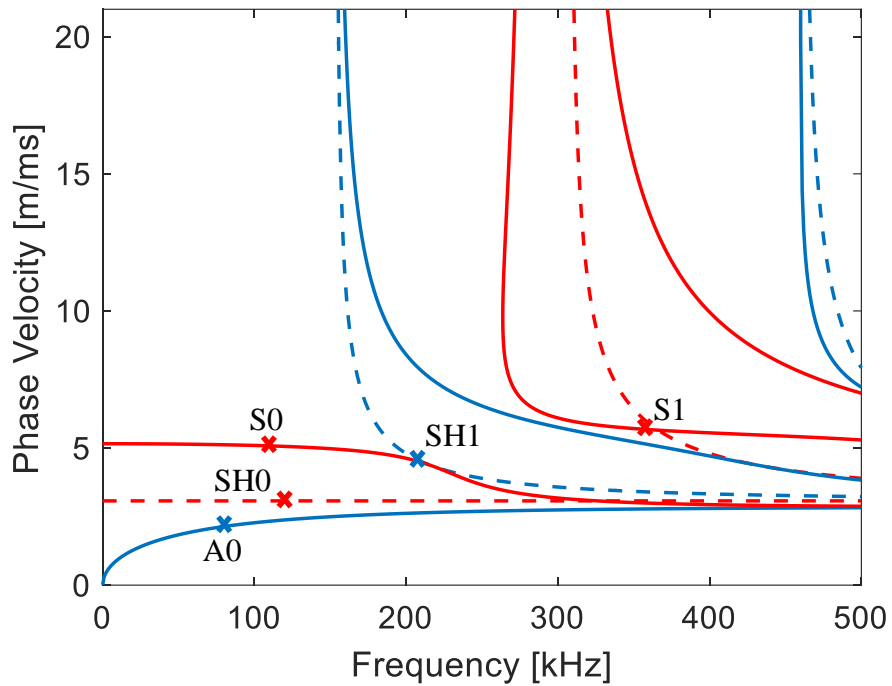


Fig. 30 Theoretical dispersion curve for guided waves in 10mm thick steel. Lamb (solid lines) and Shear Horizontal (dashed lines) wave modes are shown. Asymmetric modes are blue and symmetric modes are red, this graph was generated using the Dispersion Calculator Software (Centre for Lightweight Production Technology, DE). X's represent the frequencies of the wave modes used in this work.

SH0 was previously used in [127] but only for reflection from plate edges, so had to be evaluated for use on welds. A1 was not selected as in [55] it was found to have no reflection on the T-Joint weld. Rayleigh waves have previously been shown to have a small reflection coefficient from welds [170], [171]. However, their propagation distance is typically shorter than guided wave modes such as Lamb or SH waves so are inherently unsuited to echolocation type applications. In addition, generating a Rayleigh wave which will propagate a long distance in 10mm thick plate is practically difficult due to the very small wavelength of the wave produced, and hence will be strongly attenuated by very small surface defects [172].

4.3.1. Desired Wave Behaviours

The wave mode best suited to ranging from welds requires the characteristics described in the following paragraphs. Strong reflectivity from welded sections is the most important factor to consider when selecting the wave mode best suited for utilising guided waves for echolocation and ranging. If the mode does not reflect off of welds then ranging is not possible. A greater reflectivity makes it easier to do TOF calculations for ranging as well as making welds easily distinguishable from other structural features.

A particular weld is likely to have variations in its geometry across its length, so it is preferred that wave mode reflectivity is consistent with weld size and would change linearly and proportionally to a weld heads geometry that changes in size.

Low dispersion is desirable when dealing with guided waves. The range of wave propagation considered suitable is operating up to 2 m, initial testing showed dispersion was found to be manageable at this range. Fig. 31 shows SH1 signals for receiver positions at 200mm and 600mm from the weld, the geometry of the sample used is shown in Fig. 34. The weld reflection is identifiable even when the wave has a total travel path of 1.5 m, Path E Fig. 34, from transmission point to the weld and reflecting back to receiver.

To investigate the chosen modes Finite Element Analysis was used to test the wave modes that could not be evaluated experimentally. Simulations were validated experimentally on a subset of wave modes.

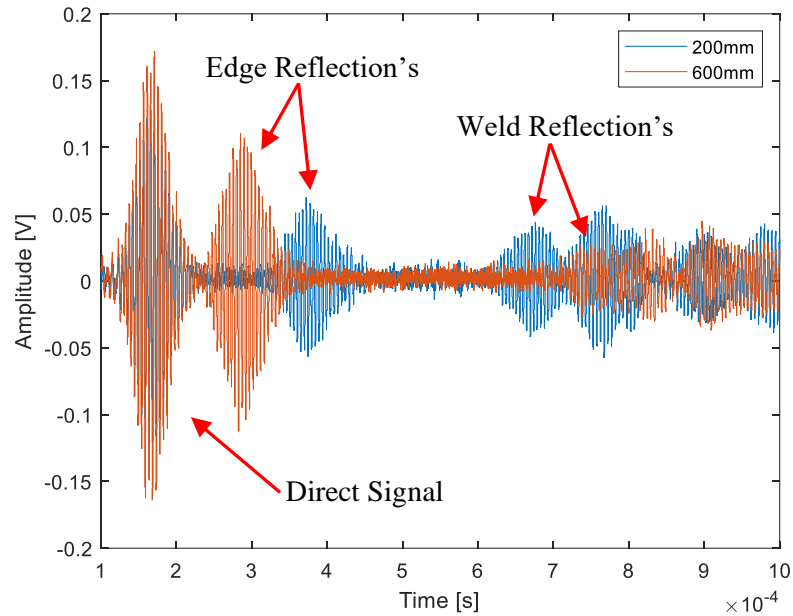


Fig. 31 Experimental data. First received direct signal, left edge reflection signals and weld signals are highlighted. SH1 at 205kHz was used on Sample 3 for these measurements. The blue signal is where the receiver is 20cm from the weld and the orange signal is where the receiver is 60cm from the weld.

4.4. Methodology

The wave modes indicated in Fig. 30 were investigated in 10mm thick S275-N Steel plate, 300mm width and 1500mm length, as this is commonly used in the construction of large oil and gas industry plant [173]. The material used is mild steel and as shown in [174] and [175] the grain structure of a parent metal and bead added via Metal Inert Gas (MIG) welding is approximately the same size, 34 μ m. The Heat Affected Zone (HAZ) will have significantly less effect on the reflection of the wave than the geometry changes of the bead, especially in the case of the samples used in this work, as such grain structure is not explored in simulation.

Visualising the geometry of a weld on plate, the presence of a weld causes an increase from nominal plate thickness, the wave mode which is best suited to ranging will react to this change in thickness by strongly reflecting from it. This requires the ideal mode to be sensitive to upper and lower boundary changes. The energy density distribution of a wave mode, for a given plate thickness, can be used to identify the areas of a plate thickness which carry the largest portions of a waves energy as it propagates, as this is typically varied across plate thickness. Analysis of the energy density distributions of the chosen wave modes across plate thickness, shows that A0, S1 and SH1 have a higher percentage of energy at the plate boundaries rather than a uniform or centre focussed distribution across the plate thickness, as shown in Fig. 32. The upper and lower boundaries of the plate are where the thickness increases when a weld head is present, and it is thought that modes which have an energy distribution favouring the plate boundaries will reflect well from welds.

Good reflectivity is also thought to be dependent on low mode conversion at geometric changes in a subject where thickness variation occurs. Significant mode conversion will cause the energy sent out to be spread across multiple wave modes, this will make it hard to distinguish a strong signal from noise and comparison to the initial signal very difficult. Most geometric features can be described as a thickness change [176]. A significant amount of work has been conducted into mode conversion of guided waves when encountering thickness changes within a subject [138], [176], [177], [178], [179], [180].

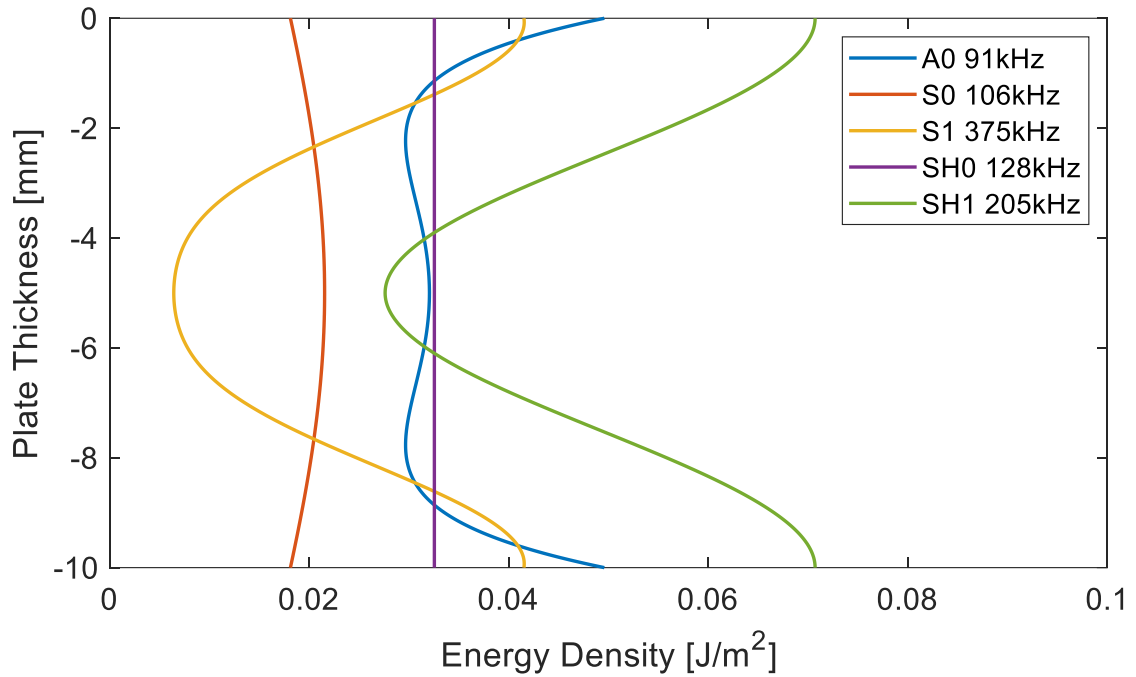


Fig. 32 Energy density (E_{Total}) distributions across 10mm plate for A0, S0, S1, SH0 and SH1 generated using Dispersion Calculator.

4.5. Simulation

4.5.1. Simulation Setup

Simulated and experimental results both used the same setup and had strong correlation. To obtain reflection coefficient values, the wave modes were propagated at a weld head. A transmitter generates a wave which is directed towards the receiver to measure the initial signal, this setup is shown in Fig. 33 and the propagation paths of the waves are shown in Fig. 34. Depending on the mode, the wave will not reflect, reflect or strongly reflect off of the weld and propagate back to the receiver. Using a 2DFFT based method the amplitude of the weld reflection signal and the first received signal can be obtained to gain

a reflection coefficient value. As the setup will remain the same for each wave mode investigated, the values for each wave mode can be easily compared.

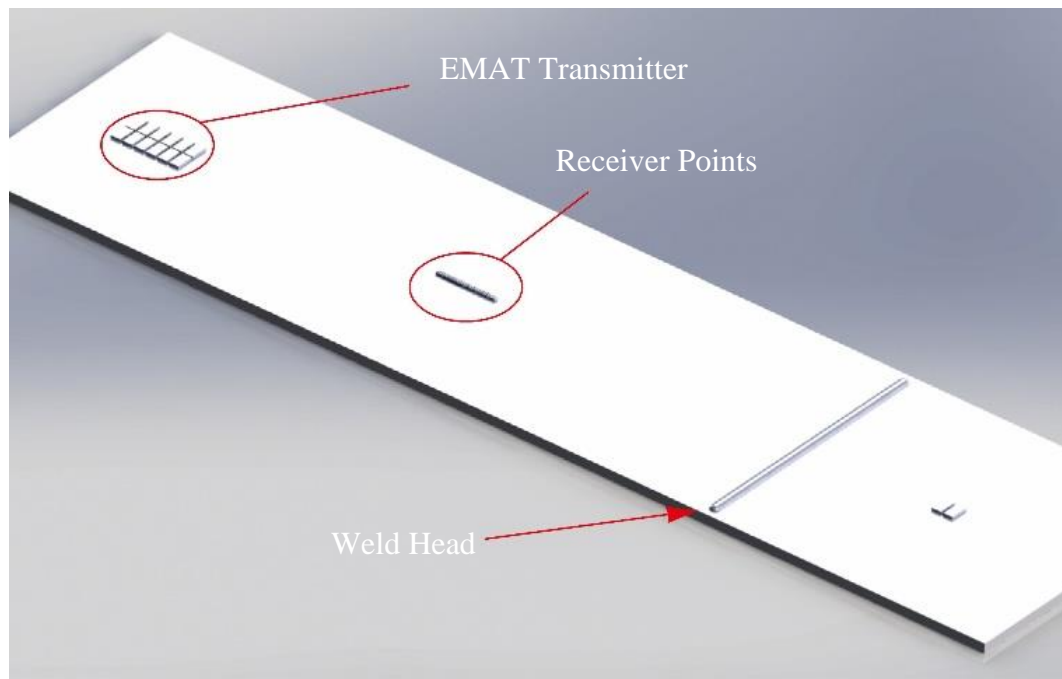


Fig. 33 The weld sample model with the PPM EMAT block representations and monitoring point representations for SH wave inspection, which allow measurement at 64 different points with 1mm spacing.

Fig. 34 shows the possible propagation paths that could be taken and will be referred to in the following descriptions. Transmitter and receiver EMAT's are separated 300 mm colinearly centre to centre, Path A. Experimentally the receiver is moved in 1mm steps over 64 mm to allow a 2DFFT to be performed on the data, R1- R2, in Figure 33. In simulation the steps are modelled as nodes, spaced similarly, which measure directional velocity changes over time. The transmitter/receiver setup is placed so that the receiver is 400mm from the weld, this means that wave paths A & C can be easily distinguished from

the other wave paths. This allows easy calculation of the reflection coefficient through comparison to wave A and wave C.

Plate dimensions are 1.5x0.3x0.01 m where the weld is 500 mm from the right-hand edge, this setup is the same for the experimental plates. Each of the modes were propagated at four weld heads with different geometries. Different weld heads were used to characterise a given wave modes reaction to small changes in weld geometry.

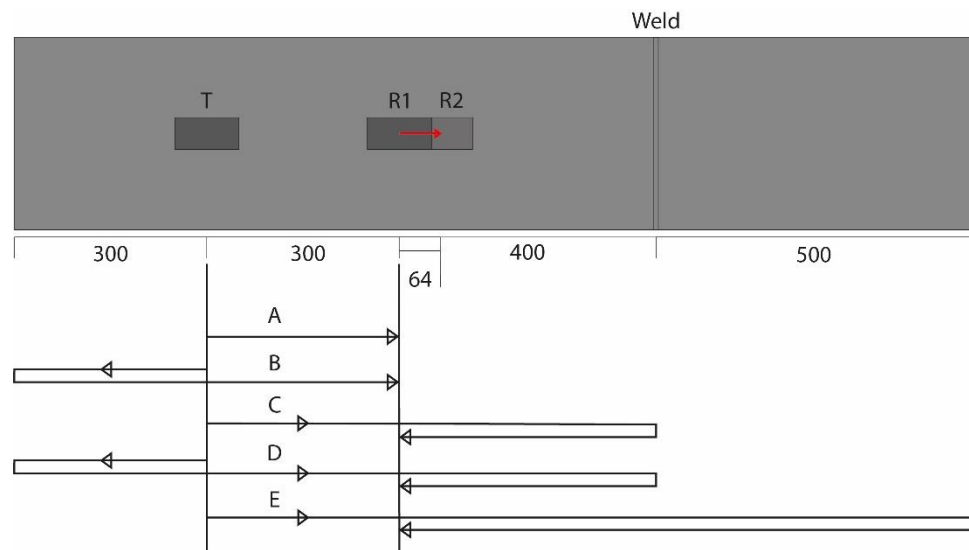


Fig. 34 The various key propagation paths of the waves generated in this setup are shown here with the propagation paths of interest being path A and path C.

The calculated weld head Cross Sectional Area (CSA) for each weld head is Table 3 given in. It is thought that the larger the CSA the higher the reflectivity. The different weld heads were manufactured, measured, and then modelled using Solidworks (Dassault Systems, FR), in simulation the weld microstructure [169], [181] was not modelled. It is thought to have some effect on the reflectivity of a wave mode but not significant enough to be a focus of investigation at this time [182], [183].

Table 3 – Calculated Cross Sectional Area of weld head samples.

| Sample No. | 1 | 2 | 3 | 4 |
|------------------------|-------|-------|-------|-------|
| CSA (mm ²) | 14.35 | 16.77 | 20.43 | 24.02 |
| Weld Height (mm) | 12.6 | 13 | 13.2 | 13.6 |
| Weld Width (mm) | 8.5 | 9.5 | 10.3 | 10.75 |

The EMAT model used to generate SH modes were a 6x2 magnet PPM configuration, where magnet dimensions were 20x10x5mm, Fig. 35 (a). The EMAT's were modelled from Sonemat (Sonemat Ltd., UK) sensors that were used for experimental measurement. OnScale (OnScale, US-CA) was used to run the simulations. The PPM EMAT model was used to generate SH0 (128kHz, 25mm wavelength) and SH1 (205kHz, 25mm wavelength) in simulation. To generate S0 (106kHz, 51mm wavelength), S1 (375kHz, 16.1mm wavelength), and A0 (91kHz, 25.4mm wavelength) modes, a meander coil EMAT was simulated [156], [184], [185], Fig. 35 (b).

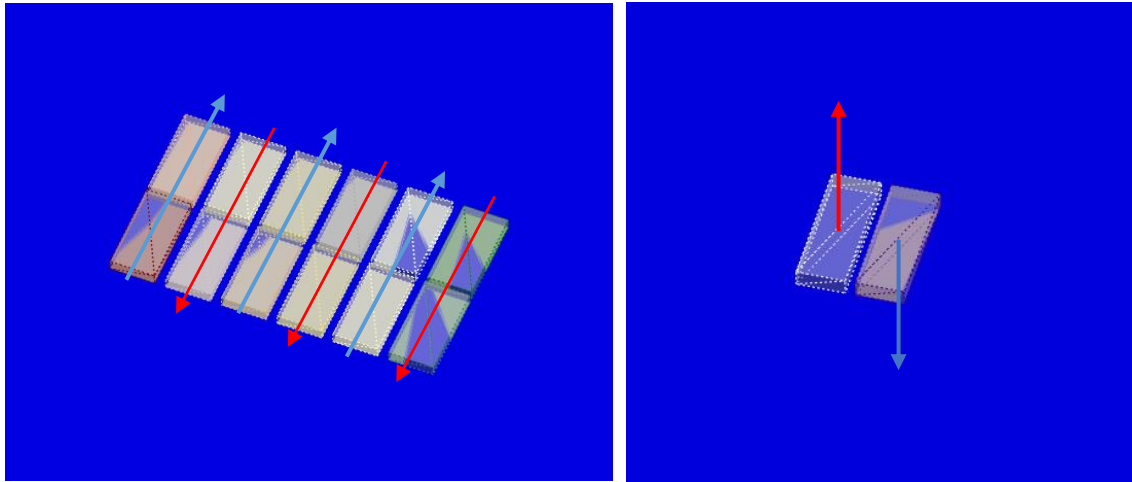


Fig. 35 a) SH generation block array, the arrows indicate the application of force when pulsed. b) Lamb wave generation block array the arrows indicate the application of force when pulse. In this case the application of force is perpendicular away from and into the subjects surface.

A 5-cycle sinusoidal pulse was used as the driving function [127]. 0.5mm mesh size was used for this model as a compromise between numerical stability and computational time vs. the time step for the Courant–Friedrichs–Lewy (CFL) stability criterion [186]. Adhering to the Courant–Friedrichs–Lewy (CFL) stability criterion is essential to ensure numerical stability in the simulation, as it dictates the maximum allowable time step based on the mesh size, wavelength and wave speed to prevent computational errors or divergence of the solution. Plate density was set to 7850kg/m^3 [187].

Fig. 36 shows an example of the simulations carried out to test wave mode weld reflectivity, in this example SH0 was propagated towards weld sample 4. The initial signal

generation can be seen, followed by wave propagation towards the receiver points and the waves interaction with the weld.

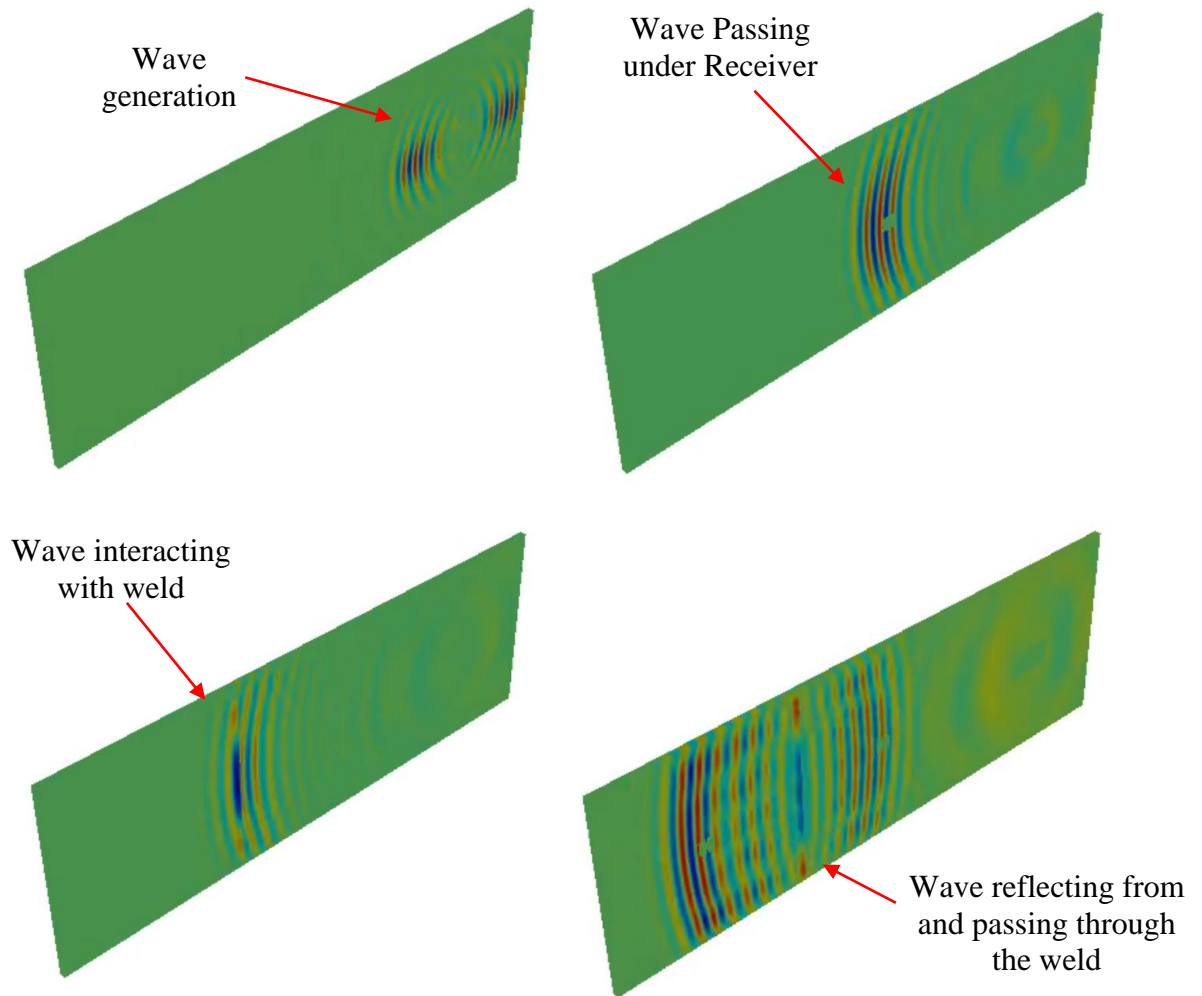


Fig. 36 a) Shows initial generation of SH0. b) Shows the first wave passing under the receiver points. c) Shows the wave encountering the weld. d) Shows the wave reflecting from and passing through the weld.

4.5.2. Data Extraction

To calculate the reflection coefficient values for the waves propagated in simulation and experimentally, a 2DFFT [188] was performed on the data to gain an accurate value of the amplitude of the initial signal and the reflected signal. 2DFFT is suitable for use with

dispersive and non-dispersive modes [55]. This can be used to better extract information from multiple A-Scans by taking measurements in the spatial domain as well as the time domain allowing isolation of specific frequencies and their amplitudes [141], [189], [190]. 2DFFT is also used to validate the wave modes generated experimentally and in simulation [141], [191].

To find the reflection coefficient for a given wave mode and weld size the following steps were taken:

- 1) 64 measurements were taken at intervals of 1mm, monitoring points in Fig. 33, where the receiver moves and the transmitter remains stationary to form a vector in the form of a 2D array data set. A specific time period is isolated so that only the first transmitted wave and the weld reflected wave are considered.

- 2) A 2DFFT is performed on this data which builds a 2D plot, Fig. 37, where it is organised by wavenumber, frequency and amplitude. A theoretical dispersion curve plot is overlaid. As mode conversion can occur at the weld reflection, and dispersion causes parts of the wave to spread out; using 2DFFT allows us to view dispersive modes this by organising amplitude by frequency and wavenumber, instead of in the time domain.

- 3) A vertical line at the centre frequency for the generated mode is drawn, to isolate this frequency, and the point where this line intersects the dispersion curve is isolated within this plot and a wavenumber/amplitude graph is generated for positive and negative wavenumbers, see Fig. 38 [192].

4) Using the wavenumber amplitude plot, the spikes which represent the first transmitted and first weld reflected waves can be identified. Integration is then performed on each spike to calculate the area under the spike, this is more accurate than taking the max amplitude value as it considers the changes in the width of the signal.

5) To find the reflection coefficient the area of the weld reflection spike is then divided by the area of the received signal spike, Fig. 38. Using this method the individual wave modes can be isolated, and the reflectivity calculated.

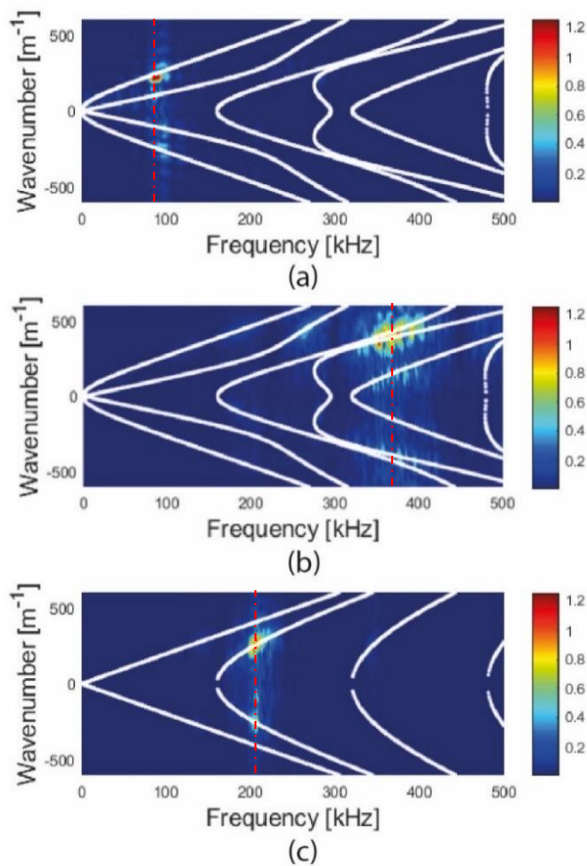


Fig. 37 Wavenumber-Frequency Amplitude plots for (a) A0 (91kHz) (b) S1 (375kHz) (c) SH1 (128kHz). The centre frequencies are highlighted. The mode conversion of the generated waves and the waves that returned after reflecting from the weld, are those with negative wavenumbers.

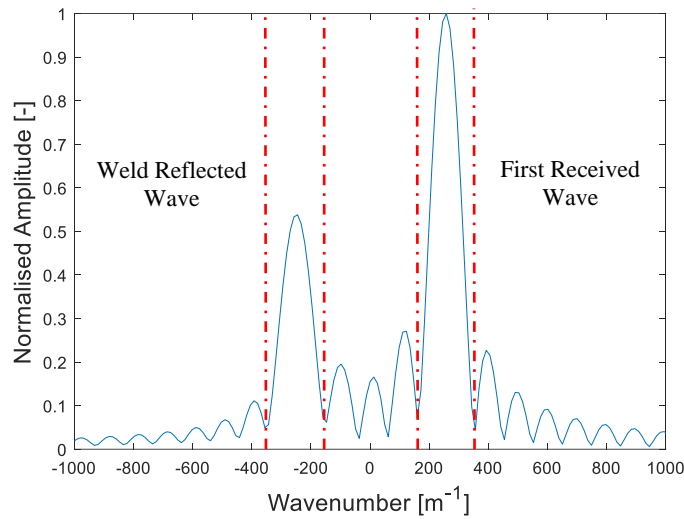


Fig. 38 An example of the Wavenumber-Normalised Amplitude plot that is used to find the magnitude of the first transmitted wave and the weld reflected wave, this example is for SH1 taken from the plot Fig 16c. The limits of the integration performed on the spikes are highlighted by the red dashed lines.

Using material datasheets [187], wave properties were calculated for the S-275N samples, including theoretical longitudinal and shear velocities [41]. To verify these values, bulk ultrasonic wave measurements and Time of Flight calculations were carried out on the experimental samples. The results for both theoretical and experimental values are shown in Table 4. The values calculated for both theoretical and experimental measurements are within suitable range of each other to support good correlation between simulation and experiment.

Table 4 – Sample Longitudinal and Shear Velocities

| | Longitudinal Velocity (m/s) | Shear Velocity (m/s) |
|----------------------------|-----------------------------|----------------------|
| Material Calculated Values | 6001 | 3208 |
| Experimental Test Values | 5959 | 3259 |

4.5.3. Wave Mode Simulation Results

Results for the wave mode simulations are graphed in Fig. 39. Fig. 32, shows the wavenumber-frequency distributions of A0, S1 and SH1, for direct and reflected signals, these modes have similar energy distributions which favour the boundaries of the plate.

For the frequency of A0 tested, minimal amounts of mode conversion to S0 occurs upon generation. A small amount of energy is reflected in equal amounts from A0 and S0, this indicates that mode conversion is occurring when the wave encounters the weld. S0 showed the same behaviour as A0, with mode conversion at the weld and very little of the mode reflected back to the receiver.

Significant amounts of mode conversion occur for S1 upon generation and when interacting with the weld, this made analysis difficult due to the noisy returning signal, this was also found in [169].

SH0 did not reflect strongly from the welded section, although the mode did not have significant mode conversion.

In simulation SH1 was found to be the most reflective out of the modes propagated, as was found in Table 5 of [55], however the focus of this paper was corrosion detection not ranging. SH1 showed the most desirable response for ranging by having the highest reflection coefficient and the reflectivity value changes were proportional to weld geometry changes.

Comparing the energy density distributions the level of mode conversion for A0, S1 and SH1, which all favoured the plate boundaries. SH1 has the thickness energy distribution

which best favours the boundaries of the plate, almost no mode conversion and it has the highest reflection coefficients found. This shows that the findings in simulation align with the theory discussed in 4.3, where a mode that has an energy density distribution that favours the plate boundaries will have a higher reflection coefficient. Although S1 has the second highest reflectivity, this was not able to be validated experimentally due to project limitations, as such SH0 was tested experimentally instead. Fig. 39 shows that SH0 has a higher average energy density than S1 so is a suitable replacement in experiment.

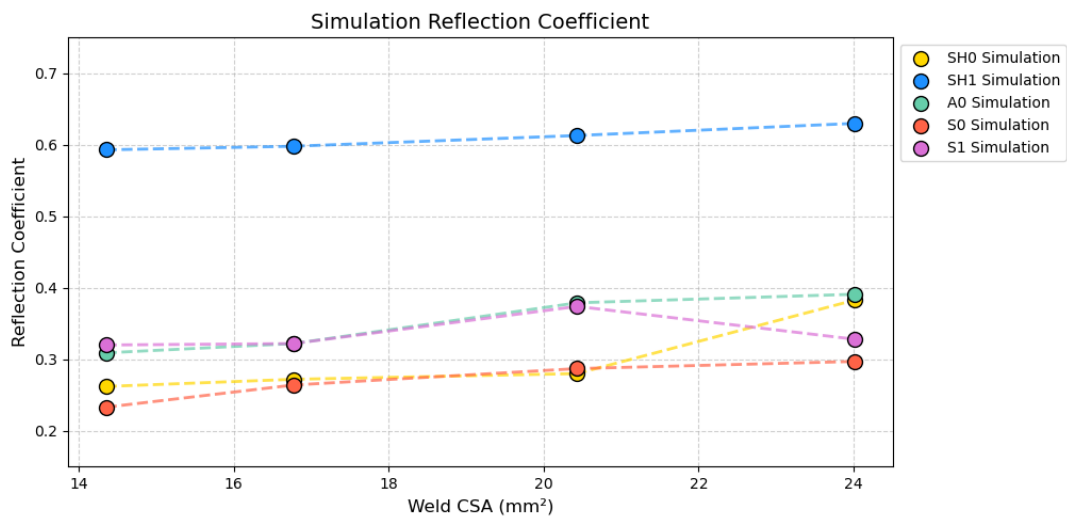


Fig. 39 Simulated data. The reflection coefficient for each mode and each sample is shown, SH1 is significantly more reflective than the other modes tested, S1 is the most reflective lamb mode. Good stability is shown by A0, SH0 and SH1.

4.6. Experiment

4.6.1. Weld Samples

Four 10mm S275-N Steel plates were used as the parent material of base test geometries. To minimise the variables within the experimental setup and to ease the manufacture process, weld beads were added straight to parent plates via MIG welding, instead of

directly butt welding two plates together. This enabled the geometry of the plate and weld cap to be representative but with minimal plate distortion on each side of the weld bead. The samples were manufactured in house via robotic welding, welding setup is shown in Fig. 40.

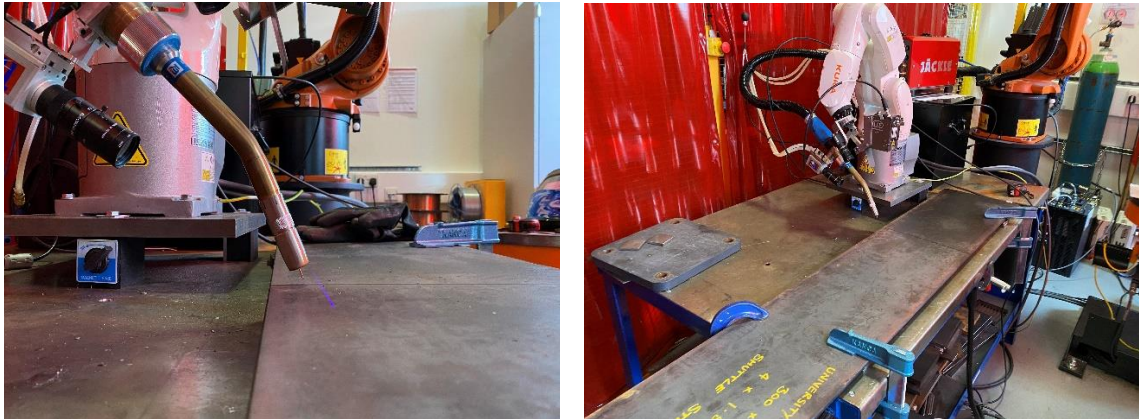


Fig. 40 A) Shows the welding angle of the robotic arm. B) Shows the welding setup with sample 2 clamped in place.

Table 3 lists the weld head geometry of the four samples, the weld on each plate was positioned 0.5m from the right-hand edge. The geometry measurements taken were used to model the plates in simulation. Sample 1 has the smallest CSA and Sample 4 has the largest CSA. The CSA values were designed to be within the same size ranges as real world samples.

4.6.2. Experimental Measurement Setup

The pitch catch setup used for the 2DFFT measurements is shown in Fig. 33 and Fig. 41, where the receiver EMAT is moved towards the weld in 1mm measurement steps. 1mm steps were deemed to be high enough resolution for an accurate 2DFFT whilst being able to maintain positional accuracy during sensor movement. The transmitter and receiver

were positioned so that the weld reflected signal would arrive at a different time than other signals, making it easier to isolate and identify the weld reflected wave from plate edge reflections, as experimentally they cannot be prevented as easily as they can be in simulation. Sonemat PPM EMATs, model numbers SHG2541-G and SHD2541-S with a wavelength of 25mm were used to generate Shear Horizontal modes SH₀, at 128kHz, and SH₁, at 205kHz. Both transmitter and receiver EMATs are constructed with two rows of six magnets, which provides narrowband excitation and reception.

A LabVIEW (NI Inc., US-TX) program was used to control the wave generation parameters. The laptop used to run LabVIEW was connected to a PicoScope 5000a (PicoTech, UK) to trigger a Ritec RPR-4000 Pulser/Receiver (Ritec, INC, US-RI), shown in Fig. 41. The Ritec generates a 5-cycle sinusoidal pulse with a reception gain of 50dB. A lift-off of 0.5mm was created between the EMATs and the sample so that the EMATs were able to be moved easily when measuring; lift-off and movement was achieved using 0.5mm thick PTFE sheets. A jig setup was used to ensure collinearity between the transmitter and receiver EMAT's.

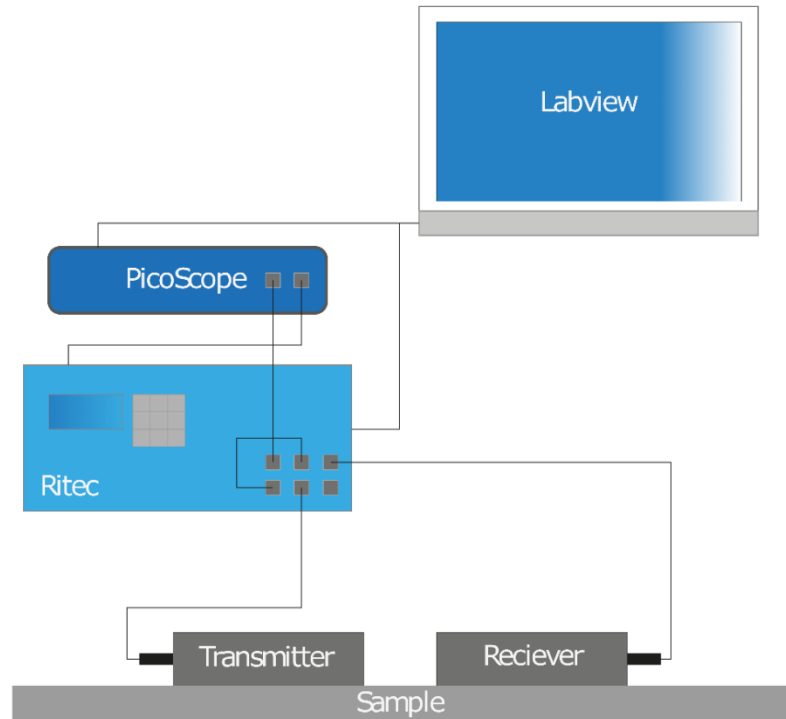


Fig. 41 Experimental setup where the LabVIEW programme is used to command the Ritec generating the pulses to send through the EMAT's. The signal from the receiver EMAT is sent to the Ritec, digitized in the Picoscope and sent back to the LabVIEW programme where it can be viewed.

4.6.3. Experimental Results and Comparison to Simulation

Experimental results are shown in Table 5. SH1 was significantly more reflective than SH0. Both modes responded to increased weld head geometry by increasing in reflectivity.

Table 5 - Experimental Reflection Coefficients for SH0 and SH1

| | CSA (mm ²) | SH0 (128 kHz) Experimental | SH1 (205 kHz) Experimental |
|----------|------------------------|----------------------------|----------------------------|
| Sample 1 | 14.35 | 0.145 | 0.409 |
| Sample 2 | 16.77 | 0.134 | 0.416 |
| Sample 3 | 20.43 | 0.188 | 0.442 |
| Sample 4 | 24.02 | 0.308 | 0.493 |

As can be seen in the results there is a difference in the strength of the reflection coefficients between simulation, Fig. 39, and experiment, Table 5, there are multiple factors contributing to this increase in coefficient value.

The experimental welds are not completely consistent and have some variation in their bead size across their length, in simulation this is not the case. Real world weld variations are normal and as a result at different positions along the weld the reflection coefficient will vary slightly. The plates in simulation can be considered perfect meaning there is less signal loss in the simulation sample than the physical plates, which will have many minor flaws causing additional losses in amplitude.

To further validate good correlation between simulation and experiment, SH0 and SH1 reflection coefficients were plotted using simulation and experimental results, shown in Fig. 42. The data points were then used to generate a best fit line which using the gradient of the line a trend value could be established. For both experiment and simulation there is an absolute value difference of gradient equal to 0.005 which shows there is good correlation between simulation and experiment.

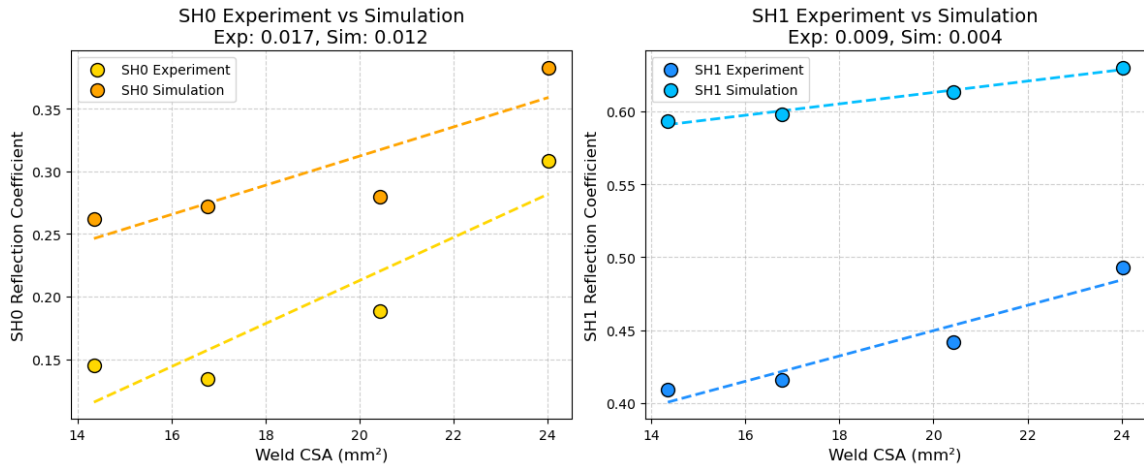


Fig. 42 Plots of SH0 and SH1 experimental and simulation data plotted with a best fit line to find the trend value using the best fit line gradient.

4.7. Ranging Evaluation

To evaluate the ranging capabilities of SH1, as well as SH0, waves were propagated at the weld bead from varying stationary transmitter and receiver positions, so that relative distance between the receiver and the weld could be estimated, this is ranging. Waves of frequencies 128kHz (SH0) and 205kHz (SH1) were generated in Sample 4 and propagated at the weld from the different positions shown.

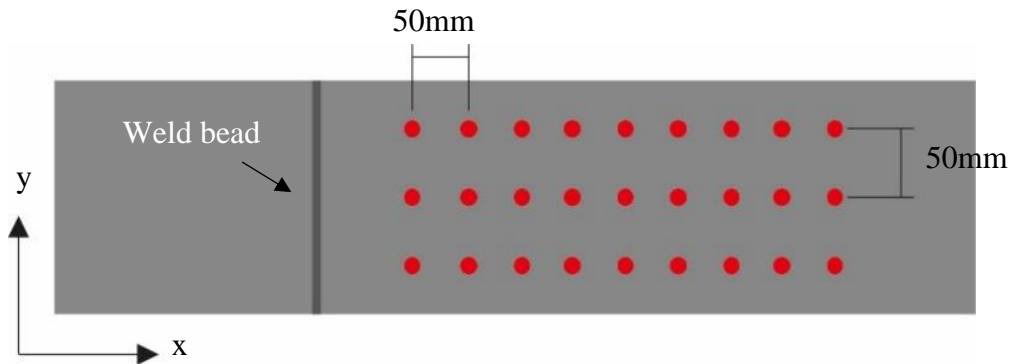


Fig. 43 Each red dot represents the positions for the receiver when propagating the modes at the weld for range and distance estimation, the transmitter and receiver EMAT's are kept 300mm apart and colinear for all measurements.

Fig. 43 shows the distinct positions of the receiver EMAT. The EMAT pair was positioned at three different points along the y-axis and moved back in 50mm steps from the weld along the x-axis, measurements further than 650mm from the weld were not carried out as the sample length did not allow it. The weld geometry is inconsistent across its length, with variation of up to $\pm 2\text{mm}$ each side, so an average of three measurements across the weld will give a more realistic picture of a modes ranging capabilities than a signal measurement at one point.

Human error when placing the EMAT's had a minor contribution to the error of the modes ranging accuracy due to the high magnetic forces between the EMATs and sample. The results for the estimated and actual distances are graphed in Fig. 44.

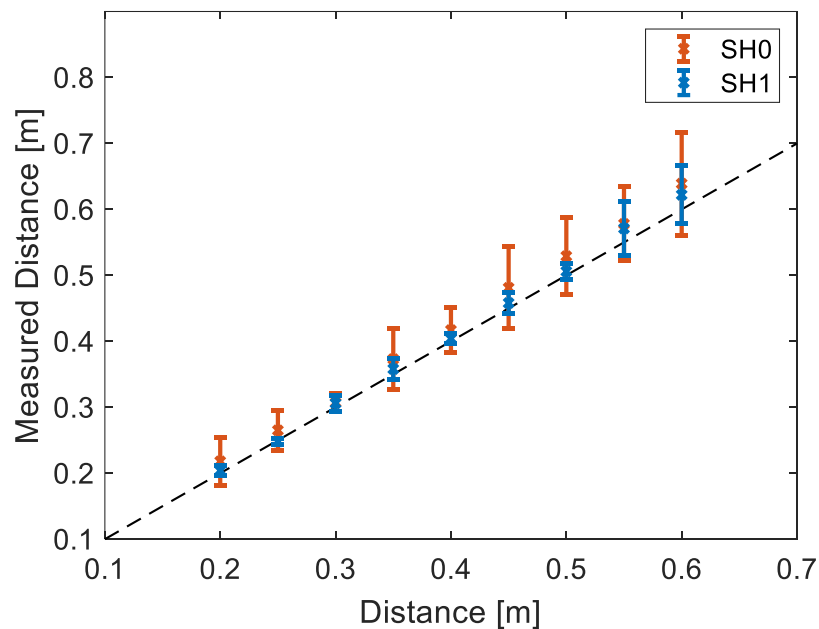


Fig. 44 Distance is the distance from receiver to the weld. Distance vs Estimated Distance of SH0, group velocity 3259m/s, orange, and SH1, group velocity 2000m/s, blue, in experiment. The dashed line shows the exact position of the weld to the centre of the EMAT.

Ranging accuracies were evaluated by comparing the actual distance, measured by hand, and the measured distance, measured using guided waves time-of-flight, between the weld and the receiver. A combination of time-of-flight and Short-Time Fourier Transform (STFT) was used to calculate the distance between the weld and the receiver using measurements [138].

First, the measurements were arranged and plotted by time (x-axis) and frequency (y-axis), where increases in amplitude can be seen via colourmap, Fig. 45 A. The frequencies of 128 kHz (SH0) and 205 kHz (SH1) were then individually extracted so that the time that reflections occur could be viewed. The first received wave and reflection are marked on Fig. 45 B. Using this time information, combined with the wave velocity of each mode taken from dispersion curve plots, the distance the reflection travelled can be calculated. The difference between the calculated distance and the measured distance, which was known, was then used to find the wave modes ranging accuracy/error.

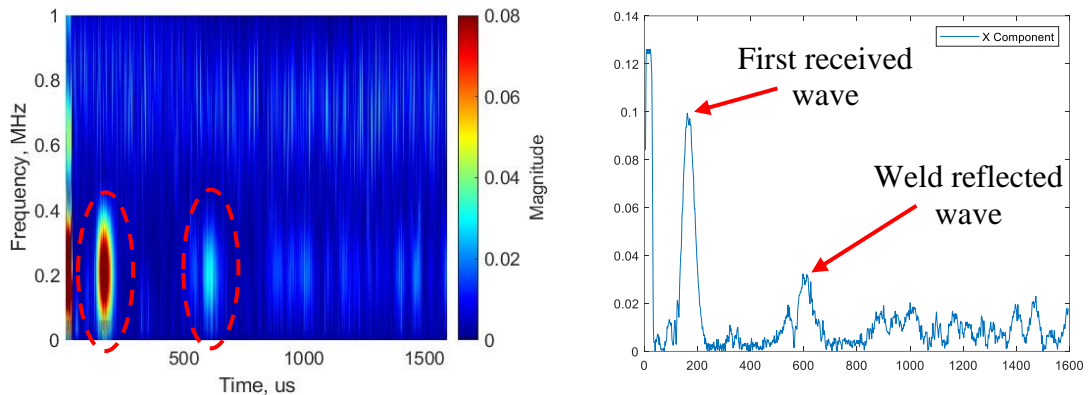


Fig. 45 A) Shows the STFT plot used for each frequency tested vs time with the magnitude of the amplitude. B) Shows the selected frequency plotted in isolation to identify the reflected signal.

As shown in Fig. 44, SH1 can be used to accurately estimate the distance from the receiver to the weld, better than SH0, as across the different distances to the weld SH1 had higher positional estimation accuracy and less error throughout than SH0. The overall positional estimation error of SH1 was 2.65% and the overall positional estimation error of SH0 was 5.96%. For SH1 at an EMAT pair position ≥ 75 cm from the weld, interpretation of the weld reflection became harder. This is thought to be due to dispersion, where the group velocity is a less accurate value to use for calculating the weld distance and the spreading out of the signals energy, results in the reflection signal becoming harder to identify.

Comparing this to the methods listed in Table 6, positioning using guided waves shows good performance, with the error value at +/- 1.99cm when using SH1. The updated Table below lists the guided wave performance as compared to the methods discussed previously.

Table 6 – List of positioning methods with SH0 and SH1 added.

| Positioning Method | Positioning Error |
|---|----------------------------|
| SH0 Positioning | +/- 4.5cm (Error) |
| SH1 Positioning | +/- 2cm (Error) |
| Laser Positioning (Pose Tracking) [109] | +/- 5.3cm (Minimal Error) |
| Radio Waves (Extended Kalman Filter) [110] | +/- 23cm (Minimal Error) |
| Odometry (IMU and Encoder) [111] | +/- 50cm (Maximal Error) |
| Camera/Laser Data Fusion (Extended Kalman Filter) [112] | +/- 10.3cm (Minimal Error) |
| 3D Vision System and Natural Landmarks (Extended Kalman Filter) [113] | +/- 1.8cm (Minimal Error) |
| Vision Assisted GPS [114] | +/- 5cm (Minimal Error) |
| LiDAR (Multi-Sensor Setup) [115] | +/- 11.1cm (RMSE) |
| Wireless Sensor Network and IMU (H Filtering) [116] | +/- 13.1cm (RMSE) |

4.8. Investigation Conclusion

In order to identify the optimal guided wave mode for echolocation/ranging on large industrial plant, various guided wave modes were investigated against for weld reflectivity. Welds can be clearly detected using the SH1 wave mode and the position of a weld relative to the position of the receiver can be accurately estimated at the distances evaluated using this mode. SH1 is a dispersive mode, however, during experiment and simulation this was not a significant issue due to the ranges of propagation and the narrowband signal used.

A 2.65% estimation error for SH1 over multiple positions is considered suitably accurate for ranging and mapping over reasonable distances that would be expected on large steel plant such as pressure vessels.

As SH1 was found to be the best suited mode for ranging from welds, an optimised PPM EMAT was constructed to efficiently generate SH1 from a mobile robot. This optimisation methodology is presented in Chapter 5.

Chapter 5

5. Design and Manufacture of an Optimised Side-Shifted PPM EMAT Array for Use in Mobile Robotic Localisation

5.1. Introduction

Following the investigation into the best suited guided wave mode for ranging from welds in plate like structures in Chapter 4, an optimisation methodology for bi-directional and uni-directional PPM EMATs is presented. This methodology optimises the EMAT design in two areas; maximising the eddy currents inducted into a sample by optimising racetrack width and number of turns; and optimising the magnet size and spacing for maximising the background magnetic field without increasing the number of magnets. The efficacy optimisation methodology is measured through direct comparison to a commercial EMAT.

This optimisation methodology is then applied to a sensor setup best suited to mobile robotic application. The resultant sensor setup offers considerable benefits over a

bidirectional transmitter in a pulse echo, pitch-catch configuration. A comparison of the two setups is presented.

5.2. Optimising Sensor Setup for Positioning

The transducer setup used in [127] is typical for mobile robotics, however is not optimal for echolocation and ranging as the transmitter simultaneously produces both a forward and backward SH1 wave during generation. In a finite subject, due to bidirectional generation, it is difficult to interpret data in real-time using a single receiver, as the propagation path of a received reflection is unknown, so the position of the reflective feature relative to the transducer setup is ambiguous. To overcome this, two receivers can be used, Fig. 46, to determine the generation direction of a reflected wave and, subsequently, its travelled path using time of flight methods. When a two receiver setup is used, a received signal will arrive at each receiver at slightly different times provided the receivers are at unequal distances from the transmitter. From this time difference in arrival, the direction that the signal was travelling can be interpreted, this is illustrated in Fig. 47.

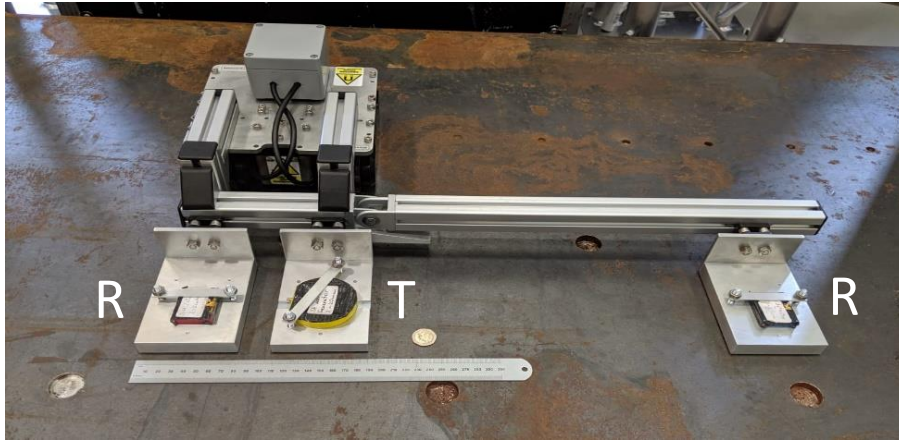


Fig. 46 An example of a two receiver, bidirectional transmitter EMAT setup using miniaturised EMATs, fixed to a mobile robotic crawler. The transmitter is the circular yellow sensor labelled T, the two receivers are labelled R.

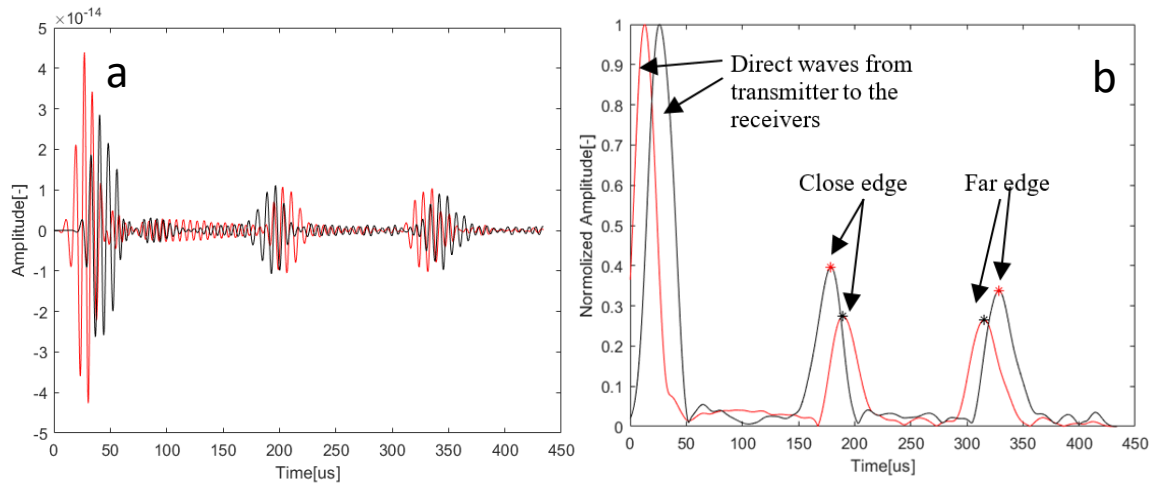


Fig. 47 (a) Shows the signals received from the two receivers, it can be seen that there is a small offset in phase between both red and black. (b) Shows the normalised envelopes of the signals shown in (a), where the edges reflections from the subject can be seen. The difference in phase between the two signals can be used to identify the direction of features relative to the transducer setup.

When utilising a bi-directional transmitter ranging dead zones can occur, where two signals, initially generated in opposite directions, can return to a receiver at the same time,

so the direction of each individual signals cannot be determined easily. To solve this a second receiver is added to the setup so that there is an time offset between a given signal when it arrives at each receiver, from this the direction that the signal was travelling can be interpreted through comparison. The difference shows which receiver the signal arrived at first, this implies the direction the signal travelled.

Furthermore, using two receivers greatly increases the footprint of the transducer setup as well as the magnetic hold force, which can impede robotic crawler movement. Reducing the EMAT size for use on robotic crawlers has been explored in [193]; this was achieved by reducing the size of the magnet array and coil in standard PPM EMATs. However reducing the size of the EMAT causes the generated signals to be weaker and noisier compared to larger footprint EMATs, making signals harder to interpret.

The EMATs used in [127] are traditional commercial PPM EMATs transmitter in a pitch-catch setup, where, in order to produce waves with increased amplitudes, high voltages have to be applied to the transmitter and the distance between subject surface and the transducers has to be minimised without making contact with the surface. EMATs typically have low SNR, which is a well-known issue [139], [185], however this is exacerbated when using EMATs in a mobile robotics context as strong magnetic holding forces from the EMATs mean that separation from the subject surface must be maintained as the EMATs may become stuck, fixing the robot in place. As well variations in lift-off can affect signal quality due to the change in distance from the transducer to the subject surface.

Additionally to generate guided waves with high voltages, a special pulser is required, applied to a robotic system. The use of a pulser brings the same difficulties of an umbilical cord used for providing coupling fluid for bulk ultrasonic measurements. Low SNR and poor transduction efficiency is a well-known issue with EMATs, however in literature there is little work on the optimisation of PCB racetrack coil EMATs to improve the issues found with producing high amplitude waves with low excitation voltages resulting in low transduction efficiency.

An omni-directional EMAT setup was not used as the sensor of choice in this work due to the increased magnetic holding force and setup complexity. As well the complexity of signal interpretation is increased when using an omnidirectional sensor. One of the aims of this work is to reduce setup complexity.

Air-coupled transducers were considered, as Dobie et al. [194] has shown that they can be used in a mobile robotic setting. However in Chapter 4, SH1 was determined to be the wave mode best for ranging, air-coupled transducers aren't practical for generating shear horizontal modes, therefore air-coupled transducers were not used.

This work looks to address the problems highlighted through developing a PCB PPM EMAT optimisation model which aims to maximise the SNR for a given set of EMAT footprint dimensions. This model is then used to optimise the efficiency of a unidirectional transmitter PPM EMAT setup, which is better suited to mobile robotic ranging. This setup removes the ambiguity around the direction of the received signal as the initial direction of the wave is always known, so ranging can always take place with no dead zones. This setup also removes the need for the second receiver which significantly reduces the

footprint of the transducer setup, reduces the total magnetic holding force added by the sensors, and reduces the complexity of signal analysis.

The optimisation framework focusses on increasing the Lorentz force output in PPM EMATs to increase the SNR of the signals produced. This is done through coil and magnet array optimisation and uses dimensional parameters as the input to output the parameters used to achieve the highest Lorentz force for the user set input parameters. This framework will also give the reader some direction on designing their own PPM EMAT. The optimisation framework is evaluated through comparison of the signals produced by a commercial EMAT and an optimised EMAT with the same dimensional parameters, when pulsed with the same signals.

The unidirectional side-shifted PPM EMAT will be constructed using two offset coils and magnet array which are then pulsed independently with one pulse 90° out of phase from the other, similar to that in [21]. In addition, a receiver EMAT will be manufactured; this will then be packaged together with the transmitter as one small unit for ease of deployment onto a mobile robotic system. Following the design and experimental validation of the mobile robot focussed transmitter/receiver set-up, its ranging capabilities were evaluated by comparing it to the two-receiver bidirectional transmitter setup. Evaluation was carried out through comparison of the two different setups through their ability to range at all measurement points, and the number of measurement points that can be taken by a given setup. Considerations have been made to reduce the obstruction of robot mobility through reducing the high magnetic strength or large package size.

5.3. Optimisation and Methodology

EMAT performance optimisation was achieved by increasing the Lorentz force induced into the subject as much as possible without the use of extremely high voltages or high force permanent magnet arrays which would be unsuitable for use in mobile robotics applications. The Lorentz force was focused on as it is typically the main generation mechanism when applied to materials such as steel and aluminium [46], [151].

To do this, the racetrack coil has been optimised to maximise the induced eddy current, increasing \mathbf{J}_e and $\tilde{\mathbf{B}}$, and the magnet array has been optimised for the appropriate magnetic field vector value, $\bar{\mathbf{B}}$. The Lorentz force, \mathbf{f}_L , is shown by:

$$\mathbf{f}_L = \tilde{\mathbf{f}}_L + \bar{\mathbf{f}}_L = \mathbf{J}_e \times (\tilde{\mathbf{B}} + \bar{\mathbf{B}}) \quad (5.1)$$

$$\mathbf{f}_L = \begin{cases} \mathbf{J}_e, \tilde{\mathbf{B}} \propto \sin \omega t \\ \bar{\mathbf{B}} = \text{const.} \end{cases} \quad (5.2)$$

As in Chapter 4, [23], SH1 was found to be best suited for ranging from welded section, SH1 is used in this work and will be generated in a 10 mm steel plate, therefore the dimensions of the magnet arrays are set to fit a 25 mm wavelength, which generates SH1 at 205 kHz, and the coils were designed to appropriately cover the surface area of the magnet array that sits on top of the coil.

During the design process, experimental manufacture and use were kept in mind; this was applied to multiple parameters of the design process, as it was preferred to have a design that was transferrable from simulation into practical experimentation without significant design changes.

5.3.1. Transmitter Coil Optimisation

This section describes the numerical model created for optimising the racetrack coil. The model operates by taking a number of coil design parameters and then iteratively working through the possible options for coil trace widths and the number of turns. This is done to find the set of values that give the highest induction of eddy currents, J_e , into the sample, which is done through maximising the strength of the magnetising fields generated by the alternating current in the coil [46], [195]. Practically, this means maximising the induced eddy currents, which is achieved through optimising the trace width and trace spacing, maximising power transfer and impedance matching the pulser generator pulsing the coil [196]. Subject characteristics are also required as input value for the model.

The coil optimisation shown here is intended for use on Flexible Printed Circuit Board (FPCB) coils and not hand wound coils. There are multiple benefits to using FPCB coils over hand wound coils, which include the following: high coil flexibility easing construction; greater influence over wire/trace parameters to control performance; increased wire/trace to sample surface contact, which increases eddy current induction; precise manufacturing; and a low profile [46].

The input parameters for the numerical model are as follows:

Coil Dimensions are illustrated by Fig. 48

C_{length} - Total coil end to end length (mm)

C_{width} - Total coil width (mm)

M_{width} - Width of magnet that is to be covered (mm)

PCB Manufacturing Inputs, *typically set by manufacturer.*

$G_{minimum}$ – Minimum gap (mm) between traces

$T_{minimum}$ – Minimum manufacturers trace width (mm)

W_{Cu} – Copper Weight (oz/ft²)

$P_{thickness}$ – PCB Thickness (mm)
 G_{sample} – Distance from sample (mm)

Experiment Variables, *parameters regarding pulsing.*

V_{in} – Voltage at pulser source (V)

Z_{source} – Impedance at pulser source (Ω)

f – Intended frequency of pulsing (kHz)

S_M – Sample Material (requires inductance vs distance plot)

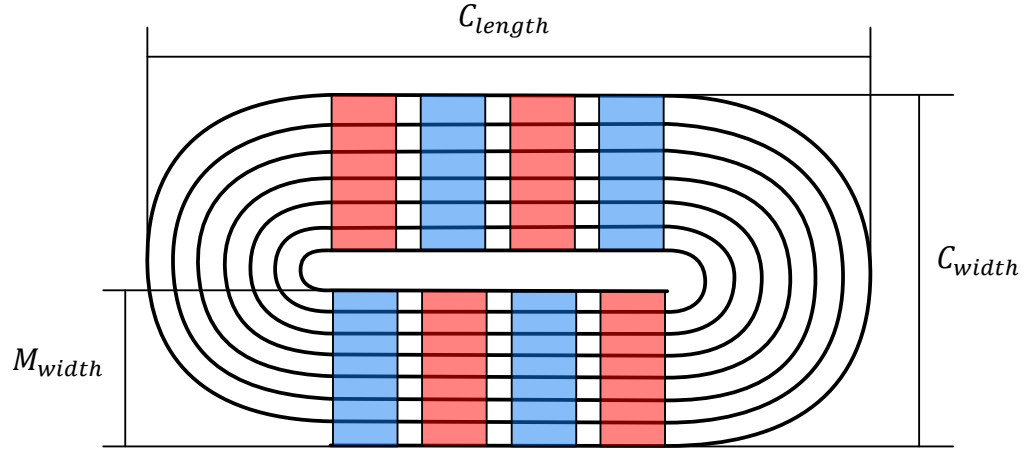


Fig. 48 Geometrical coil input parameters for the numerical model, shown diagrammatically.

The coil dimensional parameter inputs were designed to match the EAGLE (Autodesk, Inc. CA, USA) User Language Programme (ULP) that was used to generate the files for manufacturing the PCB coils, this ULP is a spiral coil generator [197]. This eased transfer of coil dimensions output by the model into the manufacturing process. The model operates in the following way:

Following the input of parameters listed, the applicability of the skin effect is assessed using (5.3), where ρ_{Cu} and μ_{Cu} are respectively the resistivity and permeability of Copper, μ_0 is the permeability constant. This equation is used to determine whether the skin effect is substantial enough to be considered effective at the intended sensor operation frequency.

If the skin effect is considered negligible the model does not include the skin effect. If the frequency of the signal that is intended to be used is high enough that the skin effect begins to occur, the model will stop running. However, the operating frequencies of EMATs are typically below the values where the skin effect, S_E , applies.

$$S_E = \sqrt{\frac{\rho_{Cu}}{\pi f \mu_0 \mu_{Cu}}} \quad (5.3)$$

The model then iterates through a number of possible turns, N , within the set coil dimensions until the trace width, $T < T_{minimum}$. For each iteration of N the following steps are taken.

The value for $G_{minimum}$ for each iteration is set to the largest value from either: the IPC2221 lookup table [198], based on the input voltage, or the minimum manufacturers gap. The trace width, T , required to meet the value of M_{width} for an iteration is calculated using (5.4).

$$T = \frac{(M_{width} - G_{minimum}(N - 1))}{N} \quad (5.4)$$

Following the process in [199], the critical dimensions are then calculated for the coil based on C_{length} , C_{width} and M_{width} . This process allows the coil to be generated as a series of end connected line segments, in the case of this work the Track Width Ratio (TWR) factor is set to 1 to maintain constant trace width through each turn. The lengths of each line segment in each turn of the coil can be calculated and parallel segments are grouped together for analysis. The total trace length T_{TL} is the sum of all trace segment lengths where T_{AL} is the average turn length, T_{TL}/N .

Inductance is then calculated for each iteration of N in the following way. [200] gives a method for calculating L_{SI} , the summation of the self-inductance of the coil segments. L_{MI} is double the summation of mutual inductances of each line segment to all other line segments calculated following the method in Section III of [199], doubled summation is utilised as symmetry is used in the calculation. The inductance of the coil, L , is calculated using (5.5). The inductive reactance, X_L , is calculated using $2\pi fL$.

$$L = L_{SI} + L_{MI} \quad (5.5)$$

The capacitance of each iteration of N is measured between the input and ground return, given by (5.6) from [201] using the case of air and FR4 substrate, a common substrate used in PCB manufacture, where ϵ_{Air} is the permittivity for air, ϵ_{FR4} is the permittivity for FR4 substrate, ϵ_0 is the permittivity of vacuum. The capacitive reactance, X_C , is then calculated using $1/2\pi fC$.

$$C = N \frac{T^2 \epsilon_0 \epsilon_{FR4}}{P_{thickness}} + \frac{(0.9\epsilon_{Air} + 0.1\epsilon_{FR4})\epsilon_0 W_{Cu} T_{TL}}{NG_{minimum}} \quad (5.6)$$

The resistance of each iteration of N is then calculated using (5.7) from the total length of the coil, C_{TL} .

$$R = \frac{\rho_{Cu} T_{TL}}{W_{Cu} T} \quad (5.7)$$

The impedance of each iteration of the coil is calculated using a planar coil model [201] shown by (5.8). This impedance value is then adjusted to account for the impedance of air and the impedance of the material under inspection and the EMATs distance from its surface.

$$Z = \frac{(R + X_L)X_C}{R + X_L + X_C} \quad (5.8)$$

$I = V/Z$ is then used to estimate the current. Using the current, the magnetization, M_N , of each iteration of N can be calculated with $M_N = NI$. Thus, the optimum number of turns and trace width can be established through finding which iteration of N produces the highest magnetization from the values of the input parameters, the highest magnetization will come from $Z = Z_{Source}$. The model outputs a curve of magnetization vs. no. of turns as well as the optimal trace width and no. of turns that are used as ULP inputs to generate the FPCP coil.

For clarity, the numerical implementation of the algorithm related to the optimisation of the transmitter coil is presented in Table 7.

Table 7 – Pseudo Code of the Numerical Model

| |
|---|
| <p>Given $C_{length}, C_{width}, M_{width}, G_{minimum}, T_{minimum}, W_{Cu}, V_{in}, Z_{source},$</p> <p>1. $N \leftarrow 1$ 2. repeat 3. $T \leftarrow \frac{(M_{width} - G_{minimum}(N-1))}{N}$ 4. Calculate T_{TL} 5. $T_{AL} \leftarrow T_{TL}/N$ 6. Calculate L_{SI} [35] 7. Calculate L_{MI} [34] 8. $L \leftarrow L_{SI} + L_{MI}$ 9. $X_L \leftarrow 2\pi fL$ 10. $C \leftarrow N \frac{T^2 \epsilon_0 \epsilon_{FR4}}{P_{thickness}} + \frac{(0.9\epsilon_{Air} + 0.1\epsilon_{FR4})\epsilon_0 W_{Cu} T_{TL}}{NG_{minimum}}$ 11. $X_C \leftarrow 1/2\pi fC$ 12. $R \leftarrow \frac{\rho_{Cu} T_{TL}}{W_{Cu} T}$ 13. $Z \leftarrow \frac{(R + X_L)X_C}{R + X_L + X_C}$ 14. $N \leftarrow N+1$ 15. if $Z = Z_{source}$ 16. return N, T // return values and exit the program 17. end 18. until false</p> |
|---|

5.3.2. Transmitter Magnet Array Optimisation

To optimise the magnet array of a PPM EMAT being used for mobile robotics, a balance needs to be made between increasing the static magnetic field, \bar{H} , induced in the plate, and not increasing \bar{H} beyond the point that it impedes the robots movement [50], as increasing \bar{H} will increase \bar{B} which increase the applied Lorentz force. Optimisation options for \bar{H} are limited with PPM EMATs, the constraints that have to be considered are as follows; magnet spacing determined by choice of wave mode/wavelength; magnet array layout determined by style of the PPM EMAT; practically available magnet sizing options; choosing broadband or narrowband generation/reception; and the balancing the magnetic array strength to allow mobile robotics to allow movement whilst producing good quality signals [50].

Using the magnet arrangement shown in Fig. 49 as a reference example, the centre to centre spacing of magnets with the same polarity in the same row is determined by the wavelength [138], in the example this is 25 mm. A paper [202] by Rose carried out a study on the elements in comb style transducers for generating guided waves, which showed that when increasing the magnet width, w , over 50% of the length S (Fig. 49), little change in the generated wave amplitude is observed. However, acquiring Neodymium magnets of specific widths is not as practical as buying standard off the shelf sizes, which results in using magnets of $w > S/2$, this can have a small effect on performance but is typically cancelled as this will usually increase the static magnetic field, \bar{H} , due to increased magnet size. It is not recommended to use magnets of width, $w = s$, as this will

be difficult to manufacture and will result in increased wave harmonics creating additional noise and no real amplitude gain compared to $w > S/2$ [202].

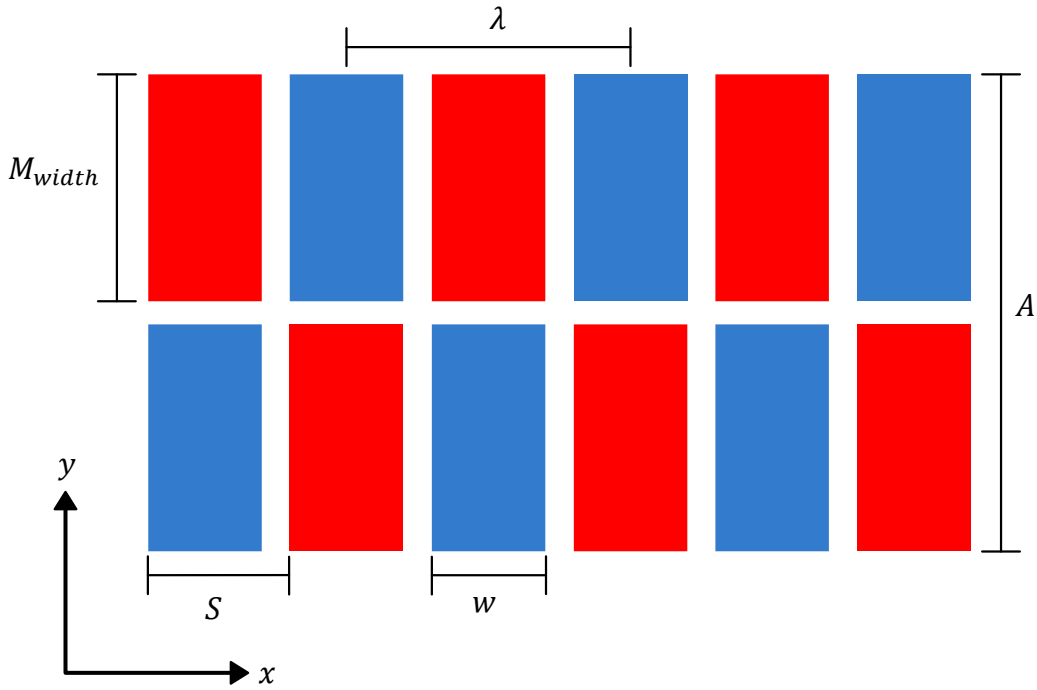


Fig. 49 Diagram showing the magnet array spacing dimensions for PPM EMAT based on [202] and [203]. The red and blue rectangles represent the magnets and their polarization.

The width of the wavefront is determined by the outer edge to edge distance of the magnet in the y-direction, in the case of the example, Fig. 49, this is 41 mm, the magnet width determines the width of the coil. The total width was used to calculate the beam spread of the EMAT using (5.9) [203], where the width is aperture A , λ is the wavelength.

$$\theta = 2\arcsin\left(0.442\frac{\lambda}{A}\right) \quad (5.9)$$

Six magnets were used in each of the two rows in the example EMAT. Reducing the number of magnets in a row will create broadband generation/reception and increasing the number of magnets in a row will create narrowband generation/reception [56], [204].

Ideally it is better to have more magnets for narrowband generation and reception if the EMAT is to be used at only specific wavelengths, however this will increase the size of the EMAT, as well as the magnetic holding force which then impacts the feasibility for use on a mobile robotic platform. There is existing work which has experimented with varying magnet sizes within a row to vary the wavelength of waves generated [151].

5.4. Validation of Optimisation Model

5.4.1. Magnetisation Validation via Experiment

Experimental comparison to the values output by the numerical model was carried out to validate the coil optimization model. This was done by using the coil dimensions of an existing commercial standard bidirectional PPM racetrack coil EMAT, a Sonemat SHG2541-G, and using the model to define the no. of turns and trace widths for the input dimensions given. The model determined that for the following $C_{length} = 116$ mm, $C_{width} = 41$ mm, $M_{width} = 20$ mm, the optimal trace width was 0.63 mm and the number of turns was 18, this gives the highest magnetization. It was found experimentally that 18 turns was the optimal number and that experiment aligned with the model.

The numerical model outputs a curve of magnetization vs. number of turns for a given set of input parameters, this is a theoretical calculation. To validate the model a number of test PCB coils, not FPCBs, were manufactured, each PCB coil had different trace width values and number of turns (5, 10, 15, 18, 25), 18 turns was used instead of 20. The use of PCB not FPCB was adjusted for in the model. The magnetization values of the PCBs

were then measured experimentally and compared to the values generated by the model, the resultant data is shown in Fig. 50.

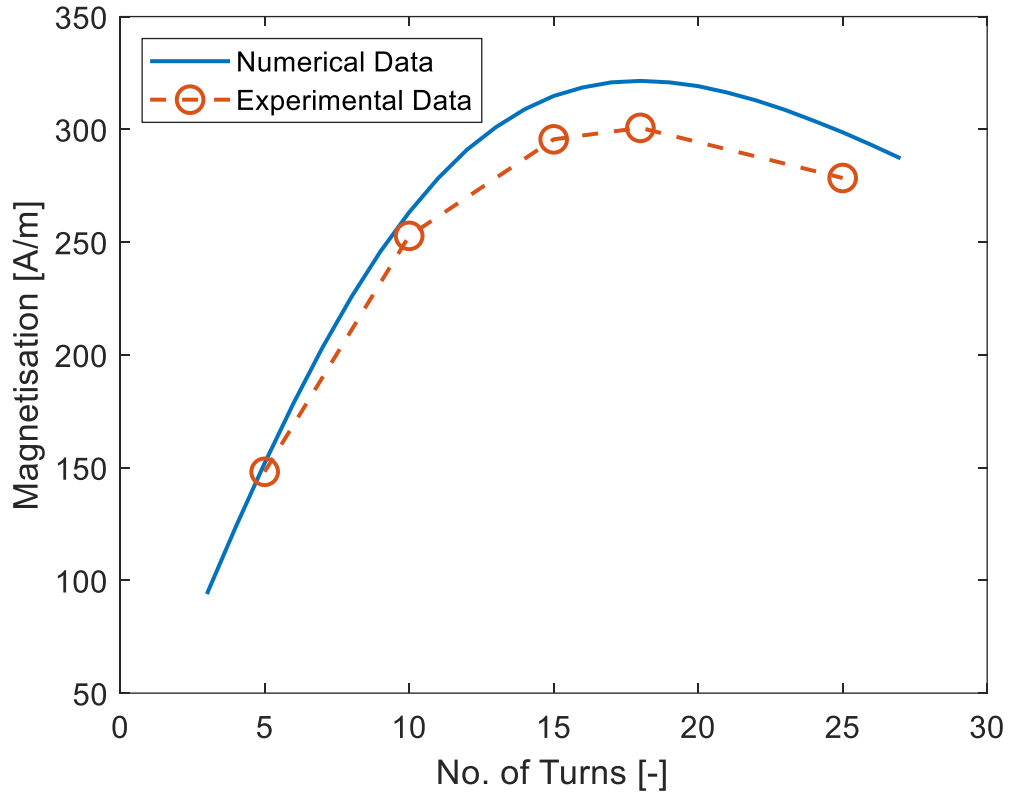


Fig. 50 Numerical model magnetization - no. of turns curve, blue, with the experimental data points for 5, 10, 15, 18 and 25 turns shown, orange.

It can be seen that the experimental magnetization values followed a very similar trend and closely resembled magnetization values of the numerical model, however there is a slight offset which varies depending on the number of turns. The offset was likely due to over etching during the PCB manufacture process. The amount of over etching is typically constant across a run which means that the same amount of copper is removed regardless of trace width, this over etching will have a greater effect on smaller traces than larger

ones which is reflected in the graph, the smaller trace widths see greater proportional increases in resistance which reduces magnetization.

5.4.2. Industrial EMAT Comparison

To further validate and to show the benefits of utilising the coil optimization model, a dimensional replica of the Sonemat SHG2541-G using the numerical model optimised parameters was constructed and compared to the original Sonemat transmitter. The replica transmitter has the same dimensional parameters as the Sonemat transmitter, i.e. C_{length} , C_{width} , M_{width} , but the remaining parameters are the values generated by the numerical model, as well a FPCB racetrack coil was used, instead of a hand wound coil. For the coil dimensions taken from the Sonemat and used to design the replica coil, the optimal number of turns was 23 and the optimal trace width was 0.63 mm, with a copper weight of 2 oz/ft². The magnet array setup for the replica was copied from the Sonemat transmitter and remained unchanged.

To compare the optimized replica and the Sonemat transmitter, both EMATs were placed on a 10 mm steel sample. The transmitters were positioned 300 mm (centre to centre) from a receiver EMAT and pulsed with the same voltage. The same pulsing voltage was used to illustrate the effects of optimising the racetrack coil as the optimised coil will produce higher amplitudes with the same voltage compared to the unoptimized EMAT. The experimental setup used is same as that used in 4.6.2, Fig. 41, a pitch catch setup was used. A LabVIEW (NI Inc., US-TX) programme was used to control the wave generation parameters. The laptop used to run LabVIEW was connected to trigger a PicoScope 5000a (PicoTech, UK) to synchronise with a Ritec RPR-4000 Pulser/Receiver (Ritec, INC, US-

RI), shown in Fig. 51. The Ritec generates a 3-cycle sinusoidal pulse with a reception gain of 50 dB. 0.5 mm lift-off was achieved using PTFE sheets. 10 mm steel plate was used as the sample, which has a density of 7850 kg/m^3 , a measured Longitudinal and Shear velocity of 5959 m/s and 3259 m/s.

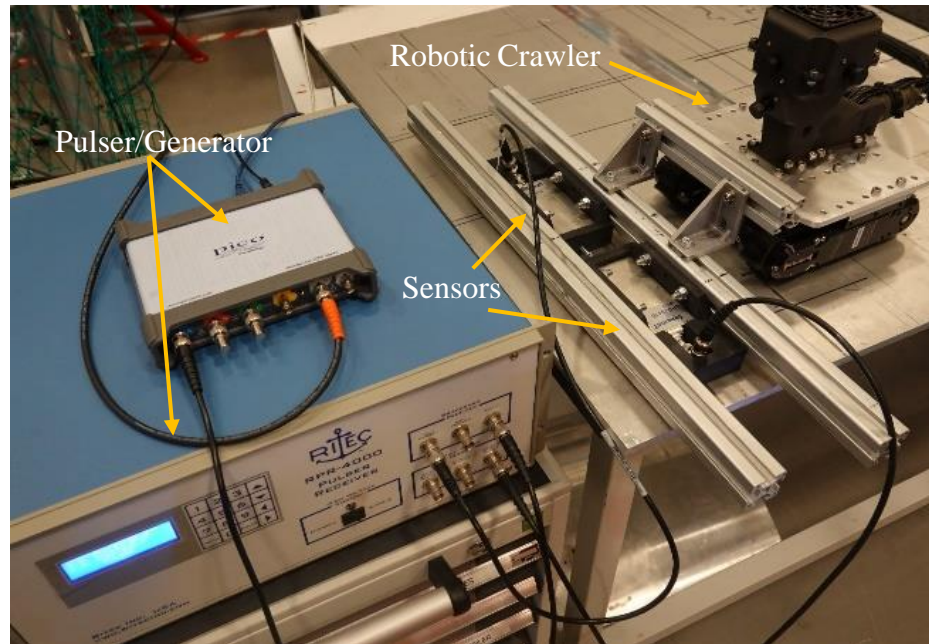


Fig. 51 Experimental Setup, the Ritec pulses the EMATs and receives the resultant signals, the Picoscope is triggered to record this and feeds the information to the LabVIEW program so it can be analysed.

Fig. 52 shows the A-Scans of the signals generated by each transmitter at two frequencies, 128 kHz for SH0 and 205 kHz for SH1, $\lambda = 25 \text{ mm}$. The clear advantages to using the optimised coil can be seen in terms of amplitude and SNR, where there is a two times increase in signal amplitude between the two EMATs in favour of the optimized replica. The replica transmitter had a 6 dB SNR increase over the Sonemat transmitter.

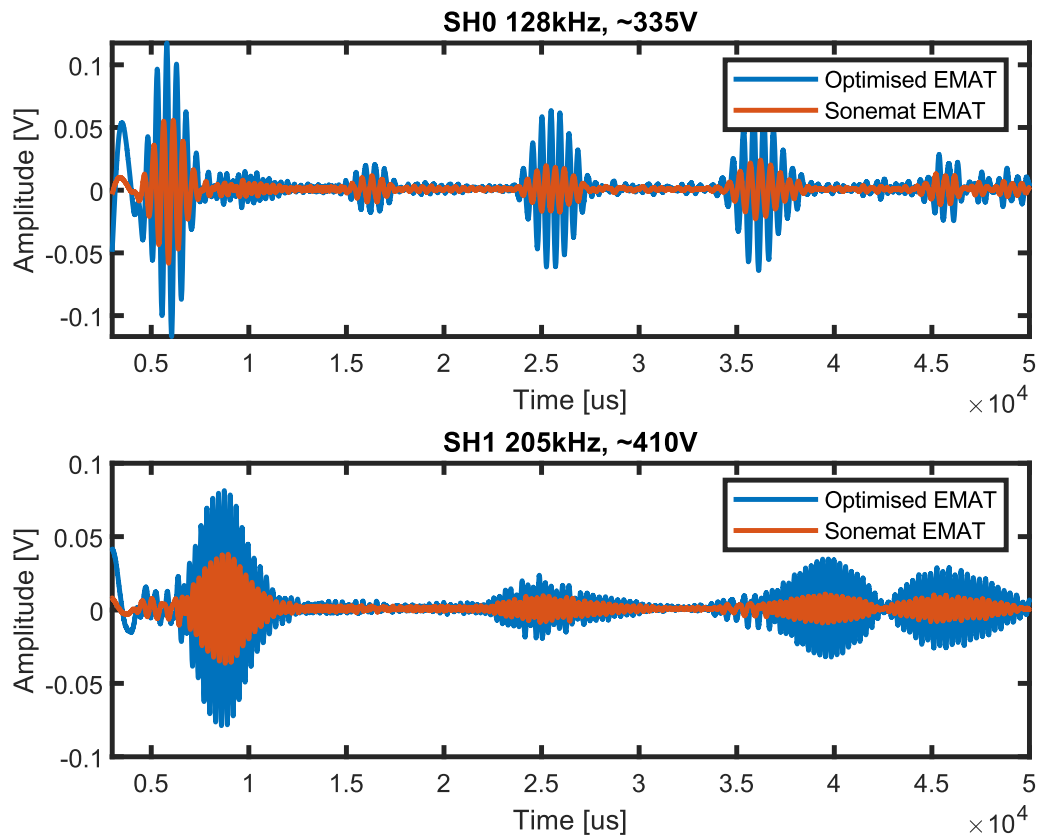


Fig. 52 The top graph shows the A-Scans of each transmitter when generating SH0 and the bottom graph shows the A-Scans for SH1. It can be seen clearly the increase in signal amplitude when using the optimized transmitter.

5.5. Mobile Robotic Transducer Design

5.5.1. Transmitter/Receiver Setup

As discussed a typical mobile robotic setup is a bidirectional transmitter and with two receivers, such as that used in [127], this setup impedes robotic movement due to the size, approx. 30 cm in width, but is necessary due to the bidirectional transmitter which requires two receivers so that relative feature positioning can be established during ranging.

One of the benefits of using a unidirectional EMAT for ranging is that the relative position of a feature can be easily inferred. As waves are only being produced in one direction from the EMAT, there is no confusion around the wave propagation path arising from whether a wave initially travelled from the left or the right side of the transmitter.

The result of using a unidirectional transmitter is that the overall sensor package size can be reduced significantly as there is no need for a second receiver to help determine wave propagation paths. Further to this it was found in testing that the receiver can be placed adjacent to the transmitter and performance remains the same, as electrical saturation subsides before returning signals arrive. When the transmitter emits a pulse, the receiver initially experiences a high level of electrical interference or residual excitation from the transmitted signal. This occurs due to the strong electromagnetic coupling between the transmitter and receiver, temporarily overwhelming the receiver's ability to detect incoming signals. As the setup used is in pitch catch orientation not pulse echo, electrical saturation will only affect the first received direct signal from transmitter to receiver not those reflected from edges and welds. Both factors allow the transmitter and receiver to be mounted in the same housing which greatly reduces the transducer package size, which is highly advantageous for use in mobile robotics. The unidirectional transmitter/receiver setup is shown diagrammatically by Fig. 53.

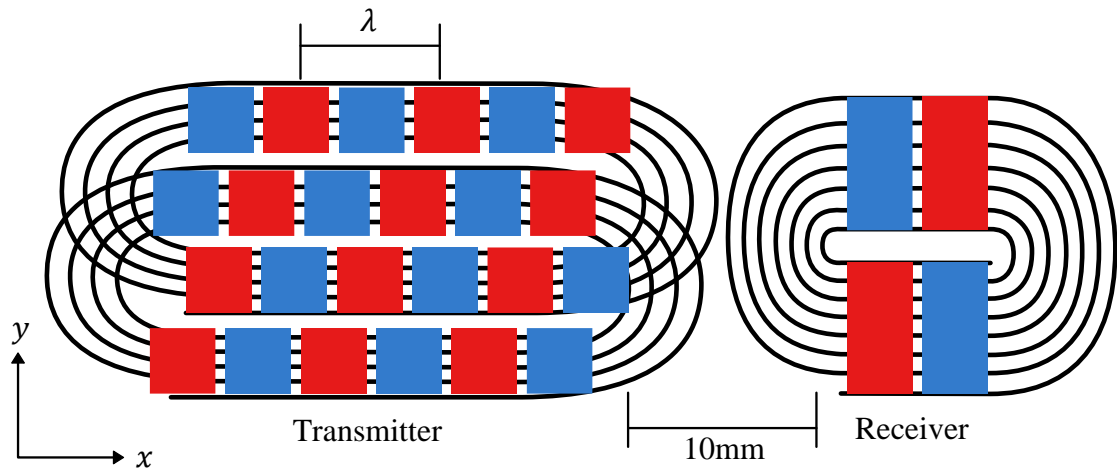


Fig. 53 Diagram showing the magnet and coil arrangement of the unidirectional, reduced receiver setup. 10 x 10 mm magnets were used for the transmitter and 20 x 10 mm magnets were used for the receiver.

5.5.2. Transmitter EMAT Design

A unidirectional PPM EMAT is essentially two standard PPM EMATs overlapped and integrated into each other, the magnet array of the top EMAT is side shifted a quarter wavelength ahead of the bottom EMAT [21], Fig. 54. Each EMAT has a coil which is pulsed separately from the other, the top EMAT coil, I_2 , is pulsed 90° after the bottom coil, I_1 , this causes the two forward propagating waves to constructively interfere and the backward propagating waves to destructively interfere, essentially eliminating the wave propagation on one side [21].

The relative coil and magnet array positioning is critical to effective enhancement and cancelling of the forward and backward propagating waves. If the coil positions and time at which each coil was pulsed were not offset and they were aligned, the coils would behave act like a normal bidirectional transmitter increasing the amplitude of backward and forward propagating waves. If the coils were offset by 180° this would cause full wave

cancellation. If the coil and signal pulse offset was set to 270° the backward propagating wave would be enhanced and the forward propagating wave cancelled out, the opposite of what has been designed. Combinations in between the positions mentioned would result in suboptimal iterations of constructive and destructive interference of the forward and backward propagating waves.

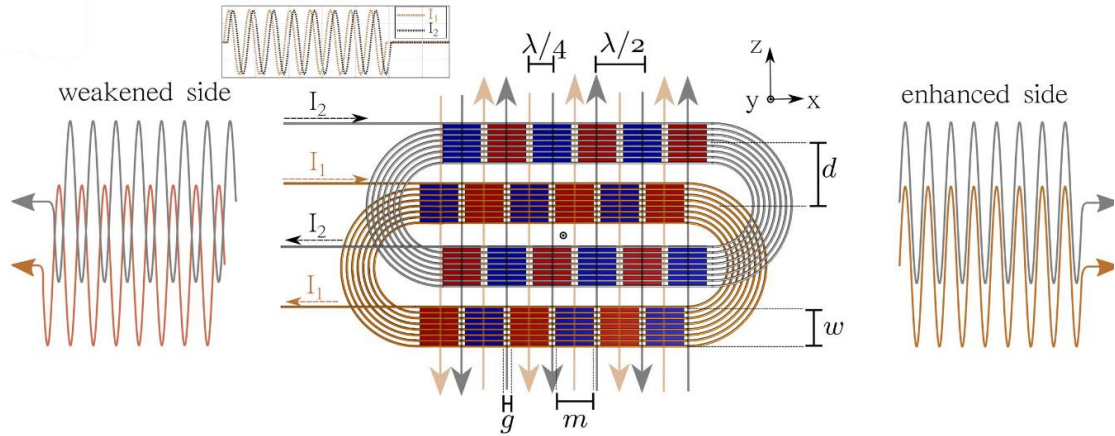


Fig. 54 Unidirectional EMAT schematic showing how the coil and time of pulsing offset creates constructive and destructive interference, adapted from [21].

The unidirectional EMAT designed in this work, Fig. 53 and Fig. 54, was optimised for a 25 mm wavelength to generate SH1 within 10 mm steel plate at 205 kHz. 10 x 10 x 5 mm magnets were used as they allowed space to easily overlap the two racetrack coils and magnet arrays, the magnets were also a commercially available size, 2.5 mm edge to edge spacing was created between the magnets, this means that $w > S/2$ by a small amount, however as there are six rows of magnets, the noise created by increased magnet size is eliminated by narrowband generation.

The FPCB coils were chosen to be manufactured by PCBWay (PCBWay, CN) meaning that the input parameters, $G_{minimum}$, $P_{thickness}$, $T_{minimum}$, W_{Cu} , were set by the

manufacturers limitations. To produce a wave with wavelength of 25 mm and to allow the coils to overlap to form a unidirectional EMAT, the required values for the remaining input parameters are shown in Table 8.

Table 8 – Unidirectional EMAT Coil Parameter Inputs

| Parameter | Value | Parameter | Value |
|------------------|----------------------|------------------|--------------|
| C_{length} | 116 mm | $P_{thickness}$ | 0.25 mm |
| C_{width} | 36 mm | G_{sample} | 0.5 mm |
| M_{width} | 10 mm | V_{in} | 1600 V |
| $G_{minimum}$ | 0.25 mm | Z_{source} | 50 Ω |
| $T_{minimum}$ | 0.25 mm | f | 205 kHz |
| W_{Cu} | 2 oz/ft ² | S_M | Steel |

For the unidirectional transmitter coils, the resultant trace width was 0.354 mm and number of turns were 23, this design was produced on flexible Kapton PCB with a copper weight of 2 oz/ft². Although these coils are designed for a unidirectional PPM EMAT the optimisation method presented still applies, as the coils are pulsed individually and due to the way the PCB assembly is constructed there is no difference between the method of optimisation for this coil and a standard bidirectional coil, only the parameter inputs are different, such as having a significantly larger C_{width} to M_{width} ratio.

5.5.3. Reduced Size Receiver EMAT Design

The receiver coil was designed using the same methodology as the transmitter coils however the coil dimensions were altered to fit across a 2x2 array of 20 x 10 mm magnets. Input parameters for the numerical model were identical except from the following values:

L_{length} - 80 mm, L_{width} - 42 mm, M_{width} - 20 mm. This resulted in a trace width of 0.745 mm with 23 turns, printed onto flexible Kapton PCB with copper weight of 2 oz/ft².

Four magnets were used for the receiver as the decrease in magnetic holding force from using twelve magnets decreases the total magnetic holding force of setup from what was previously used [50]. The transmitter EMAT is a narrowband generator and as such it has been assumed that narrowband reception was not critical, so a reduced number of magnet rows was used for this optimised sensor setup.

5.5.4. Simulation of Unidirectional Transmitter EMAT

5.5.4.1. Simulation Setup

OnScale (OnScale, US-CA) was used to simulate the unidirectional transmitter EMAT design. A 3D model was created where blocks of the same dimensions as the magnets were used as force application areas, for generating the SH wave in the simulated steel plate. The coil and the magnets were not directly simulated in OnScale, but instead Lorentz forces were applied to the surface in the areas where the magnets and coil overlap.

To generate SH1 in a 10 mm plate of mild steel, with density 7850 kg/m³ [187], Longitudinal and Phase velocities were 5959 m/s and 3259 m/s, a 3-cycle 205 kHz sinusoidal pulse was used as the driving signal for all four rows, however the driving signal for rows 1 and 3 were offset by 90°. Mesh size was set to 0.1 mm which is less than $\lambda/20$, [205], so the mesh size is suitably accurate. Measurement points were set on both sides of the force array 10 cm along the x-axis from the centre of the force array, in order to measure the dampened backward waves and the enhanced forward waves.

5.5.4.2. Simulation Results

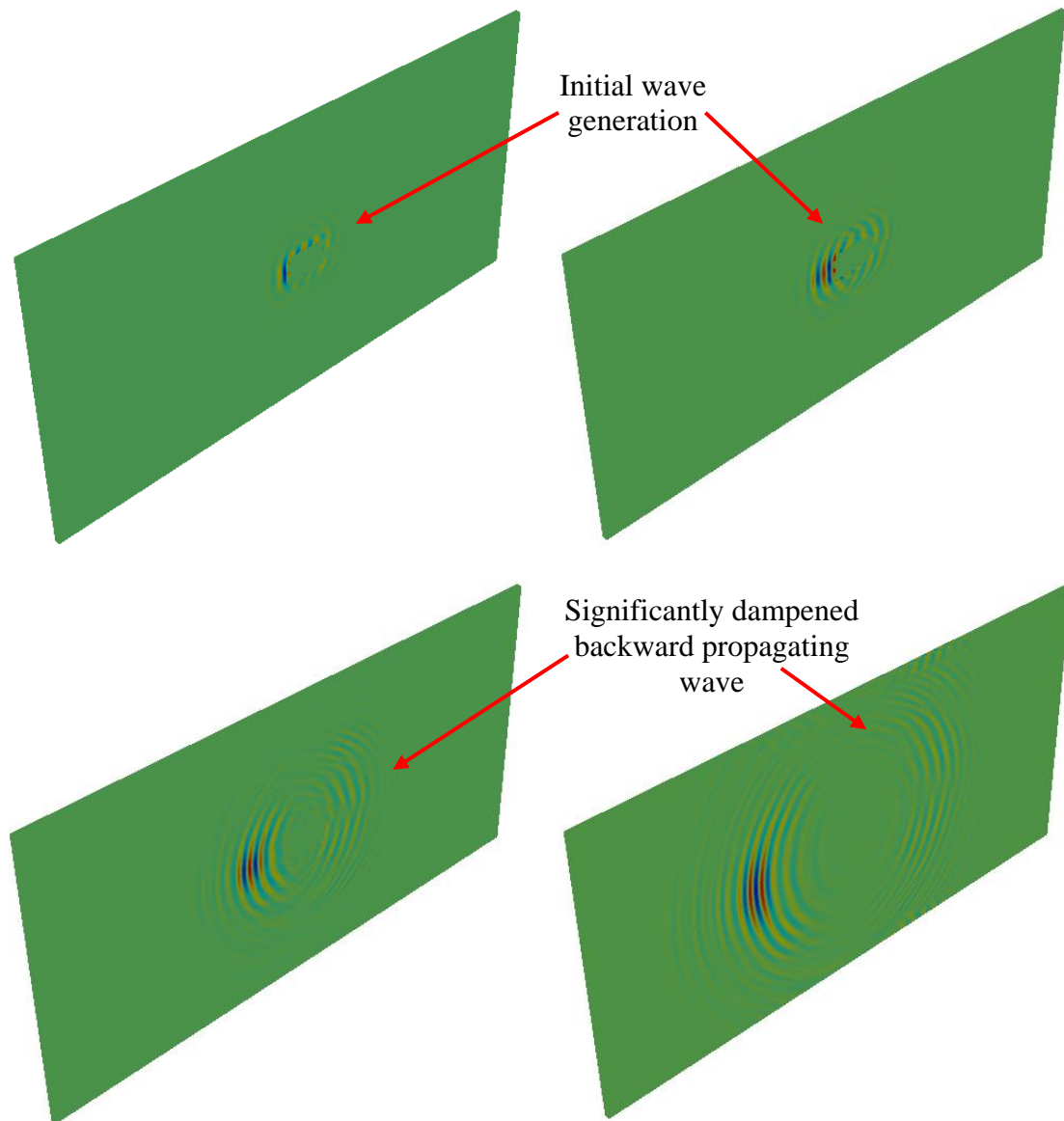


Fig. 55 Multiple stages of single sided wave generation can be seen in the images of the simulation. Initial wave generation can be seen where an enhanced forward propagating wave moving towards the left can be seen. Two significantly dampened side lobe waves can be seen propagating to the right, their amplitudes are less than 0.1 mV which is in the range to be considered noise.

Fig. 55 shows images of a simulation of the unidirectional transmitter. Fig. 56 shows the comparison in amplitude between the forward (constructive interference) and backward

(destructive interference) waves, as desired the backward wave is almost fully eliminated. By comparison to the forward travelling wave, the backward signal is in an amplitude range that could be considered noise, with an amplitude less than 0.1 mV, which will further reduce in amplitude through attenuation. Additionally the majority of this wave propagates as side lobes. As such there is little chance of this wave producing a feature reflection, as the point this small signal is measured is almost next to the point of generation and feature reflection propagation paths are typically longer.

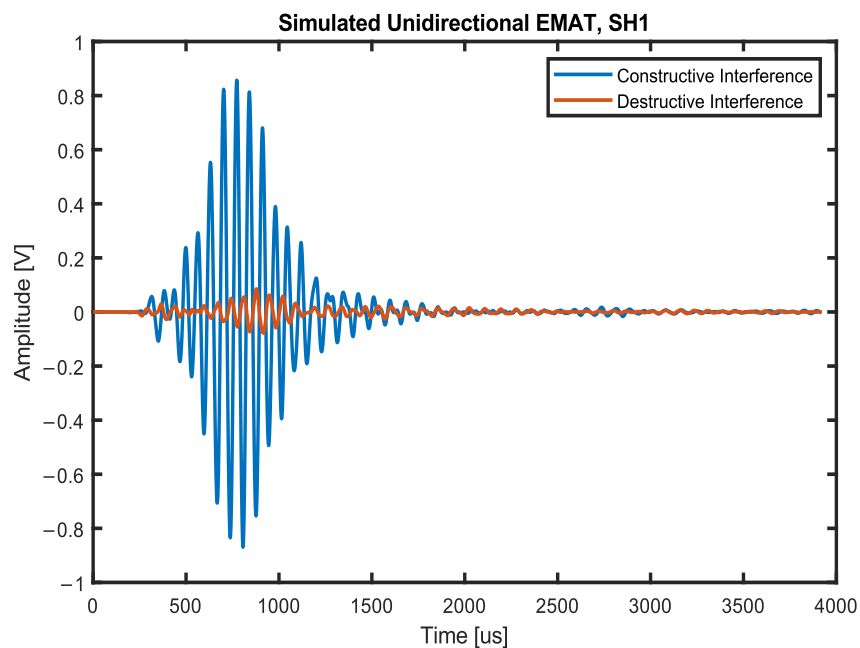


Fig. 56 Signals produced by the simulated unidirectional transmitter, the dampened wave is significantly reduced in size compared to the undampened wave.

5.5.5. Experimental Test of Unidirectional EMAT

5.5.5.1. Experimental Setup

To show that the optimised unidirectional transducer package operated as intended, the transmitter and receiver EMATs were tested experimentally. The transmitter was

validated by taking measurements at either side of the EMAT when pulsing the transmitter, if single sided generation occurred this would be seen where one measurement resemble noise and the other side will show a strongly amplified signal.

Due to equipment limitations, both coils of the unidirectional transmitter could not be pulsed at the same time and had to be pulsed separately. Post processing was then used to phase shift the pulse of one coil by 90° and combine the signals to cause constructive and destructive interference. This also required the receiver to be moved to be in front and behind the receiver to capture the initial pulse of the forwards and backwards waves. The receiver EMAT was placed 10 cm, centre to centre on both sides, from the transmitter, this setup has increased transducer separation compared to the final transducer setup for experimental simplicity.

For evaluating the receiver an SNR comparison to a commercial receiver EMAT was used. The commercial EMAT and the reduced size receiver EMAT were placed 30 cm from the commercial transmitter EMAT. SH waves were sent to the receivers at the same voltage, the SNR of each receiver EMAT was then able to be compared. The experimental equipment setup for both tests was the same as that used in 5.4.2, a pitch catch configuration was used for measurement in both cases. For the unidirectional transmitter test the commercial EMAT, the Sonemat SHD2541-S, was used as the receiver. A Sonemat SHG2541-G, was used as the transmitter for the reduced size receiver test. Both commercial EMATs are designed for a 25 mm wavelength and with a 6 x 2 magnet array made up of 20 x 10 x 5 mm magnets.

5.5.5.2. Transmitter Test Results

The results of the unidirectional transmitter can be seen in Fig. 57, where the amplitude of the forward propagating wave was significantly increased, and the backward propagating wave was dampened greatly.

The backward propagating wave was not fully eliminated, this is thought to be a result of the equipment limitations and subsequent post processing. However, it has still been shown that unidirectional generation has been achieved using this EMAT configuration.

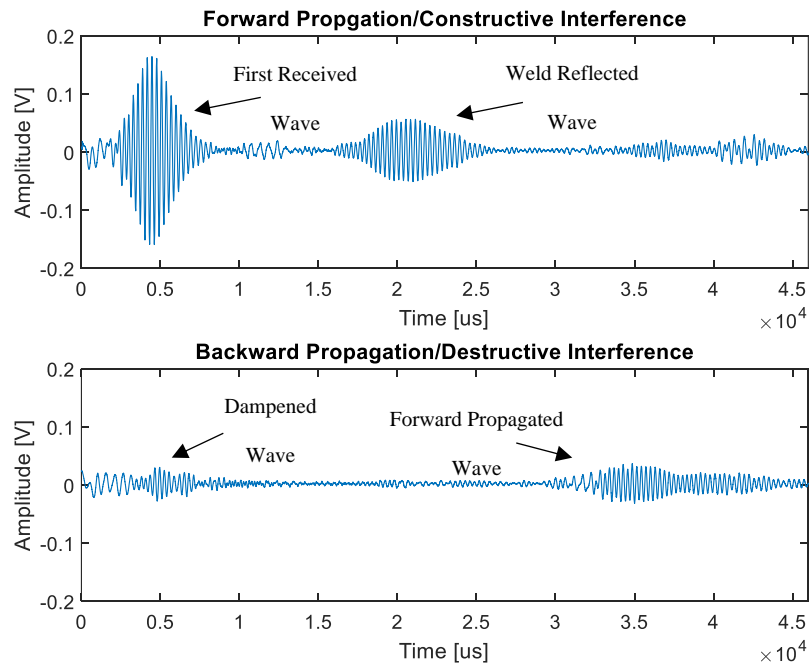


Fig. 57 The forward propagating waves and the backward propagating waves are shown, the difference in amplitude shows unidirectional transmission has been achieved experimentally. The signal at 3.5 μ s in the backward propagating signal is a reflected signal from the forward propagating wave.

5.5.5.3. Receiver Test Results

The SNR of the commercial EMAT receiver was 23.7 dB and the SNR of the reduced size receiver was 19.4 dB. The SNR of the reduced size receiver was expected to be less than the commercial EMAT as the commercial EMAT has four more rows of magnets, which increases its reception capabilities. However, the slight reduction in SNR does not significantly affect the ability to range with the reduced size receiver, as in testing the reflections of edges and welds could still be clearly seen even with the small increase in noise. The reduced magnetic pull force is beneficial for improving compatibility with a mobile robotic system, as such the compromise of a slightly reduced SNR is acceptable.

5.5.6. Transducer Ranging

The use of two receivers solves the issue of determining the wave propagation path when using a bidirectional transmitter. However the performance of this type of setup is not perfect and certain measurement positions within a sample will cause signal interpretation issues. An example of this would be where two features are at the same distance relative to each receiver but in opposite directions, reflecting signals will arrive at the same time at both receivers, which means the path the signal has travelled cannot be interpreted, this means ranging cannot occur as direction is needed. The unidirectional transmitter setup solves this issue as the returning waves are driven from one side of the EMAT, so the initial direction and propagation path is implied for all signals.

Accuracy of ranging is not measured here as in both setups the SH1 wave mode is used so a comparison cannot be made as ranging accuracy is wave mode dependant. Instead,

performance will be measured by evaluating the difficulty of identifying the direction that the signal came from and the coverage given by the number of measurements that can be taken by a transducer setup when moving in 10 cm steps across a test sample. Of the two transducer setups, the better performing setup for ranging and mapping in an unknown environment will be that which has no dead zones of identifying received signal direction and provides increased measurement coverage of the sample.

5.5.6.1. Mapping Performance Setup

To compare the two transducer setups a mapping accuracy test was carried out on 100 x 100 x 1 cm aluminium plate. Aluminium plate was used instead of steel to ease the measurement process as there are no magnetic holding forces making the EMATs significantly easier to position accurately. The bidirectional setup was reduced in size so that both receivers were closer together resulting in a total transducer length of 35 cm. The unidirectional setup had a length of 15 cm, where the unidirectional transmitter and the reduced size receiver were used.

Both setups were tested by mounting them to a robotic crawler and driving the crawler laterally across the sample from one side to the other, moving the transducers and recording the ease of identifying the reflected signal and the certainty of the direction of the signal, Fig. 58. A housing was created for both setups to mount to the robotic crawler and to maintain the same relative transmitter and receiver position(s) during measurement. Starting at the edge of the plate, measurements were taken as many times as possible in 10 cm steps, however due to the different sizes of transducer a different number of measurements were taken for each setup.

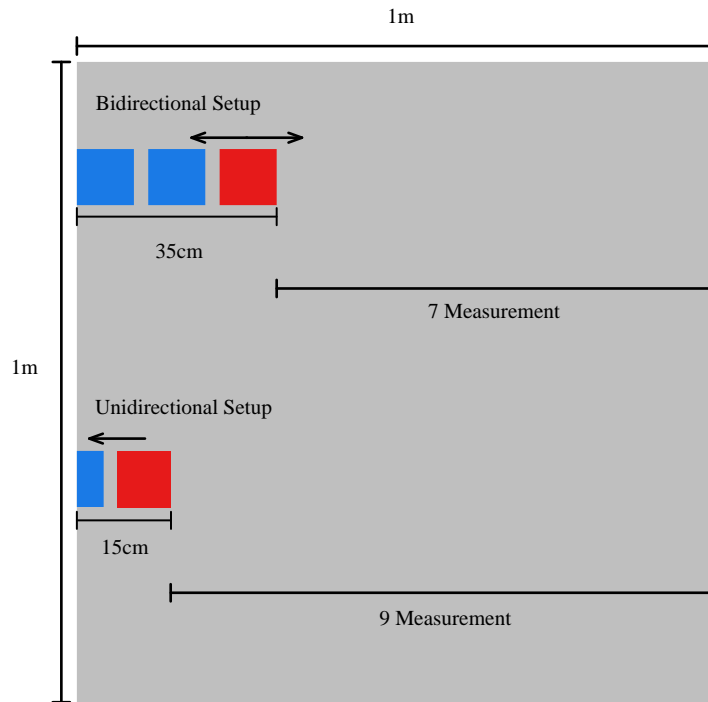


Fig. 58 Ranging test setup and plate, the number of 10 cm steps for each transducer setup is illustrated, the bidirectional transducer setup is 35 cm in length and unidirectional transducer setup is 15 cm. Transmitters are represented by the red squares and receivers by the blue squares. The arrows indicate the directions of wave generation.

5.5.6.2. Mapping Performance Results

Comparing the total number of measurements taken with each setup, extra coverage was achieved within the 1 m plate using the unidirectional configuration. This is beneficial as it increases the amount of subject data available during inspection. There were two positions along the plate where it was difficult to identify an edge reflection using the unidirectional transducer setup. This was the penultimate and final measurement position, where the wave travelled from one end of the plate and back. As a result of the wave travelling this distance, attenuation had a significant effect on the returning signal. However, strong signal attenuation is expected with plate-borne guided waves and in a

typical ranging situation the transducer setup will be able to be easily moved closer to an feature that is initially shown by weak reflections.

For the bidirectional transmitter and two receivers setup, issues were present in this experiment. There were positions where two reflecting signals arrived at the same time to each receiver, and therefore, could not be distinguished, resulting in the direction of propagation not being established. It can be seen in the signals, shown in Fig. 57, that the signal direction of the unidirectional EMAT setup is known and the distance to the edge is calculated. For the signals received by the bidirectional transducer setup, as shown in Fig. 59, the direction that the signals came from cannot be interpreted, and therefore, ranging would not be possible at this position in an unknown environment.

Further to this, there were a number of positions where identification of a given reflecting signal, and the direction of its propagation were difficult to interpret, these additional scans are shown in Fig. 60.

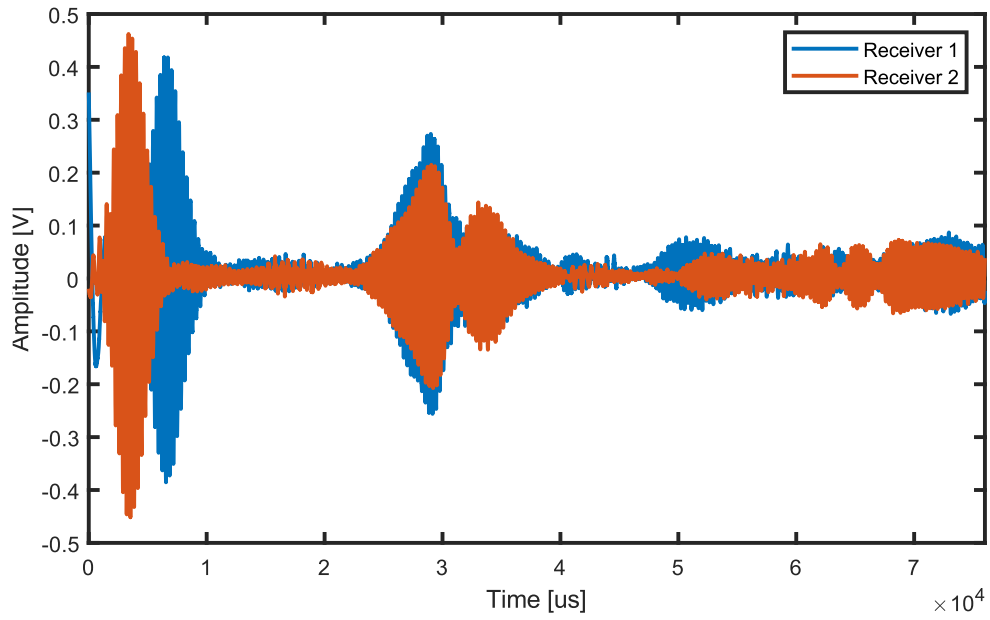


Fig. 59 An example of a point on the plate where the direction of the signals could not be inferred due to the reflecting signals returning back to both receivers at the same time, as indicated by the red lines.

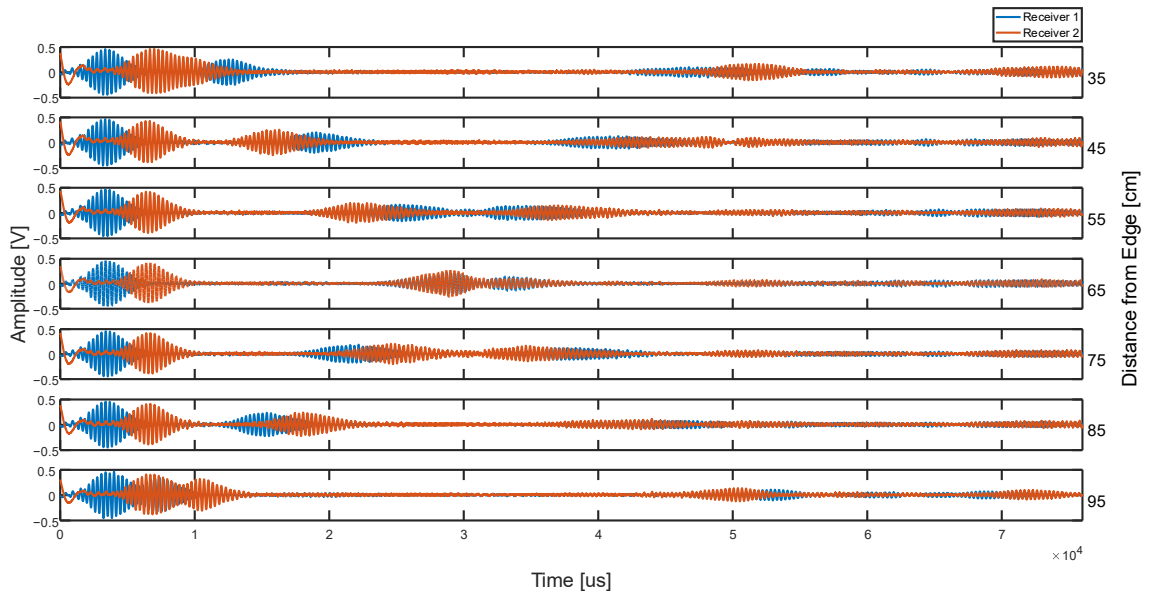


Fig. 60 Shows the entire seven scans taken to further highlight the point on the plate where the two-receiver setup cannot map; this is 65 cm from the plate edge.

5.5.6.3. Magnetic Holding Force

The EMATs used in [127] are traditional commercial PPM EMATs in a pitch catch setup. The magnetic holding force of this setup, one transmitter and two receiver EMATs, on sufficiently thick steel plate with a 0.5mm gap between sensor and sample, is estimated simply below. In this case the transmitter and receivers are Sonemat 6x2 PPM Array EMATs, so the calculation of holding force is identical for all three EMATs. The holding force of a single magnet is given by (5.10) where F_0 is the holding force of a single magnet, B is the surface magnetic flux density, A is the pole face area of a magnet, and μ_0 is the permeability of free space.

$$F_0 = \frac{B^2 A}{2\mu_0} \quad (5.10)$$

As the EMATs are constructed with 20x10mm N52 neodymium magnets [206], the holding force of a single magnet is calculated as approximately 50N. The total force of the array is calculated using equation (5.11), where n is the number of magnets and K is the interaction factor, 1.5 is used for closely packed magnets. The total force of an array is found to be approximately 900N.

$$F_{array} = (N \cdot F_0) \times K \quad (5.11)$$

The exponential decay of the air gap between the sensor and sample is then applied, this is given by equation (5.12), where δ is the decay length set at 1mm. This results in a force of 546N

$$F_{gap} = F_{array} \times e^{-\frac{g}{\delta}} \quad (5.12)$$

This value is then adjusted for flux leakage and magnet repulsion using equation (5.13), $F_{leakage}$ is set at 0.7, $F_{replulsion}$ is set at 0.85.

$$F_{final} = F_{gap} \times F_{leakage} \times F_{replulsion} \quad (5.13)$$

The resultant holding force per sensor is approximately 325N, the total force of one transmitter and two receivers as a setup is approximately 1625N.

The optimised sensor model used a 6x4 PPM array, 10x10mm magnets, for the transmitter and 2x2 PPM array, 20x10mm magnets, for the receiver. Using the same method of calculation the total holding force of the sensor setup was found to be approximately 567N, where the 6x4 array contributed approximately 459N and the 2x2 array contributed approximately 108N. This shows the magnetic holding force can be reduced by 1058N whilst improving signal strength and reducing sensor setup size, improving application to mobile robotic setups.

5.6. Investigation Conclusion

To improve EMAT enabled range finding for use in mobile robot applications, a numerically optimised unidirectional EMAT transmitter and receiver setup was developed to replace the typical bidirectional transmitter, two-receiver setup used for mobile robotic applications [127].

The first improvement was made by increasing the generated Lorentz force by the EMAT to improve the quality of the signal produced at lower voltages. This was achieved by building a numerical model for racetrack coil geometry and parameter optimisation based on the desired input parameters and by creating a guideline for magnet array construction

and design, which was experimentally validated and compared to an existing commercial transmitter. A replica EMAT of a commercial transmitter built using the optimisation methodology produced waves with a 2x increase in signal amplitude over the commercial non-optimised transmitter when pulsed with the same voltage level.

A unidirectional transmitter-based transducer setup was utilised as it has a compact overall size which is more appropriate for mobile robotic applications. The unidirectional transmitter was designed and manufactured using the EMAT optimisation framework along with a reduced size receiver to complete the transducer setup, resulting in an increased signal amplitude with a smaller transducer footprint. This was tested experimentally for proof of concept. The optimised sensor setup reduced the total magnetic holding force by 1058N.

Finally, the optimised transducer setup was compared a typical bi-directional and two receiver setup to highlight the benefits of using the optimised setup for echolocation and ranging in a mobile robotic application. The two setups were compared by their ranging capabilities. Both setups were moved across an aluminium plate and the number of measurement steps, steps were in 10 cm increments, where the direction of the reflected signals could be implied and the reflected edges were easily detectable were counted. The unidirectional setup was able to take more measurements within the defined measurement space due to its reduced size and was able to range effectively at almost all points, becoming ineffective at one point only due to wave mode attenuation. The bidirectional transmitter setup was unable to range at certain points due to the signals returning to the receivers at the same time, so signal direction could not be inferred.

Chapter 6

6. Conclusion

6.1. Thesis Summary

This thesis has presented work contributing to the development of utilising EMAT generated guided waves for echo-location and ranging purposes with a focus on applying the findings to mobile robotic inspection/mapping systems. From a selection of fundamental plate-borne guided waves, the mode best suited for reflecting from welded sections in plate like subjects in order to localise a mobile robot plate was investigated. Following this an EMAT optimisation model was developed to improve the strength of signal generated, this model was utilised to develop mobile robotics specific echo-location/ranging EMAT setup which utilised a unidirectional transmitter.

Chapter 2 briefly introduces the reader to the different methods of NDT, typical subjects that require NDT, and why utilising robotically deployed NDT methods is beneficial to industry. Mobile robotic inspection systems are then explored through presenting a state of the art and discussion of typical robotic localising/mapping methodologies. Mobile robotic ranging/sensing and positioning methods are then presented and a discussion on

why proper localisation and tracking of a robots positioning over time is critical to a successful structural inspection.

Chapter 3 starts with introducing ultrasonic guided waves and EMAT generation of guided waves. Guided wave characteristics such as dispersion, wave modes and energy density distribution are discussed, followed by guided wave inspection methods. General EMAT operation is briefly discussed and the typical styles of EMATs and the type of wave they generate are also discussed. The operational mechanisms of Lorentz force EMATs are discussed in depth where the details of the generation of guided waves and reception are presented.

Chapter 4 focuses on the investigation into evaluating the best suited guided wave mode for echolocation and ranging from welded sections in plate-like structures, such as tankers and vessels; as welded sections are consistent and common features to range from on large industrial structures. In this investigation the best suited mode was found to be the mode which reflects strongly from welded sections at reasonable distances, so that echolocation and ranging can take place. A0, S0, S1, SH0 and SH1 were tested and generated in 10mm steel plate in simulation, the modes were propagated at four weld on plate models with varying geometry and reflection coefficients were measured and calculated. SH0 and SH1 were tested experimentally by propagating the modes at four welded plate samples with the geometry of those used in simulation. SH0 and SH1 were then tested for their ranging capabilities on the same samples. SH1 was found to be the mode that had the highest reflection coefficients in simulation and experiment and had a higher accuracy in ranging through each of the “relative to weld” positions tested.

Chapter 5 presents a numerically optimised unidirectional EMAT transmitter and receiver setup was developed to maximise the amplitude of the waves produced by a given EMAT design. Optimising the racetrack coil and magnet array design doubled the signal amplitude over a commercial transmitter of the same design when pulsed with the same voltage levels. Following this a unidirectional transmitter setup optimised for mobile robotics was developed using the numerical optimisation model and applying this to a unidirectional racetrack coil transmitter and a single reduced size receiver. This sensor setup reduces signal complexity compared to a bi-directional transmitter sensor setup and greatly improves the amplitude of the transmitted waves.

6.2. Thesis Findings

6.2.1. Guided Wave Weld Reflectivity Investigation

Five guided waves modes (A0, S0, S1, SH0 and SH1) were propagated at four different butt weld samples, each sample was 10mm steel. Using a 2DFFT method a reflection coefficient for each mode was calculated, SH1 was found to have the highest reflectivity across each of the samples, as well as the most consistent response to weld size changes. This means that in the context of using guided waves as a sensory input for mapping large ferromagnetic structures, SH1 is the most appropriate mode of choice due its weld reflectivity, meaning the most common feature in a given structure will be detected consistently.

Additionally it was found that a wave mode which is highly weld reflective will likely have an energy density distribution favouring the edges of the plates and will have low mode conversion when encountering weld sections.

6.2.2. Racetrack EMAT Optimisation Methodology and Sensor Setup Optimisation

It is common knowledge that EMATs have poor SNR's compared to inspection methods that utilise contact bulk ultrasound, however there are many advantages to using EMATs that outweigh the reduced SNR performance. An optimisation methodology was developed in order to maximise the SNR of racetrack PCB coil EMATs. This methodology is in two parts, the first is a Lorentz maximisation model where for a given set of racetrack coil size dimensions, the optimal number of turns and race width can be calculated to increase the coil induction which as a result increases the Lorentz force. The second part is the magnet array optimisation methodology where a set of design guidelines are presented to optimise the background magnet force. The two parts of the methodology were then applied by replicating an existing commercial EMAT design and comparing the optimised replicant to the original commercial design. In this comparison it was found that the optimised replicant EMAT produced waves of significantly higher amplitudes with better SNR.

This optimisation model was then used to create a unidirectional EMAT transmitter and single receiver setup for use in the guided wave mobile robotic mapping system. When using a traditional bidirectional transmitter, two receivers are required to accurately

determine the propagation direction of received signal. The optimised unidirectional setup offers clear benefits for ranging/localisation over a bidirectional in a mobile robotic mapping context. The benefits include producing stronger signals for ranging, easing signal interpretation, reducing overall sensor package size, and reducing the total magnetic holding force of the sensor.

6.3. Future Work

Following the selection of the wave mode best suited for ranging via welded structures and development of an optimised sensor setup, this work would continue to be developed as follows.

Ouabi et al. [128] showed that automated mapping of plate like structures could be carried out using Lamb waves generated with an omni-directional piezo-crystal based sensor. This methodology has shown to be able to manage complex signal measurement and analysis to build probability maps with good certainty. Building upon this work, an omni-directional SH EMAT transducer setup could be developed to utilise the benefits of the system presented in [128] and the benefits of using an optimised EMAT and SH1 for localisation and ranging compared to Lamb waves. This omnidirectional sensor would likely require a modified version of the optimisation model presented in this thesis but the same general principles of optimisation would still apply. Seung et al. [154] presented an omnidirectional SH EMAT which offers a good starting point for a sensor design and Guo et al. [153] have presented an omnidirectional EMAT for enhanced generation of A0 modes which offers good insight into the optimisation of omnidirectional EMATs.

Furthermore Tabatabaeipour et al. [207] has begun to explore minimum thickness mapping using a Gaussian process regression model where shear horizontal guided waves (SH0) are used as the input. This work began to explore mapping of corrosion pitting and patch type defects which are commonly found in the structures discussed in this thesis. Using SH modes for defect thickness measurement would complement using SH modes for ranging and mapping by providing more insight into the health of the structure during scanning.

References

- [1] D. Lattanzi and G. Miller, 'Review of Robotic Infrastructure Inspection Systems', *J. Infrastruct. Syst.*, vol. 23, no. 3, p. 04017004, Sep. 2017, doi: 10.1061/(ASCE)IS.1943-555X.0000353.
- [2] A. Shukla and H. Karki, 'A review of robotics in onshore oil-gas industry', in *2013 IEEE International Conference on Mechatronics and Automation*, Aug. 2013, pp. 1153–1160. doi: 10.1109/ICMA.2013.6618077.
- [3] 'Nuclear Power in the United Kingdom |UK Nuclear Energy - World Nuclear Association'. Accessed: Nov. 04, 2023. [Online]. Available: <https://world-nuclear.org/information-library/country-profiles/countries-t-z/united-kingdom.aspx>
- [4] 'United Kingdom Electricity Price - Quote - Chart - Historical Data - News'. Accessed: Nov. 04, 2023. [Online]. Available: <https://tradingeconomics.com/united-kingdom/electricity-price>
- [5] 'Oil storage', PetroWiki. Accessed: Nov. 04, 2023. [Online]. Available: https://petrowiki.spe.org/Oil_storage
- [6] P. Horrocks, D. Mansfield, K. Parker, J. Thomson, T. Atkinson, and J. Worsley, 'Managing Ageing Plant', *HSE Books*, p. 53, Aug. 2010.
- [7] R. Bogue, 'Applications of robotics in test and inspection', *Ind. Robot Int. J.*, vol. 45, no. 2, pp. 169–174, Apr. 2018, doi: 10.1108/IR-01-2018-0012.
- [8] C. P. Marsh, A. Siddique, B. Temple, V. M. Hock, and F. Robb, 'Fury: Robotic In-Situ Inspection/ Condition Assessment System for Underground Storage Tanks'.
- [9] C. Stout and D. Thompson, 'UAV Approaches to Wind Turbine Inspection'.
- [10] D. Zonta, B. Glisic, and S. Adriaenssens, 'Value of information: impact of monitoring on decision-making: VALUE OF INFORMATION: IMPACT OF MONITORING ON DECISION-MAKING', *Struct. Control Health Monit.*, vol. 21, no. 7, pp. 1043–1056, Jul. 2014, doi: 10.1002/stc.1631.
- [11] J. M. Farley, 'BEST PRACTICE IN THE APPLICATION OF NDT – AN UPDATE', *Mitsui BabcockHSE*, p. 6, 2004.
- [12] 'Human factors/ergonomics, health and safety in the workplace'. Accessed: May 13, 2021. [Online]. Available: <https://www.hse.gov.uk/humanfactors/index.htm>
- [13] D. Zhang, R. Watson, C. MacLeod, G. Dobie, W. Galbraith, and G. Pierce, 'Implementation and evaluation of an autonomous airborne ultrasound inspection system', *Nondestruct. Test. Eval.*, vol. 37, no. 1, pp. 1–21, Jan. 2022, doi: 10.1080/10589759.2021.1889546.
- [14] J. Lou *et al.*, 'Field Implementation of Above Water Riser Robotic Inspection Tools - Reducing Safety Risk While Improving Efficiency and Effectiveness', in *Day 1 Mon, May 06, 2019*, Houston, Texas: OTC, Apr. 2019, p. D011S002R007. doi: 10.4043/29651-MS.
- [15] 'RMS 2 Ultrasonic Corrosion Mapping | Eddyfi'. Accessed: May 22, 2020. [Online]. Available: <https://www.eddyfi.com/en/product/rms-2-ultrasonic-corrosion-mapping>

- [16] ‘Pressure Vessels’. Accessed: Apr. 12, 2021. [Online]. Available: <http://mechref.engr.illinois.edu/sol/pressure.html>
- [17] G. Dobie, ‘Ultrasonic Sensor Platforms for Non-Destructive Evaluation’, p. 308.
- [18] J. Szrek, P. Trybała, M. Góralczyk, A. Michalak, B. Ziętek, and R. Zimroz, ‘Accuracy Evaluation of Selected Mobile Inspection Robot Localization Techniques in a GNSS-Denied Environment’, *Sensors*, vol. 21, no. 1, p. 141, Dec. 2020, doi: 10.3390/s21010141.
- [19] G. Punzo *et al.*, ‘Bipartite Guidance, Navigation and Control Architecture for Autonomous Aerial Inspections Under Safety Constraints’, *J. Intell. Robot. Syst.*, vol. 95, no. 3–4, pp. 1049–1061, Sep. 2019, doi: 10.1007/s10846-018-0780-1.
- [20] C. N. MacLeod, R. Summan, G. Dobie, and S. G. Pierce, ‘Quantifying and Improving Laser Range Data When Scanning Industrial Materials’, *IEEE Sens. J.*, vol. 16, no. 22, pp. 7999–8009, Nov. 2016, doi: 10.1109/JSEN.2016.2601822.
- [21] A. C. Kubrusly, L. Kang, and S. Dixon, ‘Unidirectional Shear Horizontal Wave Generation With Side-Shifted Periodic Permanent Magnets Electromagnetic Acoustic Transducer’, *IEEE Trans. Ultrason. Ferroelectr. Freq. Control*, vol. 67, no. 12, pp. 2757–2760, Dec. 2020, doi: 10.1109/TUFFC.2020.3027246.
- [22] A. C. Kubrusly, L. Kang, I. S. Martins, and S. Dixon, ‘Unidirectional Shear Horizontal Wave Generation by Periodic Permanent Magnets Electromagnetic Acoustic Transducer With Dual Linear-Coil Array’, *IEEE Trans. Ultrason. Ferroelectr. Freq. Control*, vol. 68, no. 10, pp. 3135–3142, Oct. 2021, doi: 10.1109/TUFFC.2021.3084201.
- [23] R. McMillan *et al.*, ‘Characterization of EMAT Guided Wave Reflectivity on Welded Structures for use in Ranging’, *IEEE Sens. J.*, pp. 1–1, 2022, doi: 10.1109/JSEN.2022.3179326.
- [24] R. McMillan *et al.*, ‘Design and Manufacture of an Optimised Side-Shifted PPM EMAT Array for Use in Mobile Robotic Localisation’, *Sensors*, vol. 23, no. 4, p. 2012, Feb. 2023, doi: 10.3390/s23042012.
- [25] P. D. Wilcox, ‘LAMB WAVE INSPECTION OF LARGE STRUCTURES USING PERMANENTLY ATTACHED TRANSDUCERS’, p. 223.
- [26] ‘Aboveground tanks: One million gallons or more | Minnesota Pollution Control Agency’. Accessed: Nov. 05, 2023. [Online]. Available: <https://www.pca.state.mn.us/business-with-us/aboveground-tanks-one-million-gallons-or-more>
- [27] ‘Systems’. Accessed: Nov. 05, 2023. [Online]. Available: https://www.zepplin-systems.com/de/en/p/zsd/silo-storage-Z_ZIMSER_P97960_00154/
- [28] ‘Large Water Storage Tanks | Tanks up to 210,000 Gal | WST’. Accessed: Feb. 01, 2025. [Online]. Available: <https://water-storage-tank.com/large-water-tanks/>
- [29] Mark, ‘Understanding Pressure Vessels in the Oil and Gas Industry’, Red River. Accessed: Feb. 01, 2025. [Online]. Available: <https://www.redriver.team/understanding-pressure-vessels-in-the-oil-and-gas-industry-3/>
- [30] L. Jeffus, *Welding Principles and Applications*, 4th ed. Cengage Learning, 1997.

- [31] ‘Different Types Of Welding Joints’, <http://industrial.store.shoppiko.com>. Accessed: Feb. 11, 2025. [Online]. Available: <http://industrial.store.shoppiko.com/blog/article/different-types-of-welding-joints>
- [32] C. M. Fortunko, ‘Ultrasonic Inspection of Weldments with Frequency Scanned SH Waves’, in *1979 Ultrasonics Symposium*, Sep. 1979, pp. 253–258. doi: 10.1109/ULTSYM.1979.197202.
- [33] P. A. Petcher and S. Dixon, ‘Weld defect detection using PPM EMAT generated shear horizontal ultrasound’, *NDT E Int.*, vol. 74, pp. 58–65, Sep. 2015, doi: 10.1016/j.ndteint.2015.05.005.
- [34] J. P. Sargent, ‘Corrosion detection in welded steel plates using Lamb waves’, *Insight - Non-Destr. Test. Cond. Monit.*, vol. 52, no. 11, pp. 609–616, Nov. 2010, doi: 10.1784/insi.2010.52.11.609.
- [35] S. Mech, T. Michaels, J. Emmons, and M. Sugiyama, ‘Development of ultrasonic examination methods for austenitic stainless steel weld inspection’, HEDL-SA-1348, 5059068, Aug. 1977. doi: 10.2172/5059068.
- [36] T. J. Jessop, P. J. Mudge, and J. D. Harrison, *Ultrasonic measurement of weld flaw size*. in Report / National Cooperative Highway Research Program, no. 242. Washington, D.C: Transportation Research Board, National Research Council, 1981.
- [37] S. Halkjær, M. P. Sørensen, and W. D. Kristensen, ‘The propagation of ultrasound in an austenitic weld’, *Ultrasonics*, vol. 38, no. 1–8, pp. 256–261, Mar. 2000, doi: 10.1016/S0041-624X(99)00103-1.
- [38] Z. Fan and M. J. S. Lowe, ‘Elastic waves guided by a welded joint in a plate’, *Proc. R. Soc. Math. Phys. Eng. Sci.*, vol. 465, no. 2107, pp. 2053–2068, Jul. 2009, doi: 10.1098/rspa.2009.0010.
- [39] Z. Fan and M. J. S. Lowe, ‘Interaction of weld-guided waves with defects’, *NDT E Int.*, vol. 47, pp. 124–133, Apr. 2012, doi: 10.1016/j.ndteint.2012.01.001.
- [40] X. Zhang and Z. Xu, ‘Formation mechanism of SH guided wave in weld seam’, *Results Phys.*, vol. 16, p. 102840, Mar. 2020, doi: 10.1016/j.rinp.2019.102840.
- [41] R. Halmshaw, *Non-Destructive Testing*, Second. British Institute of NDT, 2004.
- [42] J. Blitz and G. Simpson, *Ultrasonic Methods of Non-destructive Testing*. Springer Science & Business Media, 1995.
- [43] J. L. Rose, *Ultrasonic Waves in Solid Media*. 2008.
- [44] ‘(1) (PDF) Internal Cracks and Non-Metallic Inclusions as Root Causes of Casting Failure in Sugar Mill Roller Shafts’, ResearchGate. Accessed: Aug. 24, 2020. [Online]. Available: https://www.researchgate.net/publication/334942376_Internal_Cracks_and_Non-Metallic_Inclusions_as_Root_Causes_of_Casting_Failure_in_Sugar_Mill_Roller_Shafts
- [45] K. E. Thomenius, ‘INSTRUMENTATION DESIGN FOR ULTRASONIC IMAGING’, 2009.
- [46] M. Hirao and H. Ogi, *Electromagnetic Acoustic Transducers: Noncontacting Ultrasonic Measurements using EMATs*. in Springer Series in Measurement Science and Technology. Tokyo: Springer Japan, 2017. doi: 10.1007/978-4-431-56036-4.

- [47] R. Ribichini, 'Modelling of Electromagnetic Acoustic Transducers', p. 154.
- [48] N. Ida, *Engineering Electromagnetics*. Cham: Springer International Publishing, 2015. doi: 10.1007/978-3-319-07806-9.
- [49] W. Shi, W. Chen, C. Lu, J. Zhang, Y. Chen, and W. Xu, 'Optimal Design of Spiral Coil EMATs for Improving Their Pulse Compression Effect', *J. Nondestruct. Eval.*, vol. 40, no. 2, p. 38, Jun. 2021, doi: 10.1007/s10921-021-00771-z.
- [50] O. Trushkevych *et al.*, 'Miniaturised SH EMATs for Fast Robotic Screening of Wall Thinning in Steel Plates', *IEEE Sens. J.*, vol. 21, no. 2, pp. 1386–1394, Jan. 2021, doi: 10.1109/JSEN.2020.3021526.
- [51] G. Dobie, W. Galbraith, C. MacLeod, R. Summan, and G. Pierce, 'Synthetic aperture guided wave imaging using a mobile sensor platform', in *2012 IEEE International Ultrasonics Symposium*, Dresden, Germany: IEEE, Oct. 2012, pp. 1905–1908. doi: 10.1109/ULTSYM.2012.0478.
- [52] A. Asokkumar, E. Jasiūnienė, R. Raišutis, and R. J. Kažys, 'Comparison of Ultrasonic Non-Contact Air-Coupled Techniques for Characterization of Impact-Type Defects in Pultruded GFRP Composites', *Materials*, vol. 14, no. 5, p. 1058, Feb. 2021, doi: 10.3390/ma14051058.
- [53] J.-P. Monchalain, 'Laser-Ultrasonics: Principles And Industrial Applications'.
- [54] C. Wei and L. Li, 'Acoustic Emission and Ultrasound Monitoring in Laser Micro/Nanofabrication', in *Handbook of Laser Micro- and Nano-Engineering*, K. Sugioka, Ed., Cham: Springer International Publishing, 2020, pp. 1–24. doi: 10.1007/978-3-319-69537-2_47-1.
- [55] P. Khalili and P. Cawley, 'The choice of ultrasonic inspection method for the detection of corrosion at inaccessible locations', *NDT E Int.*, vol. 99, pp. 80–92, Oct. 2018, doi: 10.1016/j.ndteint.2018.06.003.
- [56] A. C. Kubrusly, M. A. Freitas, J. P. von der Weid, and S. Dixon, 'Interaction of SH guided waves with wall thinning', *NDT E Int.*, vol. 101, pp. 94–103, Jan. 2019, doi: 10.1016/j.ndteint.2018.10.007.
- [57] H. Czichos, Ed., *Handbook of Technical Diagnostics: Fundamentals and Application to Structures and Systems*. Berlin, Heidelberg: Springer Berlin Heidelberg, 2013. doi: 10.1007/978-3-642-25850-3.
- [58] I. Valavanis and D. Kosmopoulos, 'Multiclass defect detection and classification in weld radiographic images using geometric and texture features', *Expert Syst. Appl.*, vol. 37, no. 12, pp. 7606–7614, Dec. 2010, doi: 10.1016/j.eswa.2010.04.082.
- [59] 'New Tech Enables Pipeline NDT on Producing Platforms', *Offshore Engineer Magazine*. Accessed: Nov. 04, 2023. [Online]. Available: <https://www.oedigital.com/news/468080-new-tech-enables-pipeline-ndt-on-producing-platforms>
- [60] C. V. Dodd and W. E. Deeds, 'Analytical Solutions to Eddy-Current Probe-Coil Problems', *J. Appl. Phys.*, vol. 39, no. 6, pp. 2829–2838, May 1968, doi: 10.1063/1.1656680.
- [61] J. Blitz, *Electrical and Magnetic Methods of Non-destructive Testing*. Springer Science & Business Media, 2012.

- [62] ‘Eddy Current Testing’, Tiat Europe B.V. Accessed: Nov. 04, 2023. [Online]. Available: <https://tiat.nl/en/inspections/aerospace-inspections/wervelstroom-onderzoek-2/>
- [63] Q. Luo, X. Fang, L. Liu, C. Yang, and Y. Sun, ‘Automated Visual Defect Detection for Flat Steel Surface: A Survey’, *IEEE Trans. Instrum. Meas.*, vol. 69, no. 3, pp. 626–644, Mar. 2020, doi: 10.1109/TIM.2019.2963555.
- [64] Z. Liu, H. Ukida, P. Ramuhalli, and K. Niel, Eds., *Integrated Imaging and Vision Techniques for Industrial Inspection: Advances and Applications*. in Advances in Computer Vision and Pattern Recognition. London: Springer London, 2015. doi: 10.1007/978-1-4471-6741-9.
- [65] D. Zhang, W. Jackson, G. Dobie, G. West, and C. MacLeod, ‘Structure-from-motion based image unwrapping and stitching for small bore pipe inspections’, *Comput. Ind.*, vol. 139, p. 103664, Aug. 2022, doi: 10.1016/j.compind.2022.103664.
- [66] W. Jackson, G. Dobie, C. MacLeod, G. West, C. Mineo, and L. McDonald, ‘Error Analysis and Calibration for a Novel Pipe Profiling Tool’, *IEEE Sens. J.*, vol. 20, no. 7, pp. 3545–3555, Apr. 2020, doi: 10.1109/JSEN.2019.2960939.
- [67] I. Tsitsimpelis, C. J. Taylor, B. Lennox, and M. J. Joyce, ‘A review of ground-based robotic systems for the characterization of nuclear environments’, *Prog. Nucl. Energy*, vol. 111, pp. 109–124, Mar. 2019, doi: 10.1016/j.pnucene.2018.10.023.
- [68] ‘Scorpion 2 | Eddyfi’. Accessed: Jan. 27, 2020. [Online]. Available: <https://eddyfi.com/en/product/scorpion-2>
- [69] ‘AERIS - Non-Ferrous Vacuum Inspection’, JIREH. Accessed: Nov. 05, 2023. [Online]. Available: <http://www.jireh.com/robotics/aeris/>
- [70] G. R. Inc, ‘Gecko Robotics | Rapid AUT Inspection Service’. Accessed: Nov. 05, 2023. [Online]. Available: <https://resources.geckorobotics.com/rapid-aut-inspection-service>
- [71] ‘High definition remote visual inspection | MaggHD magnetic crawler’. Accessed: Aug. 24, 2020. [Online]. Available: <https://www.eddyfi.com/en/product/magghd>
- [72] W. Jackson *et al.*, ‘Magnetic inspection platform for teleoperated remote inspections of complex geometry: 49th Annual Review of Progress in Quantitative Nondestructive Evaluation (QNDE 2022)’, Aug. 2022.
- [73] ‘NAVIC 2 - Base Crawler’, JIREH. Accessed: Nov. 05, 2023. [Online]. Available: <http://www.jireh.com/products/navic-2-base-crawler/>
- [74] ‘API 635 Tank Inspection - Diakont’. Accessed: Nov. 05, 2023. [Online]. Available: <https://diakont.com/energy-services/api-635-tank-inspection/>
- [75] G. R. Inc, ‘Gecko Robotics | RUG (Rapid Ultrasonic Gridding)’. Accessed: Nov. 05, 2023. [Online]. Available: <https://resources.geckorobotics.com/rapid-ultrasonic-gridding>
- [76] ‘TRIPOD’, JIREH. Accessed: Nov. 05, 2023. [Online]. Available: <http://www.jireh.com/robotics/tripod-robotics/>
- [77] ‘TERAX - Internal Pipe Inspection’, JIREH. Accessed: Nov. 05, 2023. [Online]. Available: <http://www.jireh.com/robotics/terax/>
- [78] ‘SAW Bug’, Phoenix ISL. Accessed: Nov. 05, 2023. [Online]. Available: <https://www.phoenixisl.com/products/saw-bug/>

- [79] ‘AccuTrak’, AUT Solutions. Accessed: Nov. 05, 2023. [Online]. Available: <https://autsolutions.net/ndt-products/automated-ndt-scanners/accutrak/>
- [80] ‘BIKE: Advanced Crawler Robot for Remote Visual Inspection’. Accessed: Nov. 05, 2023. [Online]. Available: <https://www.bakerhughes.com/waygate-technologies/robotic-inspection/bike>
- [81] ‘Altiscan v1.3 - Roboplanet’. Accessed: Nov. 05, 2023. [Online]. Available: <https://www.roboplanet.fr/en/ultrasonic-crawlers/altiscan-v1/>
- [82] ‘SteerROVER | Olympus IMS’. Accessed: Nov. 05, 2023. [Online]. Available: <https://www.olympus-ims.com/en/scanners/steerrover/>
- [83] E. V. D. Leden, ‘Rolling on to Better Tank Inspection Data and Decision Making’. Accessed: Nov. 05, 2023. [Online]. Available: <https://blog.eddyfi.com/en/rolling-on-to-better-tank-inspection-data-and-decision-making>
- [84] ‘Scorpion 2 Ultrasonic Robotic Crawler’, Drumlord Ltd. Accessed: Nov. 05, 2023. [Online]. Available: <https://www.drumlord.co.uk/portfolio/scorpion-2-ultrasonic-robotic-crawler/>
- [85] G. M. Team, ‘Automated Ultrasonic Testing (AUT) Techniques: RUG, PAUT, & Rapid AUT’. Accessed: Oct. 17, 2023. [Online]. Available: <https://blog.geckorobotics.com/rug-rapid-aut-tech-for-automated-ultrasonic-testing-aut>
- [86] P. Goel, S. I. Roumeliotis, and G. S. Sukhatme, ‘Robust localization using relative and absolute position estimates’, in *Proceedings 1999 IEEE/RSJ International Conference on Intelligent Robots and Systems. Human and Environment Friendly Robots with High Intelligence and Emotional Quotients (Cat. No.99CH36289)*, Kyongju, South Korea: IEEE, 1999, pp. 1134–1140. doi: 10.1109/IROS.1999.812832.
- [87] P. Neto, J. N. Pires, and A. P. Moreira, ‘3-D position estimation from inertial sensing: Minimizing the error from the process of double integration of accelerations’, in *IECON 2013 - 39th Annual Conference of the IEEE Industrial Electronics Society*, Vienna, Austria: IEEE, Nov. 2013, pp. 4026–4031. doi: 10.1109/IECON.2013.6699780.
- [88] H. Durrant-Whyte and T. Bailey, ‘Simultaneous localization and mapping: part I’, *IEEE Robot. Autom. Mag.*, vol. 13, no. 2, pp. 99–110, Jun. 2006, doi: 10.1109/MRA.2006.1638022.
- [89] R. Siegwart and I. R. Nourbakhsh, *Introduction to Autonomous Mobile Robots*. MIT Press, 2004.
- [90] M. Mihelj *et al.*, *Robotics*. Cham: Springer International Publishing, 2019. doi: 10.1007/978-3-319-72911-4.
- [91] J. Borenstein, H. R. Everett, L. Feng, and D. Wehe, ‘Mobile Robot Positioning & Sensors and Techniques’.
- [92] J. Borenstein and L. Feng, ‘UMBmark: A Benchmark Test for Measuring Odometry Errors in Mobile Robots’.
- [93] D. Zhang, J. Cao, G. Dobie, and C. MacLeod, ‘A Framework of Using Customized LIDAR to Localize Robot for Nuclear Reactor Inspections’, *IEEE Sens. J.*, vol. 22, no. 6, pp. 5352–5359, Mar. 2022, doi: 10.1109/JSEN.2021.3083478.

- [94] P. Alves, H. Costelha, and C. Neves, 'Localization and navigation of a mobile robot in an office-like environment', in *2013 13th International Conference on Autonomous Robot Systems*, Lisbon, Portugal: IEEE, Apr. 2013, pp. 1–6. doi: 10.1109/Robotica.2013.6623536.
- [95] R. Szewczyk, C. Zieliński, and M. Kaliczyńska, Eds., *Progress in Automation, Robotics and Measuring Techniques: Volume 3 Measuring Techniques and Systems*, vol. 352. in *Advances in Intelligent Systems and Computing*, vol. 352. Cham: Springer International Publishing, 2015. doi: 10.1007/978-3-319-15835-8.
- [96] S. Atiya and G. D. Hager, 'Real-time vision-based robot localization', *IEEE Trans. Robot. Autom.*, vol. 9, no. 6, pp. 785–800, Dec. 1993, doi: 10.1109/70.265922.
- [97] 'Spot', Boston Dynamics. Accessed: Nov. 11, 2023. [Online]. Available: <https://bostondynamics.com/products/spot/>
- [98] M. Simon, 'Your First Look Inside Amazon's Robot Warehouse of Tomorrow', *Wired*. Accessed: Nov. 11, 2023. [Online]. Available: <https://www.wired.com/story/amazon-warehouse-robots/>
- [99] D. P. Paudel, C. Demonceaux, A. Habed, and P. Vasseur, '2D–3D synchronous/asynchronous camera fusion for visual odometry', *Auton. Robots*, vol. 43, no. 1, pp. 21–35, Jan. 2019, doi: 10.1007/s10514-018-9698-5.
- [100] B. Dutton and E. S. Maloney, *Dutton's Navigation & Piloting*. Naval Institute Press, 1978.
- [101] D. M. Helmick, Yang Cheng, and S. I. Roumeliotis, 'Path following using visual odometry for a Mars rover in high-slip environments', in *2004 IEEE Aerospace Conference Proceedings (IEEE Cat. No.04TH8720)*, Big Sky, MT, USA: IEEE, 2004, pp. 772–789. doi: 10.1109/AERO.2004.1367679.
- [102] 'Precise indoor positioning system for industrial applications', Precise ($\pm 2\text{cm}$) Indoor Positioning System - Marvelmind Robotics. Accessed: Nov. 11, 2023. [Online]. Available: <https://marvelmind.com/>
- [103] T. Lee, J. Shin, and D. Cho, 'Position estimation for mobile robot using in-plane 3-axis IMU and active beacon', in *2009 IEEE International Symposium on Industrial Electronics*, Seoul, South Korea: IEEE, Jul. 2009, pp. 1956–1961. doi: 10.1109/ISIE.2009.5214363.
- [104] L. Lou and X. Xu, 'An Approach to Improving Attitude Estimation Using Sensor Fusion for Robot Navigation', *Procedia Eng.*, vol. 15, pp. 5601–5605, 2011, doi: 10.1016/j.proeng.2011.08.1040.
- [105] SeungKeun Cho, JangMyung Lee, and SukChan Shin, 'A dynamic localization algorithm for mobile robots using the iGS system', in *2008 IEEE/ASME International Conference on Advanced Intelligent Mechatronics*, Xian, China: IEEE, Jul. 2008, pp. 734–739. doi: 10.1109/AIM.2008.4601751.
- [106] Y. Liu, N. Noguchi, and K. Ishii, 'Attitude Angle Estimation for Agricultural Robot Navigation Based on Sensor Fusion with a low-cost IMU', *IFAC Proc. Vol.*, vol. 46, no. 4, pp. 130–134, 2013, doi: 10.3182/20130327-3-JP-3017.00031.
- [107] M. Kok, J. D. Hol, and T. B. Schön, 'Using Inertial Sensors for Position and Orientation Estimation', *Found. Trends® Signal Process.*, vol. 11, no. 1–2, pp. 1–153, 2017, doi: 10.1561/20000000094.

- [108] Yun Xiaoping, E. R. Bachmann, and R. B. McGhee, ‘A Simplified Quaternion-Based Algorithm for Orientation Estimation From Earth Gravity and Magnetic Field Measurements’, *IEEE Trans. Instrum. Meas.*, vol. 57, no. 3, pp. 638–650, Mar. 2008, doi: 10.1109/TIM.2007.911646.
- [109] Kai Lingemann, H. Surmann, A. Nuchter, and J. Hertzberg, ‘Indoor and outdoor localization for fast mobile robots’, in *2004 IEEE/RSJ International Conference on Intelligent Robots and Systems (IROS) (IEEE Cat. No.04CH37566)*, Sendai, Japan: IEEE, 2004, pp. 2185–2190. doi: 10.1109/IROS.2004.1389733.
- [110] C. Rizzo, T. Seco, J. Espelosín, F. Lera, and J. L. Villarroel, ‘An alternative approach for robot localization inside pipes using RF spatial fadings’, *Robot. Auton. Syst.*, vol. 136, p. 103702, Feb. 2021, doi: 10.1016/j.robot.2020.103702.
- [111] Jingang Yi, Junjie Zhang, Dezhen Song, and Suhada Jayasuriya, ‘IMU-based localization and slip estimation for skid-steered mobile robots’, in *2007 IEEE/RSJ International Conference on Intelligent Robots and Systems*, San Diego, CA, USA: IEEE, Oct. 2007, pp. 2845–2850. doi: 10.1109/IROS.2007.4399477.
- [112] N. Shalal, T. Low, C. McCarthy, and N. Hancock, ‘Orchard mapping and mobile robot localisation using on-board camera and laser scanner data fusion – Part B: Mapping and localisation’, *Comput. Electron. Agric.*, vol. 119, pp. 267–278, Nov. 2015, doi: 10.1016/j.compag.2015.09.026.
- [113] E. Royer, M. Lhuillier, M. Dhome, and J.-M. Lavest, ‘Monocular Vision for Mobile Robot Localization and Autonomous Navigation’, *Int. J. Comput. Vis.*, vol. 74, no. 3, pp. 237–260, Jul. 2007, doi: 10.1007/s11263-006-0023-y.
- [114] J. Moreau, S. Ambellouis, and Y. Ruichek, ‘Fisheye-Based Method for GPS Localization Improvement in Unknown Semi-Obstructed Areas’, *Sensors*, vol. 17, no. 1, p. 119, Jan. 2017, doi: 10.3390/s17010119.
- [115] M. Kim, O. Kwon, and J. Kim, ‘Vehicle to Infrastructure-Based LiDAR Localization Method for Autonomous Vehicles’, *Electronics*, vol. 12, no. 12, p. 2684, Jun. 2023, doi: 10.3390/electronics12122684.
- [116] H. Hur and H.-S. Ahn, ‘Discrete-Time H_{∞} Filtering for Mobile Robot Localization Using Wireless Sensor Network’, *IEEE Sens. J.*, vol. 13, no. 1, pp. 245–252, Jan. 2013, doi: 10.1109/JSEN.2012.2213337.
- [117] ‘Sensor breakdown: how robot vacuums navigate’. Accessed: Jun. 16, 2024. [Online]. Available: <https://www.therobotreport.com/sensor-breakdown-how-robot-vacuums-navigate-and-clean/>
- [118] ‘Roomba® 976 Robot Vacuum | iRobot’. Accessed: Jun. 16, 2024. [Online]. Available: https://www.irobot.co.uk/en_GB/irobot-roomba-976/R976040.html?lang=en_GB&cgid=uk
- [119] S. Shibusawa, ‘Precision Farming Approaches for Small Scale Farms’, *IFAC Proc. Vol.*, vol. 34, pp. 22–27, Aug. 2001, doi: 10.1016/S1474-6670(17)34099-5.
- [120] ‘How Amazon deploys robots in its operations facilities’. Accessed: Jun. 16, 2024. [Online]. Available: <https://www.aboutamazon.com/news/operations/how-amazon-deploys-robots-in-its-operations-facilities>
- [121] ‘Proteus is Amazon’s first fully autonomous warehouse robot’. Accessed: Jun. 16, 2024. [Online]. Available: <https://www.engadget.com/proteus-amazon-first-fully-autonomous-warehouse-robot-074341277.html?guccounter=2>

- [122] S. Thrun, W. Burgard, and D. Fox, *Probabilistic Robotics*, 1st ed. The MIT Press, 2006.
- [123] N. Sünderhauf, ‘Robust Optimization for Simultaneous Localization and Mapping’.
- [124] A. A. Makarenko, S. B. Williams, F. Bourgault, and H. F. Durrant-Whyte, ‘An experiment in integrated exploration’, in *IEEE/RSJ International Conference on Intelligent Robots and System*, Lausanne, Switzerland: IEEE, 2002, pp. 534–539. doi: 10.1109/IRDS.2002.1041445.
- [125] T. Bailey and H. Durrant-Whyte, ‘Simultaneous localization and mapping (SLAM): part II’, *IEEE Robot. Autom. Mag.*, vol. 13, no. 3, pp. 108–117, Sep. 2006, doi: 10.1109/MRA.2006.1678144.
- [126] C. Stachniss, D. Hähnel, W. Burgard, and G. Grisetti, ‘On actively closing loops in grid-based FastSLAM’, *Adv. Robot.*, vol. 19, no. 10, pp. 1059–1079, Jan. 2005, doi: 10.1163/156855305774662181.
- [127] M. Tabatabaeipour *et al.*, ‘Application of ultrasonic guided waves to robotic occupancy grid mapping’, *Mech. Syst. Signal Process.*, vol. 163, p. 108151, Jan. 2022, doi: 10.1016/j.ymsp.2021.108151.
- [128] O.-L. Ouabi *et al.*, ‘Combined Grid and Feature-based Mapping of Metal Structures with Ultrasonic Guided Waves’, in *2022 International Conference on Robotics and Automation (ICRA)*, May 2022, pp. 5056–5062. doi: 10.1109/ICRA46639.2022.9811581.
- [129] L. Bjørnø, ‘Forty years of nonlinear ultrasound’, *Ultrasonics*, vol. 40, no. 1–8, pp. 11–17, May 2002, doi: 10.1016/S0041-624X(02)00084-7.
- [130] B. A. Auld, *Acoustic fields and waves in solids*. Рипол Классик, 1973.
- [131] J. D. Achenbach, *Wave Propagation in Elastic Solids*. North-Holland Publishing Company, 1975.
- [132] H. Lamb, ‘On waves in an elastic plate’, Jul. 1916.
- [133] S. Palanisamy, ‘Ultrasonic Inspection of Gas Porosity Defects in Aluminium Die Castings’.
- [134] M. J. S. Lowe, ‘Matrix techniques for modeling ultrasonic waves in multilayered media’, *IEEE Trans. Ultrason. Ferroelectr. Freq. Control*, vol. 42, no. 4, pp. 525–542, Jul. 1995, doi: 10.1109/58.393096.
- [135] M. Castaings and B. Hosten, ‘Delta operator technique to improve the Thomson–Haskell-method stability for propagation in multilayered anisotropic absorbing plates’, *J. Acoust. Soc. Am.*, vol. 95, no. 4, pp. 1931–1941, Apr. 1994, doi: 10.1121/1.408707.
- [136] B. Hosten and M. Castaings, ‘Transfer matrix of multilayered absorbing and anisotropic media. Measurements and simulations of ultrasonic wave propagation through composite materials’, *J. Acoust. Soc. Am.*, vol. 94, no. 3, pp. 1488–1495, Sep. 1993, doi: 10.1121/1.408152.
- [137] P. M. Morse and H. Feshbach, *Methods of Theoretical Physics*. McGraw-Hill, 1953.
- [138] J. L. Rose, *Ultrasonic Guided Waves in Solid Media*. New York: Cambridge University Press, 2014. doi: 10.1017/CBO9781107273610.
- [139] J. Rose, ‘An Introduction to Ultrasonic Guided Waves’, *4th Middle East NDT Conf. Exhib.*, p. 18, Dec. 2007.

- [140] B. Hernandez Crespo, C. Courtney, and B. Engineer, 'Calculation of Guided Wave Dispersion Characteristics Using a Three-Transducer Measurement System', *Appl. Sci.*, vol. 8, no. 8, p. 1253, Jul. 2018, doi: 10.3390/app8081253.
- [141] D. N. Alleyne and P. Cawley, 'A 2-dimensional Fourier transform method for the quantitative measurement of Lamb modes', in *IEEE Symposium on Ultrasonics*, Dec. 1990, pp. 1143–1146 vol.2. doi: 10.1109/ULTSYM.1990.171541.
- [142] S. Fateri, 'Advanced Signal Processing Techniques for Multimodal Ultrasonic Guided Wave Response', 2015, *Unpublished*. doi: 10.13140/RG.2.1.3911.6881.
- [143] R. Jafari-Shapoorabadi, A. Konrad, and A. N. Sinclair, 'The governing electrodynamic equations of electromagnetic acoustic transducers', *J. Appl. Phys.*, vol. 97, no. 10, p. 10E102, May 2005, doi: 10.1063/1.1851393.
- [144] S. Liu, K. Chai, C. Zhang, L. Jin, and Q. Yang, 'Electromagnetic Acoustic Detection of Steel Plate Defects Based on High-Energy Pulse Excitation', *Appl. Sci.*, vol. 10, no. 16, p. 5534, Aug. 2020, doi: 10.3390/app10165534.
- [145] I. Baillie, P. Griffith, X. Jian, and S. Dixon, 'Implementing an ultrasonic inspection system to find surface and internal defects in hot moving steel using EMATs', vol. 49, no. 2, p. 6, 2007.
- [146] H.-J. Salzburger, G. Dobmann, and H. Mohrbacher, 'Quality control of laser welds of tailored blanks using guided waves and EMATs', *IEE Proc. - Sci. Meas. Technol.*, vol. 148, no. 4, pp. 143–148, Jul. 2001, doi: 10.1049/ip-smt:20010534.
- [147] X. Jia, Q. Ouyang, and X. Zhang, 'An Improved Design of the Spiral-Coil EMAT for Enhancing the Signal Amplitude', *Sensors*, vol. 17, no. 5, p. 1106, May 2017, doi: 10.3390/s17051106.
- [148] W. Zhang, Y. Wu, Y. Wu, and Z. Cai, 'An improved design of lamb wave EMAT for A0 wave generation and enhancement', *Jpn. J. Appl. Phys.*, vol. 60, no. 3, p. 036501, Mar. 2021, doi: 10.35848/1347-4065/abe641.
- [149] M. Chen, Q. Huan, Z. Su, and F. Li, 'A tunable bidirectional SH wave transducer based on antiparallel thickness-shear (d15) piezoelectric strips', *Ultrasonics*, vol. 98, pp. 35–50, Sep. 2019, doi: 10.1016/j.ultras.2019.06.001.
- [150] H. Sun, L. Peng, S. Wang, Q. Wang, W. Zhao, and S. Huang, 'Effective Focal Area Dimension Optimization of Shear Horizontal Point-Focusing EMAT Using Orthogonal Test Method', *IEEE Trans. Instrum. Meas.*, vol. 70, pp. 1–8, 2021, doi: 10.1109/TIM.2021.3073713.
- [151] N. Suresh and K. Balasubramaniam, 'Quantifying the lowest remnant thickness using a novel broadband wavelength and frequency EMAT utilizing the cut-off property of guided waves', *NDT E Int.*, vol. 116, p. 102313, Dec. 2020, doi: 10.1016/j.ndteint.2020.102313.
- [152] A. Thon, G. Painchaud-April, A. Le Duff, and P. Bélanger, 'Optimization of a Lorentz forces EMAT for the reconstruction of the circumferential thickness profile of a steel pipe using high order shear horizontal modes', *NDT E Int.*, vol. 128, p. 102631, Jun. 2022, doi: 10.1016/j.ndteint.2022.102631.
- [153] X. Guo, J. Lin, Z. Hu, and Y. Xiang, 'An Omnidirectional EMAT Employing Spiral Coil and Annular Magnets for Enhanced Generation of A0 Mode Lamb Wave', in *2023 2nd International Symposium on Sensor Technology and Control (ISSTC)*,

- Hangzhou, China: IEEE, Aug. 2023, pp. 89–94. doi: 10.1109/ISSTC59603.2023.10281179.
- [154] H. M. Seung, C. I. Park, and Y. Y. Kim, ‘An omnidirectional shear-horizontal guided wave EMAT for a metallic plate’, *Ultrasonics*, vol. 69, pp. 58–66, Jul. 2016, doi: 10.1016/j.ultras.2016.03.011.
- [155] K. Toda and Y. Shinoda, ‘A unidirectional transducer with three electrode groups for Lamb-wave devices’, *J. Acoust. Soc. Am.*, vol. 63, no. 2, pp. 614–617, Feb. 1978, doi: 10.1121/1.381761.
- [156] Shujuan Wang, Riliang Su, Xiaoyang Chen, Lei Kang, and Guofu Zhai, ‘Numerical and experimental analysis of unidirectional meander-line coil electromagnetic acoustic transducers’, *IEEE Trans. Ultrason. Ferroelectr. Freq. Control*, vol. 60, no. 12, pp. 2657–2664, Dec. 2013, doi: 10.1109/TUFFC.2013.2864.
- [157] K. Rieger, D. Erni, and D. Rueter, ‘Unidirectional emission and detection of Lamb waves based on a powerful and compact coils-only EMAT’, *NDT E Int.*, vol. 122, p. 102492, Sep. 2021, doi: 10.1016/j.ndteint.2021.102492.
- [158] L. M. Martinho, A. C. Kubrusly, L. Kang, and S. Dixon, ‘Enhancement of the Unidirectional Radiation Pattern of Shear Horizontal Ultrasonic Waves Generated by Side-Shifted Periodic Permanent Magnets Electromagnetic Acoustic Transducers with Multiple Rows of Magnets’, *IEEE Sens. J.*, pp. 1–1, 2022, doi: 10.1109/JSEN.2022.3156849.
- [159] S. L. Huang, H. Y. Sun, Q. Wang, S. Wang, and W. Zhao, ‘Unidirectional focusing of horizontally polarized shear elastic waves electromagnetic acoustic transducers for plate inspection’, *J. Appl. Phys.*, vol. 125, no. 16, p. 164504, Apr. 2019, doi: 10.1063/1.5078776.
- [160] R. M. Bozorth, ‘The Physical Basis of Ferromagnetism’, *Bell Syst. Tech. J.*, vol. 19, no. 1, pp. 1–39, Jan. 1940, doi: 10.1002/j.1538-7305.1940.tb03129.x.
- [161] K. Kawashima, ‘Theory and numerical calculation of the acoustic field produced in metal by an electromagnetic ultrasonic transducer’, *J. Acoust. Soc. Am.*, vol. 60, no. 5, pp. 1089–1099, Nov. 1976, doi: 10.1121/1.381208.
- [162] S. S. Udpa, ‘Nondestructive Testing Handbook, third edition: Volume 5, Electromagnetic Testing’, vol. 5.
- [163] R. B. Thompson, ‘A model for the electromagnetic generation of ultrasonic guided waves in ferromagnetic metal polycrystals’, *IEEE Trans. Sonics Ultrason.*, vol. 25, no. 1, pp. 7–15, Jan. 1978, doi: 10.1109/T-SU.1978.30979.
- [164] B. Y. A. S.S. Lee, ‘EMAT Application at High Temperature’, *Nondestruct. Test. Eval.*, vol. 7, pp. 1–6, Jun. 1992, doi: 10.1080/10589759208953004.
- [165] R. Ribichini, F. Cegla, P. B. Nagy, and P. Cawley, ‘Experimental and numerical evaluation of electromagnetic acoustic transducer performance on steel materials’, *NDT E Int.*, vol. 45, no. 1, pp. 32–38, Jan. 2012, doi: 10.1016/j.ndteint.2011.08.007.
- [166] X. Chen, A. Cobb, and S. Vinogradov, ‘Corrosion Detection in Storage Tank Bottoms via Omni-Directional Magnetostrictive Guided Wave Inspection System’, in *2022 49th Annual Review of Progress in Quantitative Nondestructive Evaluation*, San Diego, California: American Society of Mechanical Engineers, Jul. 2023, p. V001T07A008. doi: 10.1115/QNDE2022-98728.

- [167] S. B. Palmer and S. Dixon, 'Industrially viable non-contact ultrasound', *Insight - Non-Destr. Test. Cond. Monit.*, vol. 45, no. 3, pp. 211–217, Mar. 2003, doi: 10.1784/insi.45.3.211.53154.
- [168] S.-K. Yang, P. H. Lee, J.-W. Cheng, and C.-H. Tseng, 'The Study of Wave Propagation through Plates Welded Joints Using Guided Waves SH0 Mode', *15th Asia Pac. Conf. Non-Destr. Test. APCNDT2017 Singap.*, p. 10, 2017.
- [169] J. P. Sargent, 'Corrosion detection in welds and heat-affected zones using ultrasonic Lamb waves', *Insight - Non-Destr. Test. Cond. Monit.*, vol. 48, no. 3, pp. 160–167, Mar. 2006, doi: 10.1784/insi.2006.48.3.160.
- [170] C. Ye, Y. Zhou, V. V. B. Reddy, A. Mebane, and I. C. Ume, 'Welding induced residual stress evaluation using laser-generated Rayleigh waves', presented at the 44TH ANNUAL REVIEW OF PROGRESS IN QUANTITATIVE NONDESTRUCTIVE EVALUATION, VOLUME 37, Provo, Utah, USA, 2018, p. 180003. doi: 10.1063/1.5031632.
- [171] L. J. Bond and J. Taylor, 'Interaction of Rayleigh waves with a rib attached to a plate', *Ultrasonics*, vol. 29, no. 6, pp. 451–458, Nov. 1991, doi: 10.1016/0041-624X(91)90075-J.
- [172] X. Jian, S. Dixon, N. Guo, and R. Edwards, 'Rayleigh wave interaction with surface-breaking cracks', *J. Appl. Phys.*, vol. 101, no. 6, p. 064906, Mar. 2007, doi: 10.1063/1.2435803.
- [173] I. Hajro and D. Hodzic, 'Basic Comparison of Selected Structural Steel Strength Influence On Total Welding Fabrication Costs of Oil Storage Tanks', *Trends Dev. Mach. Assoc. Technol.*, p. 4, 2008.
- [174] L. Kumar, K. U. Yazar, and S. Pramanik, 'Effect of fusion and friction stir welding techniques on the microstructure, crystallographic texture and mechanical properties of mild steel', *Mater. Sci. Eng. A*, vol. 754, pp. 400–410, Apr. 2019, doi: 10.1016/j.msea.2019.03.100.
- [175] J. Zhang, Y. Song, X. Li, and C. Zhong, 'Comparison of Experimental Measurements of Material Grain Size Using Ultrasound', *J. Nondestruct. Eval.*, vol. 39, no. 2, p. 30, Jun. 2020, doi: 10.1007/s10921-020-00675-4.
- [176] Y. Cho, 'Estimation of ultrasonic guided wave mode conversion in a plate with thickness variation', *IEEE Trans. Ultrason. Ferroelectr. Freq. Control*, vol. 47, no. 3, pp. 591–603, May 2000, doi: 10.1109/58.842046.
- [177] Y. H. Cho, W. D. Oh, and J. H. Lee, 'A Wall Thinning Detection and Quantification Based on Guided Wave Mode Conversion Features', *Key Eng. Mater.*, vol. 321–323, pp. 795–798, Oct. 2006, doi: 10.4028/www.scientific.net/KEM.321-323.795.
- [178] S. A. Uribe, N. Nakamura, H. Ogi, M. Hirao, D. O. Thompson, and D. E. Chimenti, 'MODE CONVERSION OF SH GUIDED WAVES AT DEFECTS FOR PIPELINE INSPECTION', in *AIP Conference Proceedings*, Chicago (Illinois): AIP, 2009, pp. 1550–1557. doi: 10.1063/1.3114142.
- [179] M. J. S. Lowe, D. N. Alleyne, and P. Cawley, 'The Mode Conversion of a Guided Wave by a Part-Circumferential Notch in a Pipe', *J. Appl. Mech.*, vol. 65, no. 3, pp. 649–656, Sep. 1998, doi: 10.1115/1.2789107.
- [180] P. Wilcox *et al.*, 'Guided wave testing of rail', *Insight - Non-Destr. Test. Cond. Monit.*, vol. 45, no. 6, pp. 413–420, Jun. 2003, doi: 10.1784/insi.45.6.413.52892.

- [181] F. Kauffmann, T. Klein, A. Klenk, and K. Maile, 'Creep behavior and in-depth microstructural characterization of dissimilar joints', *Sci. Technol. Adv. Mater.*, vol. 14, no. 1, p. 014203, Mar. 2013, doi: 10.1088/1468-6996/14/1/014203.
- [182] C. M. Fortunko, 'Ultrasonic evaluation of austenitic stainless steel welds using shear horizontal waves', *Appl. Phys. Lett.*, vol. 39, no. 9, pp. 699–700, Nov. 1981, doi: 10.1063/1.92853.
- [183] S. M. Tabatabaeipour and F. Honarvar, 'A comparative evaluation of ultrasonic testing of AISI 316L welds made by shielded metal arc welding and gas tungsten arc welding processes', *J. Mater. Process. Technol.*, vol. 210, no. 8, pp. 1043–1050, Jun. 2010, doi: 10.1016/j.jmatprotec.2010.02.013.
- [184] M. Kogia *et al.*, 'Electromagnetic Acoustic Transducers Applied to High Temperature Plates for Potential Use in the Solar Thermal Industry', *Appl. Sci.*, vol. 5, no. 4, pp. 1715–1734, Dec. 2015, doi: 10.3390/app5041715.
- [185] K. Mirkhani *et al.*, 'Optimal design of EMAT transmitters', *NDT E Int.*, vol. 37, no. 3, pp. 181–193, Apr. 2004, doi: 10.1016/j.ndteint.2003.09.005.
- [186] S. A. Ghorashi, F. Honarvar, and M. Tabatabaeipour, 'Automated extraction of local defect resonance using the principal component analysis in lock-in ultrasonic vibrothermography', *Infrared Phys. Technol.*, vol. 105, p. 103204, Mar. 2020, doi: 10.1016/j.infrared.2020.103204.
- [187] E. team, 'Table of material properties for structural steel S235, S275, S355, S420', EurocodeApplied.com. Accessed: Apr. 18, 2021. [Online]. Available: <https://eurocodeapplied.com/design/en1993/steel-design-properties>
- [188] R. Long, J. Russell, P. Cawley, N. Habgood, D. O. Thompson, and D. E. Chimenti, 'ULTRASONIC PHASED ARRAY INSPECTION OF FLAWS ON WELD FUSION FACES USING FULL MATRIX CAPTURE', in *AIP Conference Proceedings*, Chicago (Illinois): AIP, 2009, pp. 848–855. doi: 10.1063/1.3114345.
- [189] P. Wilcox, M. Lowe, and P. Cawley, 'The effect of dispersion on long-range inspection using ultrasonic guided waves', *NDT E Int.*, vol. 34, no. 1, pp. 1–9, Jan. 2001, doi: 10.1016/S0963-8695(00)00024-4.
- [190] B. Ren, H. Cho, and C. Lissenden, 'A Guided Wave Sensor Enabling Simultaneous Wavenumber-Frequency Analysis for Both Lamb and Shear-Horizontal Waves', *Sensors*, vol. 17, no. 3, p. 488, Mar. 2017, doi: 10.3390/s17030488.
- [191] D. Alleyne and P. Cawley, 'A two-dimensional Fourier transform method for the measurement of propagating multimode signals', *J. Acoust. Soc. Am.*, vol. 89, no. 3, pp. 1159–1168, Mar. 1991, doi: 10.1121/1.400530.
- [192] A. Sedaghati, F. Honarvar, M. Tabatabaeipour, and A. N. Sinclair, 'Investigation of the scattering of Lamb waves from a generalized circular cavity by using Poisson/Mindlin plate theories and numerical simulation', *Proc. Inst. Mech. Eng. Part C J. Mech. Eng. Sci.*, vol. 234, no. 1, pp. 152–170, Jan. 2020, doi: 10.1177/0954406219871073.
- [193] O. Trushkevych, S. Dixon, M. Tabatabaeipour, and G. Dobie, 'Towards Guided Wave Robotic NDT Inspection: EMAT Size Matters', p. 4.
- [194] G. Dobie, R. Summan, S. G. Pierce, W. Galbraith, and G. Hayward, 'A Noncontact Ultrasonic Platform for Structural Inspection', *IEEE Sens. J.*, vol. 11, no. 10, pp. 2458–2468, Oct. 2011, doi: 10.1109/JSEN.2011.2138131.

- [195] E. R. Dobbs, 'ELECTROMAGNETIC GENERATION OF ULTRASONIC WAVES IN METALS', p. 11.
- [196] J. Isla, M. Seher, R. Challis, and F. Cegla, 'Optimal impedance on transmission of Lorentz force EMATs', presented at the 42ND ANNUAL REVIEW OF PROGRESS IN QUANTITATIVE NONDESTRUCTIVE EVALUATION: Incorporating the 6th European-American Workshop on Reliability of NDE, Minneapolis, Minnesota, 2016, p. 090012. doi: 10.1063/1.4940549.
- [197] plusea, *Spiral Coil ULP*. (Apr. 05, 2022). Objective-C. Accessed: Sep. 06, 2022. [Online]. Available: <https://github.com/plusea/EAGLE/blob/1345db3c7c3f31b4594a9f26fd8a48d5925e276a/ulp/spiral-coil.ulp>
- [198] IPC, 'IPC-2221A Generic Standard on Printed Board Design', 2003. Accessed: Sep. 11, 2022. [Online]. Available: [http://www-eng.lbl.gov/~shuman/NEXT/CURRENT_DESIGN/TP/MATERIALS/IPC-2221A\(L\).pdf](http://www-eng.lbl.gov/~shuman/NEXT/CURRENT_DESIGN/TP/MATERIALS/IPC-2221A(L).pdf)
- [199] S. R. Cove and M. Ordonez, 'Wireless-Power-Transfer Planar Spiral Winding Design Applying Track Width Ratio', *IEEE Trans. Ind. Appl.*, vol. 51, no. 3, pp. 2423–2433, May 2015, doi: 10.1109/TIA.2014.2372092.
- [200] E. B. Rosa and F. W. Grover, 'Formulas and tables for the calculation of mutual and self-inductance', p. 237.
- [201] Z. Li, X. He, and Z. Shu, 'Design of coils on printed circuit board for inductive power transfer system', *IET Power Electron.*, vol. 11, no. 15, pp. 2515–2522, Dec. 2018, doi: 10.1049/iet-pel.2018.5780.
- [202] J. L. Rose, S. P. Pelts, and M. J. Quarry, 'A comb transducer model for guided wave NDE', *Ultrasonics*, vol. 36, no. 1–5, pp. 163–169, Feb. 1998, doi: 10.1016/S0041-624X(97)00042-5.
- [203] J. Krautkrämer and H. Krautkrämer, *Ultrasonic Testing of Materials*. Berlin, Heidelberg: Springer Berlin Heidelberg, 1990. doi: 10.1007/978-3-662-10680-8.
- [204] P. A. Petcher and S. Dixon, 'Mode mixing in shear horizontal ultrasonic guided waves', *Nondestruct. Test. Eval.*, vol. 32, no. 2, pp. 113–132, Apr. 2017, doi: 10.1080/10589759.2016.1184268.
- [205] C. A. C. Leckey, K. R. Wheeler, V. N. Hafiychuk, H. Hafiychuk, and D. A. Timuçin, 'Simulation of guided-wave ultrasound propagation in composite laminates: Benchmark comparisons of numerical codes and experiment', *Ultrasonics*, vol. 84, pp. 187–200, Mar. 2018, doi: 10.1016/j.ultras.2017.11.002.
- [206] 'Neodymium Rectangular Magnets | e-Magnets UK'. Accessed: Feb. 10, 2025. [Online]. Available: <https://e-magnetsuk.com/product/neodymium-rectangular-magnets/>
- [207] M. Tabatabaeipour *et al.*, 'Ultrasonic guided wave estimation of minimum remaining wall thickness using Gaussian process regression', *Mater. Des.*, vol. 221, p. 110990, Sep. 2022, doi: 10.1016/j.matdes.2022.110990.